Applications of the Acoustophoretic Force

- Development of Acoustic Tweezing Aided Flotation -

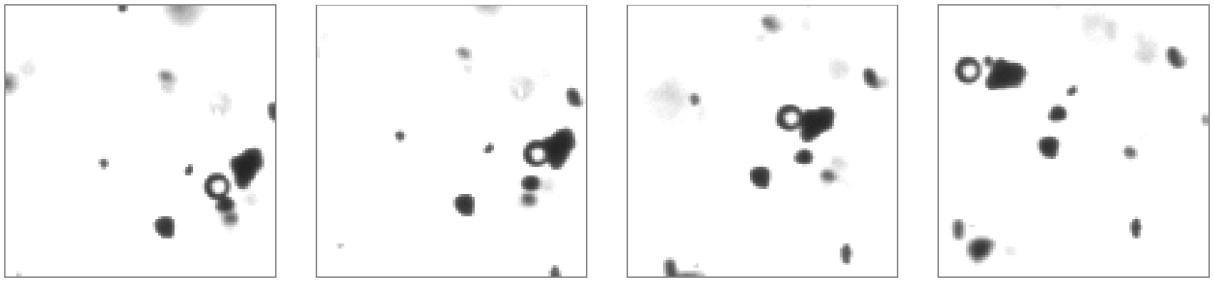

Master's Thesis

Benjamin C. Barlous

Aalborg University
AAU Energy

Energy
Aalborg University
http://www.aau.dk

AALBORG UNIVERSITY
STUDENT REPORT

Title:
Applications of the Acoustophoretic Force Development of Acoustic Tweezing Aided Flotation

Theme:
Extended Master's Thesis

Project Period:
September 2023 to May 2024

Participant:
Benjamin Christopher Barlous

Supervisor:
Per Johansen

Copies: 1

Number of Pages: 80

Date of Completion:
May 31, 2024

Abstract:

This thesis acts as an exploration of the opportunities found when applying the acoustophoretic force in an Acoustic Tweezing Aided Flotation (ATAF) system. A novel dynamic 1D acoustophoretic force expression is derived and validated for a simple geometry. This expression is used to characterize the unknown disturbing forces an air bubble would experience during ATAF with direct implementation in an Extended Kalman Filter(EKF). The EKF provided the ability to characterize disturbing forces on a modelled air bubble, but experimentally, could only characterize disturbance forces on bubbles close to the intialization position due to modelling uncertainties. The acoustophoretic force expression is also used to design a linear control strategy to cause air bubbles to interact with plastic particles. Experimentally, the ATAF system was able to align the x and y positions of the plastic particles and air bubbles with a single transducer using a PI controller and the natural buoyancy of the air bubbles respectively. The z axis position was not able to be controlled for in the experimental setup and this made air bubble and plastic particle absolute position alignment rare. Coupling between air bubbles and plastic particles was proven difficult, due to the use of olive oil, lending no hydrophic attractive force to the interaction. This thesis concludes that there is a potential for the inclusion of the acoustophoretic force in flotation plants, though further research is required.

Contents

Preface

This project was was written by Benjamin Barlous as an Extended Master's Thesis for the Mechatronic Control Engineering Master's Program. It was written between the Fall of 2023 and the Spring of 2024 and is the final project in the Master's program. I would like to thank my supervisor, Per for providing creative and academic guidance. I would also like to thank my wife for the many years of support throughout my educational journey.

During the making of this project, the following programs have been used:

- Overleaf LATEX- For the text processing in this rapport
- MATLAB and Simulink - For calculation, moddeling and data visualization
- Draw.io - For the creation of figures.
- OverLeaf - For the formatting and writing of the thesis.

Aalborg University, May 31, 2024

Benjamin Barlous
Author
<bbarlo19@student.aau.dk>

Synopsis

This master's thesis acts as an exploration into the potential for integrating the acoustophoretic force into a flotation system, referred to as Acoustic Tweezing Aided Flotation by this thesis. This thesis has three focuses; designing a practical "proof of concept" implementation of a Acoustic Tweezing Aided Flotation system, deriving and validating a dynamic characterization of the forces present on an air bubble experiencing the acoustophoretic force, and presenting a control strategy that allows for the facilitation of plastic-air bubble interaction.

This thesis opens with a state of the art where the premise of acoustic tweezing and flotation are presented. This is followed up by a presentation of different studies that apply the methods of acoustic tweezing on micro plastics and air bubbles. This concludes with a presentation of the problem statement being : "*Design a control strategy that allows for the positional manipulation of microsized particles that cannot be directly actuated by the acoustophoretic force*".

A presentation of a 1D pressure wave approximation is then given. This is shown to experimentally capture the wave characteristics for measured pressured waves generated by a transducer in olive oil. The wave equation is then used to define the pressure field and pressure field gradients used by the acoustophoretic force equation. A numerical study is then performed on the derived acoustophoretic force expression that shows that there are acoustic nodes present in the liquid whereby the acoustophoretic force causes particles with a lower contrast factor to be attracted to. The amplitude of this force is analyzed and it is shown that a minimum maximum acoustophoretic force is present on air bubbles in a fluid independent of the wave frequency. The maximum acoustophoretic force field is also shown to occur during acoustic resonance in the geometry. The movement of the nodes as a function of frequency are also shown to move more closer to the face of the transducer and less the further away from the transducer an air bubble would be located.

An equation of motion for an air bubble based on Newton's Second Law is then presented and consists of the acoustophoretic force, a viscous drag component, and an uncharacterized streaming force. This is validated by using experimentally measured bubble positions as the pressure wave frequency generated by the transducer is changed.

The equations for the acoustophoretic force expression is then implemented in an Extended Kalman Filter (EKF). The EKF includes a disturbance force state meant to represent streaming force and other unmodelled dynamics present on the air bubble. This EKF demonstrated the ability to characterise a disturbance force affecting an air bubble in the nonlinear model. The node movement expression, as found by using the acoustophoretic force equation, did not align well with the experimentally shown node positions as the air bubble moved more than 1 mm away its initial position. For air bubbles that remain close to the initial position, it showed a random walk-like characteristic of the acoustic streaming force, though the amplitude of the disturbance force state is determined by the amplitude of the acoustophoretic force and modelling uncertainties mean that the reliability of this force estimate is in question. Considering the sum of forces in the EKF was shown to be able to provide an estimation for the total forces acting on an air bubble and the movement of experimental air bubbles was

compared to simulated air bubbles with the pressure wave input frequencies. Comparing the characteristics of the experimental and modelled air bubble sum of forces as given by the EKF provided insight into where modelling uncertainties may have lied.

The acoustophoretic force expression was then linearized and was used to create a PI controller for the x axis position control of the air bubble using the transducer wave frequency as an input. The varying maximum acoustophoretic force over the control trajectory introduced a high degree of disturbance to the air bubble. On top of this, different radii of air bubbles changed the where the break frequency of the air bubble dynamics was located. The PI controller that was implemented provided sufficient disturbance rejection in both the nonlinear model and experimentally.

This thesis concludes that the inclusion of acoustic tweezing to a flotation plant presents an oppurtinuty into improving the state of the art for flotation. This thesis also concludes that the proposed 1D acoustophoretic wave equation provides a meaningful description of the force acting on an air bubble as the input frequency is changed and that there is potential for further application of the model.

Chapter 1

Introduction

The presence of microplastics in the world's fresh water system has shown to be a serious and wide spread problem.[22] It has been shown that microplastics are slow to degrade naturally, and without active measures put in place, the microplastics concentration is projected to increase in the coming years. [5] Sources of microplastics to the environment are vast, but many of these sources can enter the aquatic environment via emissions from sewage treatment plants[10]. Some amounts of microplastics can be released to aquatic environments from the effluent water, though the majority of microplastics from sewage treatment plants have been found to be retained in the sludge. [10] The removal of microplastics presents a difficulty to the current methods of water processing and is an ongoing topic of research.[18][13]

Within the field of water processing, different approaches have been shown to separate microplastic from liquids.[24] A method used that comes from the field of mineral processing is a method called flotation[25] whereby air bubbles are added to a particulate rich liquid and the interaction between the air bubbles and particulates allows for the removal of the particulate from the liquid. While flotation has been shown to work well for plastics with a diameter of greater than 1 mm[23], flotation has difficulty extracting particles smaller than this size. On top of this, as the particulate density decreases, the efficiency of flotation methods also decreases[25]. The presence of microplastics in water processing plants often have a low concentration of plastic by volume and this poses a difficulty to the state of the art of flotation.

One potential solution to the removal of low concentration microplastics plastics from fluids is to merge the field of flotation with the recent progress in the field of acoustic tweezing.[1] Acoustic tweezing is the process of using ultrasonic acoustic waves to impart a force, called the acoustophoretic force, to actuate a particle's position in a fluid. The manipulation of the acoustic field in the fluid allows for the precise actuation of particulates. Merging recent advancements from this field with flotation could potentially allow for the ability to precisely remove low concentrations of microplastics from a body of fluid. [6].

The merging of flotation and acoustic tweezing methods has not been widely researched and is therefor the motivating initiating problem for this Master's Thesis:

What are the opportunities and limitations of the application of acoustophoretic forces for acoustic tweezing aided flotation?

Chapter 2

State of the Art

Chapter Abstract

In this Chapter, the initating problem is explored. A state of the art on the state of flotation and acoustic tweezing of microplastics is presented and is then followed by a literature study on the progress of acoustophoretic particle control. Flotation systems that can separate plastics from fluid have been shown to exist and work due to air bubble- plastic interactions in a fluid. From the field of acoustic tweezing, the primary contributing factor of the amplitude of the acoustophoretic force is shown to be the difference between the acoustic properties of the fluid and particle, called the acoustic contrast factor. The low contrast factor leads to air bubbles being much easier to actuate than plastic particles and for this reason, flotation should theoretically be able to be matched with acoustic tweezing. The literature on acoustic tweezing focuses primarily on micro-flow channel systems and therefore, few examples of closed loop acoustophoretic systems exist. In order for a closed loop control acoustic tweezing aided flotation system to be designed, a disturbance robust control system must be proposed and dynamic characterization of the acoustophoretic force is required.

2.1 Flotation

In this section, the challenges associated with the application of flotation on plastic particles is given. Flotation is a mature technology that has widespread use in the fields of mineral processing[7], food processing[21], and wastewater treatment.[25]. This field takes advantage of the natural bouyancy of air bubbles in a fluid that will cause the air bubbles to rise to the top of a flotation plant. Most solids that are flotated are generally higher density of the fluid and therefore will naturally drop to the bottom of the container. The focus of the field is therefor the maximization of the interaction between the air bubble and the solids in the fluid. For this reason, the flotation plants are usually continually excited by the bubbles being added to the fluid.

The mechanism for the attachment of the air bubbles and the particulate are the hydrophobic nature of the particles in question.[25] When the particles are hydrophobic, they experience a repelling force from the water and an attractive force towards air bubbles. This causes them to couple and the buoyancy of the air bubbles then pull the particles to the top of the flotation plant. Chemical binders are often added to the fluid to change the degree of hydrophobic repelling force the particulate experiences. This has been shown to be able to make microplastic floteable with the right additive combination to the fluid.[23].

Flotation is often implemented as an open loop process with a focus on high through-

put.[25] Two configurations are most commonly used. A batch configuration that introduces a fixed amount of slurry to a contained volume and a continuous system that constantly supplies slurry to the fluid with and inlet and outlet. The flotation efficiency is often expressed as a first order system with exponentially worsening performance as the particulate concentrations decrease. This leads current state of the art of the particulate/air bubble interactions to occur as a statistical likelihood. This means that flotation process will never be able to remove all of a micro plastic from a fluid.

The challenges that are presented by applying flotation to plastic particles are: managing the air bubble and plastic attractive forces, the geometric design of a plant that can maximize the flotation for the given use case, and ensuring contact between air bubbles and plastic before the air bubble rise.[23] The management of air bubble and plastic attractive forces and the geometric designs of a microplastics flotation plant are both active fields of study. However, the statistical nature of the bubble particle interactions is an inherit limitation in the application of flotation and this thesis claims that this may be overcome by the air bubble actuation potential found in the field of acoustic tweezing.

2.2 Acoustic Tweezing

This section presents the state of the art and discuses the challenges associated with applying acoustic tweezing to a flotation plant. Acoustic tweezing is a branch of acoustofluidics and is a young field of study that has found use in particle sorting and medical applications.[1][16] This is because acoustic tweezing allows for high precision contactless actuation of small particulates on the micro and nano meter scale. A pressure field is introduced to a defined geometry and the pressure field characteristics cause the presence of the acoustophoretic force on particles in a fluid. [20]

Two types of pressure wave manipulation are commonly used for acoustophoretic tweezing; standing acoustics waves, and bulk acoustic waves.[1][19] Bulk acoustic waves use specialized geometry of the transducer horn to create local pressure minima and maxima in the fluid. These require a setup specific transducer design and will no longer be considered in this thesis. Standing acoustic wave acoustic tweezers use the fact that when a continuous pressure wave is generated in a simple geometry, the pressure wave will reflect and waves with positive and negative wave propagation directions will be present throughout the cabin. This leads to there being acoustic nodes and antinodes in the fluid where the time averaged pressure is a maximum and minimum at the these positions respectively.

Acoustophoretic Force

The acoustophoretic equations, as first presented by Gor'kov and further expanded by Settnes and Bruus[20] are given below and an overview of the relevant variables can be seen in Table 2.1:

$$F_{ap} = \frac{4 \cdot \pi}{3} \cdot r_p^3 \cdot \left(\frac{2}{3} \cdot \tilde{\kappa} \cdot Real(f_1 \cdot \mathbf{P}^* \cdot \nabla \mathbf{P}) - Real(f_2 \cdot \rho_l \cdot \mathbf{V}^* \cdot \nabla \mathbf{V}) \right) \tag{2.1}$$

$$\tilde{\kappa} = \frac{\kappa_p}{\kappa_l} \qquad \tilde{\rho} = \frac{\rho_p}{\rho_l} \tag{2.2}$$

$$\kappa_l = \frac{1}{(\rho_l \cdot c_l)^2} \qquad \kappa_p = \frac{1}{(\rho_p \cdot c_p)^2} \tag{2.3}$$

$$f_1 = 1 - \tilde{\kappa} \qquad f_2 = 2 \cdot \frac{\tilde{\rho} - 1}{2 \cdot \tilde{\rho} + 1} \tag{2.4}$$

$$\tag{2.5}$$

Table 2.1: This table gives an overview of the variables that define the acoustophoretic force

Variable	Parameter	Unit
r_p	Particle Radius	[m]
ρ_l	Liquid density	$\left[\frac{kg}{m^3}\right]$
ρ_p	Particle density	$\left[\frac{kg}{m^3}\right]$
c_l	Liquid speed of sound	$\left[\frac{m}{s}\right]$
c_p	Particle speed of sound	$\left[\frac{m}{s}\right]$
κ_l	Contrast Coefficient for liquid	Not Shown
κ_l	Contrast Coefficient for particle	Not Shown
f_1	Monopole Coefficient	[-]
f_2	Dipole Coefficeint	[-]
$\nabla\mathbf{P}$	Pressure Field Gradient	[kPa]
$\mathbf{P}^*$	Pressure Field Complex Conjugate	[kPa]
$\nabla\mathbf{V}$	Pressure Field Gradient	[kPa]
$\mathbf{V}^*$	Pressure Field Complex Conjugate	[kPa]

The relevant physical parameters that define the amplitude of the acoustophoretic force are the fluid and particle's densities, their respective speeds of sound, and the radius of the particle of interest are considered. It can be observed from the equations that the amplitude of the acoustophoretic force scales with the volume of the particle. It is noted that the mass of the particle scales with the volume. When considering the dynamics of a spherical particle, Newtons second law can be used to show that, if ignoring the viscosity of the fluid, this volume gain will have an influence on the dynamics:

$$m \cdot \ddot{x} = F_{ap} \implies \ddot{x} \cdot \rho = \frac{2}{3} \cdot \tilde{\kappa} \cdot Real(f_1 \cdot \mathbf{P}^* \cdot \nabla\mathbf{P}) - Real(f_2 \cdot \rho_l \cdot \mathbf{V}^* \cdot \nabla\mathbf{V}) \tag{2.6}$$

While any fluid that the particle will be submerged in will have a damping dependent with the particle's radius and fluid viscosity, it can be seen that the dynamic excitation due to the acoustophoretic force is independent of the radius. This eases control design by not needing to consider a change of the highly nonlinear acoustophoretic force due to different particle sizes.

The other influencing factor in the acoustophoretic force is the monopoole gain f_1 and dipole gain f_2. When considering the monopole effect, it can be seen that if the kappa value of the fluid and particle equal each other, the monopole contribution, f_1 becomes equal to

zero. The greater the numerical difference between the kappa values for the fluid and particle, the greater monopole influence force becomes. This means that the greater the difference in density and speed of sound, the greater the potential for acoustophoretic manipulation. A similar trend can be seen with the dipole coefficient f_2, only with the particle and fluid densities. One advantage of this trend is that it can be intuitively understood that the manipulation of air bubbles could be achieved relatively easily due to the high difference in density between air and water, whereas particles made out of plastic would likely be less amenable to aoustophoretic manipulation due their relative similarity to the liquid medium. This means that the acoustophoretic force could benefit flotation processes as the high bubble density in the fluid could be given a more deterministic characteristic by the acoustophoretic force.

Another point that can be reasoned from Equation 5.28 is that the amplitude of the acoustophoretic force is proportional to the derivative of the pressure field. This means that the higher frequency components defining the pressure wave are, the higher the potential for acoustic tweezing is. It is for this reason that ultrasonic transducers are used for acoustic tweezing as they operate at a minimum with a frequency higher than 20 kHz. The fact that high frequencies are used means that the wavelengths can be between the micro and nano meter scale. The lower wavelengths at this frequency means that the movement the acoustophoretic force is a good match for acoustic tweezing aided flotation.

2.3 Literature Study on the Acoustophoretic Control of Particles

In this section, a review of the control of air bubbles or plastic particles using the acoustophoretic force is discussed.

A review article from 2020 [6] has shown that little research has been done in the way of implementing acoustophoretic effects in the process of flotation, though they acknowledge the potential benefit for the aggregative effects of acoustophoretic force moving air bubbles towards acoustic nodes. They claim the state of the literature has a focus on using ultrasonic waves as a pretreatment for the slurry. They found that if the amplitude of the pressure waves was too great, the adhesian between the air bubbles and coal became less likely, though this was only described for ultrasonic waves in the 50 kHz range where acoustic cavitation may occur in the air bubbles. They also recognized the potential for high frequency > 1 Mhz had the potential for fine movement actuation for the air bubbles in a flotation system.

Muller et al [11] were able to validate the acoustophoretic force expressions on a particle of radius 5 µm. They were then able to control the motion of this particle by changing the frequency of the transducers. This was performed in a micro channel with no aggregate flow of fluid. This corresponds to there being minimal disturbing forces. While this article demonstrated the ability to use the acoustophoretic force to actuate plastic particles, the limited and contained geometry have yet to demonstrate the ability to scale the acoustophroetic force to larger cabins.

Muiak et al [12] designed a particle filter system that caused micro sized particles to be sorted. This was an open loop configuration that allowed for the collection of different particle densities into the nodes and antinodes of the standing wave respectively. The transducers were run at a constant frequency of 960 kHZ and was performed on a micro channel with a length of 2 times the wavelength of the input frequency. Similiar microchannel flow system have been designed , however scalability of such systems is quite limited for the use in a flotation plant.

Kandemir et al [9] have shown that by using two transducers, net movement of particles on the centimeter scale can be achieved by having a frequency offset on one of the transducers. They found that with a frequency offset is 1 Hz, the particles traveled from node to node on

one second periods. This showed the ability to dynamically actuate a particle throughout a geometry, however the particle position was only be made to be settle at a given predefined wavelength away from the transducer.

Nguyen et al [15] implemented a closed loop air bubble control system that used camera feedback and multiple resonating transducers to actuate 2 axis movement of the air bubble. The system they implemented achieved particle actuated by shifting the phase of one of transducers, changing where the location of the node was. The system they implemented had a distance between the transducers of 1.5 mm and were able to move the air bubble around this area to be able to spell out letters on the micro meter scale.

Literature Discussion

The current state of the art of acoustic tweezing has primarily demonstrated two types of experimental acoustic tweezing setups. The first is to control the flow of particles in a micro channel. This type of experimental setup demonstrates the ability for the acoustophoretic force to actuate particles to defined location while experiencing disturbing forces in the form of turbulent flow in the fluid. The fact that these types of setups are only made to be a few wavelengths means that they are kept at the micro and millimeter scale and these types of setups have not demonstrated the ability to actuate moving particles on the centimeter scale as would be required for Acoustic Tweezing Aided flotation.

The second type of setup shown are controlled two dimensional acoustic fields that show multiple axis of particle manipulation. These experimental setups are highly controlled and the experienced disturbance by the particles are intentionally made minimal. These experimental setups also consists of at least two transducers where acoustic resonance of the chambers can be ensured.

The treatment of the acoustophoretic force when there is not acoustic resonance in the geometry is generally avoided due to the perceived lack of actuation potential. Little literature can therefore be found demonstrating the extent of which particles can be made to move to node locations that do not occur during the acoustic resonance of the geometry. If air bubbles can be shown to still be controlable when there is not acoustic resonance, the control design for such system would be made easier as the input wave frequency could simply be used as a control input. This would allow for the node positions being the functional input to the system and would mean that the acoustic node and, therefore the air bubble, would be able to slowly be moved to the position of the plastic particle, causing positional alignment.

When air bubbles are added to a body of water during the process of flotation, turbulence will be present in the water. In order to control air bubbles or particles under these circumstances, a high degree of disturbance rejecting capability is required.

The literature primarily focuses on actuating air bubbles by changing the phase of the input wave. For this reason, little analysis can be found characterizing the properties of the acoustophoretic force as the input pressure frequency is changed concurrently. The existence of such expressions are a requirement for the characterization of the dynamics for air bubbles under actuation.

2.4 Conclusion

Implementing acoustophoretic forces in a flotation based system would allow for improving the state of the art of flotation. While the utilization of the acoustophoretic force is a popular ongoing topic for research, few centimeter scale experimental setups with visual feedback

have been shown. In order for a acoustic tweezing aided flotation system to be designed the following challenges must first be addressed:

- A validated dynamic model of the acoustophoretic force as the reference wave is changed
- The application of the acoustophoretic force to non micro flow systems
- Design of disturbance rejecting control system for actuated air bubbles

This master's thesis will therefore act as an exploration of these topics.

Chapter 3

Problem Statement and Scope

In this chapter, the problem statement of this Master's Thesis is presented, followed by presenting the thesis scope and providing a reader guide.

3.1 Problem Statement

The problem statement is the following

Design a control strategy that allows for the positional manipulation of microsized particles that cannot be directly actuated by the acoustophoretic force.

In order to answer the problem statement, the following sub problems are solved :

- Propose and validate a dynamic model for particles experiencing acoustophoretic forces
- Propose a disturbance observer that can quantify the unmodelled forces on the controlled air bubble
- Design and propose a control strategy that can allow for the positional manipulation of microsized particles that cannot be directly manipulated by acoustophoretic forces

3.2 Scope

Hardware Configuration

The experimental setup used throughout this Thesis can be seen shown in Figure 3.1. A Table over the hardware components can be seen in Table 3.1.

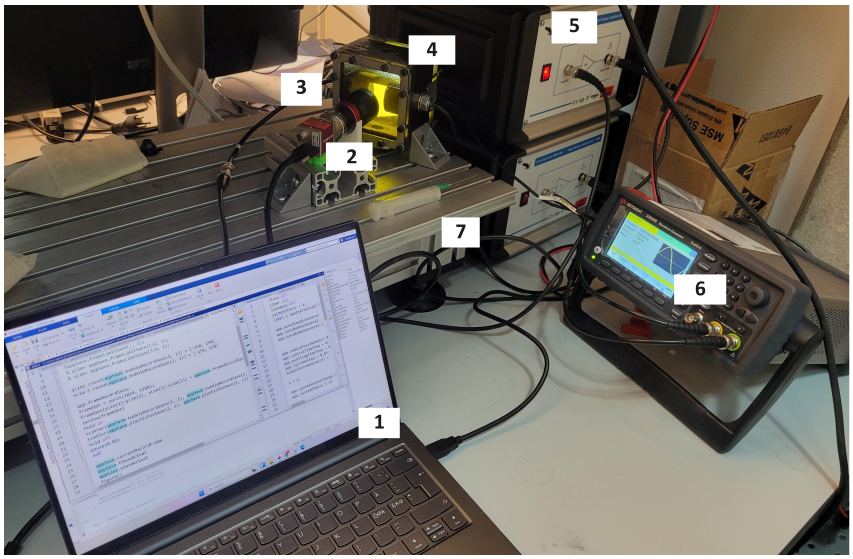

Figure 3.1: This figure shows the experimental setup used in this masters thesis. The components labeld are : (1) Laptop (2) Camera (3) Transducer (4) Cabin (5) Signal Amplifier (6) Wave Generator (7) Syringe. A full description of these items can be found in Table 3.1.

Table 3.1: Table over the hardware components in the experimental setup.

Component	Purpose	Description
Windows Laptop	Controller (1)	Interfaces between the Mako 130B and the waveform generator. Serves as system controller.
MAKO 130B	Camera (2)	Records movement of particles with a maximum framerate of 50 and resolution of 1024x1280 pixels. This corresponds to 76 pixels per mm.
Benthowave II 7581	Transducer (3)	Transmits pressure waves to the liquid. Resonant frequency 960 kHz .
Test Cabin	Cabin (4)	Designed acoustic resonator made with 2 transducers at a distance of 22.83mm apart. Only 1 transducer is used during this Thesis.
Falco Systems WMA-300	Signal Amplifier (5)	Amplifies the voltage of the signal transmitted by the wave generator.
Keysight 33500B	Wave Generator (6)	Generates the sinusoidal signal as assigned by the computer.
Medical Syringle	Syringe (7)	Used for shooting bubbles into the liquid

Limitation of Flotation In Scope

This thesis serves as a preliminary exploration into the potential for acoustic tweezing aided flotation with a focus on the control a single air bubble in the fluid. For this reason, this thesis will not research the influence of different fluids and chemical additives that would affect the coupling between air bubbles and plastic particles. This Thesis focus instead, on actuating the horizontal position of single air bubble such that it is aligned with a single plastic particle. .

Reader Guide

All of the chapters in this thesis, aside for the conclusion, have abstracts that present the method and conclusions of the corresponding chapters succinctly. This master's thesis initially presents the acoustic tweezing aided flotation proposal as this serves as a system proposal that satisfies the problem statement of the thesis. This chapter has a practical focus and can be read with minimal dependence on the other chapters, though it is advisable to read the abstracts from the remaining chapters first. The remaining chapters serve as presentations of the findings gathered when analyzing the topics that were required in order to design the acoustic tweezing aided flotation system. It is advised to read these remaining chapters in their respective order.

The remainder of this Master's thesis contains following chapters:

Chapter 4 - Acoustic Tweezing Aided Flotation: This chapter presents a system proposal for acoustic tweezing aided flotation and discusses the results and difficulties of the implementation.

Chapter 5 - Acoustophoretic Force : This chapter gives a derivation of the time averaged acoustophoretic force when a sinusoidal pressure field is present.

Chapter 6 - Particle Modelling : This chapter presents and validates a model for air bubbles with and without the presence of a ultrasonic pressure field.

Chapter 7 - System Identification of Sonicated Air Bubbles : This chapter presents an Extended Kalman filter with am additional disturbance state and implements it in the nonlinear model and on experimental data.

Chapter 8 - Linear Control : This chapter outlines control requirements and presents a linear analysis of bubbles experiencing the acoustophoretic force. A control proposal for air bubbles is then tested experimentally.

Chapter 9 - Conclusions : This chapter presents the conclusions of this master's thesis.

Chapter 4

Acoustic Tweezing Aided Flotation

Chapter Abstract

In this chapter, a proposal for acoustically aided flotation (ATAF) is presented. A two stage control structure is presented that first moves air bubbles to the plastic particles and then attempts to move the coupled particles. The control strategy is shown to be capable of actuating the bubble to the x-y axis position of the plastic. However, challenges were shown to be present due to two reason: (1) the only interacting force between the air bubbles and particles being the wake generated by the air bubble made attachment infrequent (2) the third uncontrollable axis of the air bubbles and particles position caused absolute position misalignment. The system demonstrated the ability to facilitate air bubble and plastic particle interaction, though further research is required to make the method viable at a larger scale.

4.1 Introduction

In this chapter, acoustic flotation is presented and discussed. The focus of this chapter is to demonstrate on the practical applications of the modeling and control strategies that are presented in this Master's Thesis to flotation. This chapter consists of the following sections:

- Section 4.2 : System Purpose and Design Motivation
- Section 4.3 : Method
- Section 4.4 : Experimental Results
- Section 4.5 : Discussion

4.2 System Purpose and Design Decisions

The purpose for the proposed Acoustic Tweezing Aided Flotation (ATAF) system is to change the horizontal position of plastic particles through the use of controlled air bubbles. In Chapter 8, it is shown that a PI controller is capable of actuating the horizontal position of a single air bubble across multiple milimeters in the test cabin with the use of the pressure wave frequency as input and is therefore the method used for actuating air bubbles in this chapter.

The system has a two step process chain. The first is to actuate an air bubble towards a a plastic particle. The second step is to actuate both the particle and the air bubble together. This can be seen loosely represented in Figure 4.1

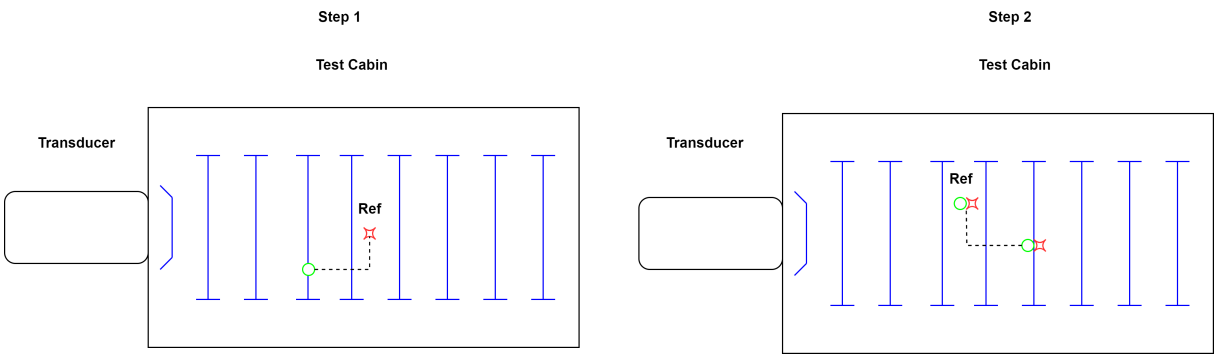

Figure 4.1: This figure shows a block diagram over the configuration of the Acoustic Tweezing Adided Flotation system proposal. The green circle represents an air bubble and the red star represents the plastic particle. The black dotted lines represent a potential trajectory for the air bubbles. The lower bubbles and stars represeent the initial positions and the top dots represent the desired final positions. The rectangular box to the left of the window represents the transducer supplying the pressure waves.

4.3 Method

System Process Description

A block diagram showing the system process chain can be seen in Figure 4.2 and an overview of the switch case program implemented in MatLAB can be seen shown in Table 4.1

System Reference

In the first control case, case 6, the reference of the focused air bubble is that of a plastic particle that is within a specified region of the camera frame. A maximum slew rate for the controller of 1 mm/s is included in the change of the reference to reduce the maximum rate of change of the acoustic node that the air bubbles is attracted towards. This ensures that the controller does not move the node faster than the air bubble can feasibly follow.

In the second control case, case 7, the reference for the air bubble and plastic particle is made to be 1 mm closer to the transducer than the original position at the start of this step. A 0.1 mm/s max slew rate is added to this reference to reduce the chance of the air bubble and plastic particle losing contact to each other during actuation.

Controller

A windows computer running MatLAB is used as the controller for the control system. This is selected as the control controller because it is able to interface with the camera used and the signal generator. The control frequency is set to 10 Hz as this was the highest frequency that could be run on the computer with the ATAF system running.

The controller used is a PI controller with a proportional gain of 10^6 and a integrator gain of 100. When the control case is initialized the initial frequency is set to 700 kHz. A saturation limit is added to the controller that does not allow the frequency to be less than 400 kHz or greater than 1100 kHz. This is because the transducer's pressure wave output is shown to be significantly lower in outside of these limits. [2].

Choice of Particle and Fluid

Throughout this thesis, a commercially available olive oil is used as the fluid medium in which air bubbles and particles are actuated. This is due to its high viscocity at room temperature.

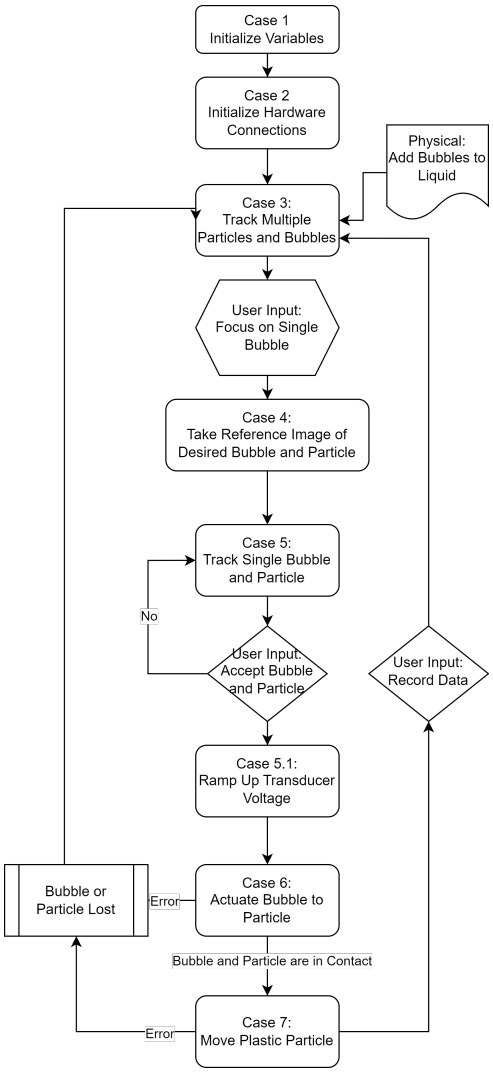

Figure 4.2: This figure gives a visual representation of the switch case structure processing chain during Acoustic Tweezing Aided Flotation.

Case 1.) System Idle

1.	Initialize Variables

Case 2.) System Initialize

1.	Connect to the oscilloscope and waveform generator

Case 3.) Particle Tracking : Sample Time = 0.25s

1.	Search for air bubbles in the defined window
2.	Search for plastic particles the allowed window

Case 4) Focus Bubble and Particle Focusing

1.	Select single bubble and particle and record reference frame.
2.	Select single plastic particle and define a focus frame near this particle

Case 4.2) Initialize Particle Focusing with predetermined Bubble

1.	Find focused bubble in focus search frame
2.	Search for plastic particles in the initial window

Case 5.) Show frames of bubble and plastic : Sample Time = 0.1s

1.	Find focused bubble in focus search frame
2.	Find focused plastic particle in focus search frame

Case 5.1) Show frames of bubble and plastic : Sample Time = 0.1s

1.	Find focused bubble in focus search frame
2.	Find focused plastic particle in focus search frame
3.	Increase transducer voltage by 25 % of nominal voltage and set input frequency to f_{init}

Case 6) Control Running

1.	Find focused bubble in focus search frame
2.	Find focused plastic particle in focus search frame
3.	Run controller with max slew rate of 1 mm/s

Case 7) Control Coupled air bubble / plastic object

1.	Find focused bubble in focus search frame
2.	Find focused plastic particle in focus search frame
3.	Run controller with max slew rate of .1 mm/s

Table 4.1: This table gives an overview of what occurs in the switch case structure during the operation of the Acoustic Tweezing and Flotation system.

This causes the air bubbles to have a lower terminal floating velocity and greatly reduces the sink time of the plastic particles relative to water. This allows for easier simultaneous manipulation of air bubbles and particles. All of the experiments throughout this thesis use this same fluid.

The plastic particles is used for this Thesis are a PET plastic which has a density and speed of sound that is similiar to olive oil. This one type of particle is used throughout the whole thesis.

Transducer Thermal Considerations

The transducer voltage has been reduced to zero when the control steps are not active. This is because the transducer's face that has contact with the liquid will heat up when it's voltage is high. The ambient oil temperature is 23 degrees when the system is off. It has experimentally been found that the transducer face temperature will increase to up to 35 degrees if the transducer is run at full voltage for half an hour. This causes a temperature gradient in the oil whereby the oil close to the transducer begins to flow up to the top of the cabin and a

continuous circular flow becomes present in the cabin. The viscous flow in the cabin them makes bubble control very difficult. When the transducer is only enabled during the control case, the transducer heating is kept to a minimum and this effect is only present directly at the face of the transducer.

Visual Processing

From an image processing perspective, the plastic particles appear very similar to air bubbles and a number of examples of particles and bubble can be seen shown in Figure 4.3

Figure 4.3: This left figure shows a single air bubble. The right figure shows three plastic particles with two air bubbles visible. In the right figure, the bubble to the top left is seen to be out of focus. Transient circular shading can also be seen in both figures and this is likely air bubbles or particles that are highly out of focus.

Bubble Visual Processing

The bubbles are initially found using MatLAB's imfindcircles() function set to find dark circles and then sorted by the function's ideal circle metric. In order to help make sure that the found bubbles found are not plastic particles, the center of the particles are compared to the mean brightness of the frame. If the found circle is a plastic particle, the middle of the particle will be very dark and, if it is a bubble, it will appear hollow and a much brighter middle pixel color. If the middle pixel is too dark, the circle will be dismissed and if it is bright enough, the circle will be accepted as an air bubble. This works the majority of the time, but if it does not, the system user can select another bubble.

During the tracking stage, a selected portion of the frame is searched for bubbles. This portion has been decided to be the bottom middle of the frame. This is because the bubbles will naturally float to the top of the frame and searching the bottom of the frame increases the chance that the bubble can feasibly be moved to a plastic particle reference before disappearing from above the top of the frame. This also has the advantage of reducing the visual processing requirement of the controller.

During the focus stage, a specific bubble is selected. The center pixel of the circle plus the radius of the bubble plus 2 pixels are recorded to the system as a pixel map. This pixel map acts as a reference pixel frame that the following frames are processed to be compared to. Every time a new frame is read, the location of the saved bubble from the previous frame is taken and this location is used to create another pixel map, referred to as the compare bubble frame. This compare bubble frame contains the previous frames bubble center location plus 75 pixels in every direction. This means that a 150 by 150 pixel window from the newly read frame is stored. The reference pixel frame is cross correlated to the compare bubble frame and a heat map with a global minimum is found. This global minimum shows the point that

appears most similar to the reference frame and it is here that bubble location of this new frame is taken to be.

The reference frame is overlaid with an exponentially increasing two dimensional function with a minimum at the previous frame's bubble location. This is because multiple bubbles can appear in this compare bubble frame and the cross correlation can incorrectly select one of the other bubbles as being most similar to the reference frame. This overlaid map weights the bubble correlation towards the previous bubbles location. This is shown to be beneficial because bubble's do not move very much between frames. This has been shown to improve performance and bubble detection stability.

Plastic Visual Processing

Plastic particles are first found after the air bubbles. This is because the frame that is searched for to find plastic particles is made to be 75 pixel above the air bubbles. This is so that the bubbles has an opportunity to reach the plastic particles as they float to the top of the cabin.

Plastic particles are also found using the MatLAB imfindcircle() function, however a smaller radius is used and a higher sensitivity to the circular shape was used. This caused more particles to be found. In order to make sure the bubbles that were found weren't bubbles, the middle pixel was checked to make sure it was dark.

During the focus stage, every time a new frame was read, the imfindcircles() function was run using a frame window size within 50 pixels of the previous particle location. If the particle was not found in the new frame, the frame sensitivity was increased until a particle was found and the particle closest to the previous particle location was taken. This method was selected because the particles move very little every frame and the method demonstrated the ability to track the plastic particles adequately.

4.4 Experimental Results

Many attempts have been made to cause the bubbles to interact with the plastic. Two examples of running the ATAF system are shown; the first demonstrates the movement of and air bubble and plastic particle before and after coupling and the second demonstrates the interaction between the air bubble plastic when they come in contact, but do not successfully couple.

4.4.1 Coupled Movement of Plastic and Air Bubble

In this section, an example of an air bubble being actuated to the position of a plastic particle and the collective movement of the coupled air bubble and plastic particle is shown. A number of frames of the air bubble interacting with and then moving a plastic particle can be seen shown in Figure 4.4.

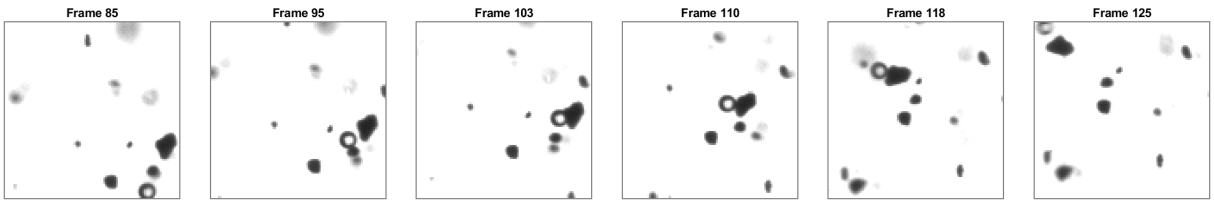

Figure 4.4: This figure shows the movement of an air bubble and plastic particle during the contact phase of the Acoustic Tweezing Aided flotation. The air bubble has a radius of 60 µm. The position of the frame is held over the frames shown. The air bubble achieves contact with the plastic particle between frames 95 and 103 and looses contact between frame 118 and 125. The frames shown occur over 4 seconds.

The horizontal and vertical positions of the air bubble and plastic particle shown in Figure 4.4 have been plotted and can be seen in Figure 4.5.

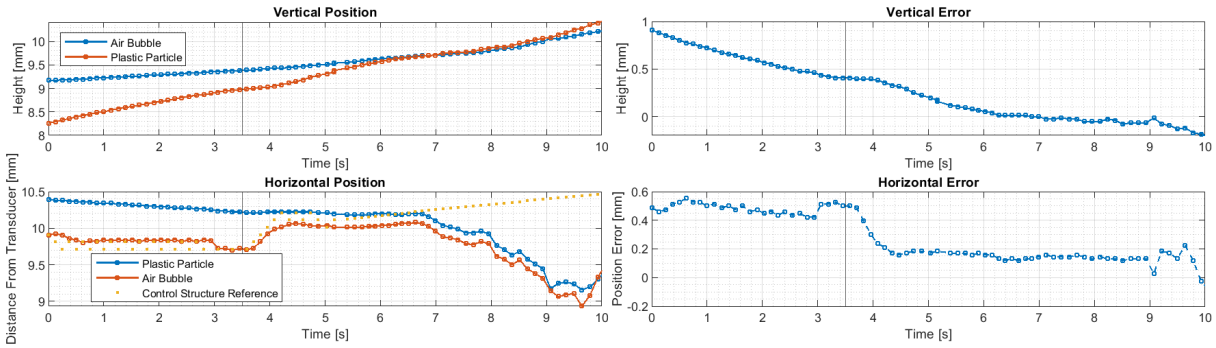

Figure 4.5: This figure shows the air bubble vertical and horizontal position during the operation of the ATAF. The black line at approximately 3.5 seconds refers to when the air bubble acquires the plastic particle as its x axis position reference. The offset seen in the horizontal error in the bottom right figure between 4 and 9 seconds is due to the radii of the air bubble and plastic particle to cause a position difference between each other despite being in contact.

When looking at the horizontal position data in the lower bottom left plot in Figure 4.5, it can be seen that the ATAF system has successfully caused the air bubble to move the plastic particle. When looking at the air bubble and plastic particle horizontal positions between 3.5 and 4 seconds, the acoustic force causes the air bubble to align the air bubble x position to the plastic particle, whereas the acoustophoretic force does not cause a discernible change to the plastic particle x location. From 7 seconds to 10 seconds, it can be seen that the controller was not able to actuate the air bubble and plastic particle to its desired reference. Despite this, during this time, both the air bubble and plastic particle positions are moved together. Without successful coupling, the movement of the plastic particle would have been negligible. For this reason, the ATAF system is considered "successful" despite the controller not moving the coupled air bubble plastic particle object to the desired reference position after the plastic became coupled to the air bubble.

It can be seen, when looking at the vertical error in the top right plot of Figure 4.5 that the coupling to the air bubble also changed the change of floating velocity of both the air bubble and plastic particle. This can be seen when comparing the vertical error between the air bubble and plastic particle between 0 to 6 seconds and then from 6 to 9 seconds. The fact that the vertical error is maintained at zero between 6 and 9 seconds when the air bubble and plastic particle are in contact, demonstrates that they both impart an attractive force on each other. This attractive force effectively causes there to be a collective buoyancy force on the coupled plastic-air bubble object. When looking at the top left figure, it appears to be the case that the coupled floating velocity is more similar to the plastic particle than it is to the free air bubble floating velocity. If the air bubble that achieved coupling with the plastic was larger than the one shown, the buoyancy experienced by the air bubble would likely cause the coupled air bubble plastic particle object to float at a higher rate, though it may also have caused the two to disengage from each other faster than they did.

The coupling between the air bubble and plastic particle is interpreted by the author to be similar to a spring force. If the air bubble experiences a force vector that is greater than the maximum spring force, the air bubble becomes decoupled to the plastic particle. This appears to occur at 9 seconds as this is when the horizontal error between the air bubble and plastic particle quickly changes value. After this point, the vertical error begins to increase again.

It can be noted in Figure 4.5 that the control reference was unintentionally changed to the plastic particle once the air bubble and plastic particle became coupled. This resulted in

the controller rapidly changing the frequency in a manner which made the bubble not follow along the reference very well. This occurs at approximately 6 seconds.

4.4.2 Contact without Coupling

For the majority of air bubble plastic particle interactions observed experimentally, the air bubble comes in contact with the plastic particle and affects the movement of the plastic particle, but coupling does not occur. An example of this occurring is analyzed in this section. Selected frames of the contact between the air bubble and plastic particle can be seen shown in Figure 4.6.

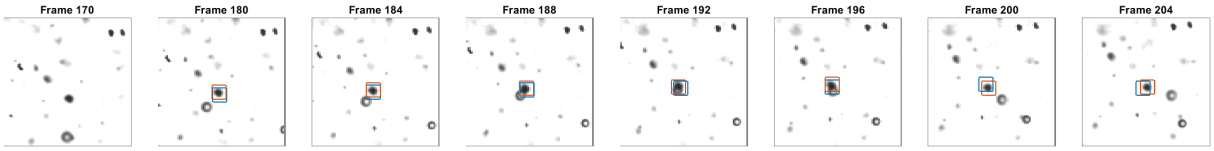

Figure 4.6: This figure shows an example of an air bubble interacting with a plastic particle, but successfully coupling does not occur. The interacting air bubble has a radius of 72 µm. The blue squares represent the plastic particle position of four frames previous to the one shown and the orange square show the current position of the plastic.

It can be seen in Figure 4.6 that in frames 180 and 184, the plastic particle unaltered velocity moves it slightly in the direction to the left of the frame. This is contrasted to what occurs after air bubble plastic contact as can be seen in frames 196, 200, and 204 where the plastic particle begins to move to the right side of the frame. The vertical and horizontal positions of the plastic particles can be seen shown in Figure 4.7

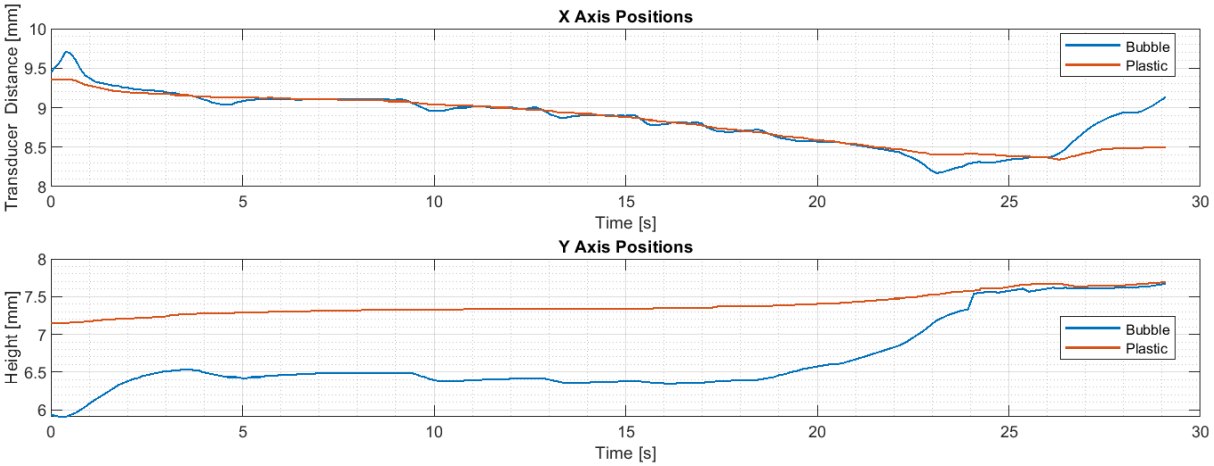

Figure 4.7: This figure shows the horizontal and vertical positions of the air bubble and plastic particles shown in Figure 4.6 as the ATAF system is run.

When looking at the horizontal positions of the plastic particle and air bubble in the top plot of Figure 4.7, the air bubble demonstrates the ability to follow the trajectory of the plastic particle with the control enabled. It can be seen that when the control is first activated, the air bubble initial moves in the wrong direction before aligning position with the particle. The initial movement is likely due to the transducer voltage being ramped up once the ATAF system is enabled and this making the nearest acoustic node to be at a location that does not align with the air bubbles initial location. It can also be seen between 23 and 24 seconds that, as the vertical position of the air bubble quickly changes, a small air bubble horizontal position error occurs , but this is quickly attenuated by the PI controller.

It can be seen that from 0 to 3 seconds and between 18 and 25 seconds, the air bubble floats to the top of the cabin as is expected for an air bubble in a fluid. However, between 3 and 17 seconds, the air bubble sinks slightly and maintains depth in the fluid. The ATAF system was kept running during this period and control over the x axis position of the air bubble is maintained. At 17 seconds, the air bubble began to float up to the plastic particle again. This demonstrates the pressure field causing a force on the air bubble on the vertical axis as well as the horizontal axis.

Contact is achieved between the air bubble and plastic particle at approximately 25 seconds, as it is here where both the air bubble vertical and horizontal positions align. It can be seen when comparing the horizontal position of the plastic particle in the top plot, before and after 26 seconds, that the horizontal velocity of the plastic particle is changed. The plastic particle quickly looses contact with the air bubble at 27 seconds, however, as can be seen by the air bubble and plastic particle horizontal positions diverging from eachother.

4.5 Discussion

The discussion is broken up into two section: a discussion of the results of the ATAF in the context of the literature on the field of acoustofluidics and a discussion of the implementaion and design of the ATAF system.

4.5.1 Literature Discussion

The direct actuation of air bubbles to the position of micro plastic demonstrated by the ATAF system has reinforced the claim that the inclusion of ultrasonic waves in the fluid can be a useful tool to help facilitate air bubble plastic particle interaction made by Chen et al. [6] in their review article of ultrasonic forces and flotation. It was found during the operation of the ATAF system that the primary difficulty was facilitating the coupling between the air bubble and plastic particle. This challenge is also one cited by Chen et al, however, the fact that no hydrophobic force is present in olive oil means that it is unclear whether difficulty in coupling was due to the presence of the ultrasonic field or a similar difficulty in causing couple would occur without the acoustic field.

With the initial frequency of the transducer used by this thesis being set to 700 [kHz], there were over 10 wavelengths of the pressure wave in the cabin. The fact that the air bubble maintained close proximity to the nearest node supports the finding by Musaik et al [12] where they caused particles to aggregate to the acoustic nodes in the microchannel. The ability to control the air bubble by changing the locations of the acoustic nodes demonstrates that the bubble aggregating effect of the acoustophoretic force is not limited to micro scale geometries.

The ability for air bubbles to be actuated across multiple milimeters by changing the pressure field frequency demonstrates the viability of actuating individual air bubbles by changing the frequency of the pressure wave. The flexibility of provided by this method could be combined with the phase shifting node position methods shown by Kandemir et al [9].

The ATAF system achieves 1 dimensional actuation of the air bubbles with the use of only a single transducer. This success of the air bubble actuation of demonstrated by the ATAF system shows that the benefits of ultrasonic actuation can be achieved without the need for two or more transducers as has been shown by the literature. [9] [12] [11] This suggests that the application of the acoustophoretic force in industrial processes may have a lower barrier for entry than what is suggested by the literature.

4.5.2 Design Discussion

Particle-Bubble Interactions

The decision to have the fluid in the cabin to be olive oil made it very difficult to have the air bubble interact with the plastic particles. Because no hydrophobic effects are present, the only attractive force between the plastic particle and air bubble is due to the wake effect that is caused by the air bubble moving. Further testing would benefit from using water as a fluid medium. It is worth noting however, it has been shown by Chen et al [23] that plastic particles have a low natural hydrophobic nature. It is likely that a chemical binder may be required to achieve a large performance boost than what was shown when using olive oil as the fluid.

The difference when switching from olive oil to water is that the viscocity of water is over an order of magnitude greater than olive oil at room temperature.[3] This presents both opportunities and challenges. This has the advantage of there being a smaller frictional coefficient due to the air bubble velocity. This means that less of the kinetic energy transferred to the air bubble is dissipated due to friction, resulting in a higher maximum potential for the movement of air bubbles due to the acoustophoretic force. The challenges that this presents are that the terminal velocity of air bubbles becomes much greater. This means that the ATAF system has less time to facilitate coupling between the air bubble and plastic particle. This puts a higher demand on the control structure and would likely require a higher performance controller and higher framerate camera than what is used by this thesis.

Acoustic Change of Viscous Forces

An unforeseen challenge presented during the actuation of air bubbles is the vertical force that the acoustophoretic force experimentally imparts on an air bubble. The off axis force his caused some air bubbles to be "locked" and would greatly reduce their terminal floating speed. This can be seen shown when looking at the air bubble's vertical position in the bottom plot of Figure 4.7 on page 19. For smaller particles, this meant that particles would sometimes not move at all for multiple seconds. The reason for the change in the vertical force balance affecting the air bubble is suspected to be due to the acoustic field being a three dimensional field. For this reason, the acoustic nodes considered by this thesis likely have a much more complex geometric component to them than is assumed by the 1D force equation and there are actually pressure field gradients in the y axis as well as the x axis. As was shown in Section v6.3.3, this effect went away when no pressure wave was present. One solution that was experimented with is to reduce the transducer supply voltage once the x axis position is aligned. The bubble will then float up to the plastic particle where the voltage can then be enabled again. Further iterations of the acoustic tweezing aided flotation would benefit from including this in the control strategy.

Flattened Multi Dimensional Control Problem

In order to have the bubble and particle interact, they must be in the same x, y and z plane. The system presented in this chapter, only controlled the x position directly. The y position alignment occurred due to the buoyancy force on the bubbles that causes itself to raise. This axis is managed by making sure that the air bubbles that are selected have an initial depth that is greater than the plastic particle. The natural buoyancy of the air bubbles then causes the y axis alignment.

The last directional plane, the z plane, is not controlled by the method presented. The camera used has a defined focal range where the edges of the air bubbles and plastic particles

are most clear. Bubbles which have highly defined edges are selected by the use of the imfindcircles() most defined circles object parameter. The focal range of the used camera is expected to be around 4-7 mm, as has been estimated by comparing the definition of different objects being moved towards and away from the camera. This high focal range means that, even if air bubbles are assumed to be on the same z plan axis, the majority of the time, the distance between them is greater than the sum of the radii between the air bubble and plastic particle. For this reason, it can be expected that, if the average air bubble has a radius of 150 mm and the average plastic particle has a radius of 100 mm, the chance of them actually interacting is less than one in 10. Experimentally, the amount of air bubbles and plastic particles that were actuated to be on the plastic x and y axis positions, but did not demonstrate any interaction, was actually much higher than this. This suggests that, when actuating a single air bubble to a specific plastic particle, that a more controlled micro-scale environment would be a better experimental setup to research this type of interaction.

Timing And Hardware Considerations

The controller was able to run at a frequency of 10 Hz. The maximum frame reading speed was 0.02 seconds, and the image processing took approximately 0.03 seconds for each frame. The remaining time requirements was used on the visual representation of the status of the system. This included showing the frame of the particles and plastic during control. This was required because the visual algorithm had the tendency to loose focus on particles or change the air bubble reference occasionally. When this happened, the system can be considered to fail, but did not always register an error. The control response is shown to be acceptable with this sample time. Using a faster PC could allow for the improvement of the performance of the system. The higher the framerate that the control strategy is run on, the better the tracking stability. On top of this, the higher potential bandwidth of the control algorithm. This would have the added benefit of further improving the disturbance rejection frequency response and a higher effective bandwidth could be used in the controller.

4.6 Conclusion

The acoustic tweezing and flotation system presented in this chapter has shown the ability to facilitate air bubble and particle interaction. Difficulty in the actuation of plastic particles was present due to the lack of particle/air bubble attractive force and the limitation of 2 axis of control for what is a three dimension control problem. This chapter has, demonstrated the potential for acoustic tweezing aided flotation as an opportunity for improving the state of the art of flotation.

Chapter 5

Dynamic Acoustophoretic Force Modelling

Chapter Abstract

This chapter derives and validates a dynamic expression for the acoustophoretic force that a particle experiences in a fluid. In Section 5.2, the time averaged acoustophoretic force bounding equations are presented. In Section 5.3, a one dimensional unsteady model for pressure waves in a cabin are introduced. The steady state and transient wave expressions appears to align well with experimentally measured pressure waveforms and the wave equation is deemed validated. In Section 5.4, the wave model is applied to the acoustophoretic force expression is derived for the steady state and transient acoustophoretic force field. The force field is expressed as an infinite series of sinusoidal expressions that exponentially decay as the number of terms increases due to the damping from reflection. The amplitude of the acoustophoretic force field is shown to be dependent on how close the input frequency is to resonance. The movement of the generated acoustophoretic nodes due to changing the input frequency is shown to correlate with how close the particle is to the transducer face. There is maximum node movement potential directly at the face of the transducer and zero potential for moving the node position directly at the opposing cabin wall.

5.1 Introduction

In this chapter, a dynamic model for the time averaged amplitude of acoustophoretic forces is presented. This is done by first presenting and validating a transient one dimensional wave equation solution. A steady state and transient infinite series for the amplitude of acoustophoretic forces is then proposed. A discussion of the potential for particle actuation as a function of changing the transducer output frequency is then performed.

The contents of this chapter are broken up into the following sections

- Section 5.2 : Acoustophoretics Equations
- Section 5.3 : Transient 1D Wave Equation
- Section 5.4 : Analytical Acoustophoretic Force Expression
- Section 5.5 : Analysis of the Dynamic Acoustophoretic Force

5.2 Acoustopheretics

In an inviscid fluid, the time average of the acoustophoretic force, F_{ap} a particle in a fluid will experience is repeated:[20]:

$$F_{ap} = \frac{4 \cdot \pi}{3} \cdot r_p^3 \cdot (\frac{2}{3} \cdot \tilde{\kappa} \cdot Real(f_1 \cdot \mathbf{P}^* \cdot \nabla \mathbf{P}) - Real(f_2 \cdot \rho_l \cdot \mathbf{V}^* \cdot \nabla \mathbf{V})) \tag{5.1}$$

Where P^* and V^* are the complex conjugates of the pressure and velocity fields in the fluid, respectively. The rest of the expressionare are given given in terms of the densities, ρ and speed of sounds c where the subscript l indicates the liquid and p the particle:

$$\tilde{\kappa} = \frac{\kappa_p}{\kappa_l} \qquad \tilde{\rho} = \frac{\rho_p}{\rho_l} \tag{5.2}$$

$$\kappa_l = \frac{1}{(\rho_l \cdot c_l)^2} \qquad \kappa_p = \frac{1}{(\rho_p \cdot c_p)^2} \tag{5.3}$$

$$f_1 = 1 - \tilde{\kappa} \qquad f_2 = 2 \cdot \frac{\tilde{\rho} - 1}{2 \cdot \tilde{\rho} + 1} \tag{5.4}$$

$$\tag{5.5}$$

It can be observed from 5.28 that, when neglecting change of particles' and fluids' radius and density due to pressure oscillations, the only time varying components are $\mathbf{P}$, $\nabla\mathbf{P}$, $\mathbf{V}$, $\nabla\mathbf{V}$. The radius and density oscillatory effects are negligible relative to their steady state values, and therefore, their exclusion from the analysis is deemed an acceptable assumption. In conclusion, in order to model the dynamics of the acoustophoretic force, only time varying pressure and velocity fields propagating through a fluid must be derived.

5.3 Transient 1D Wave Equation

This section derives an expression for a pressure wave and as a function of the distance from the pressure wave source in a fluid. This is then validated in Section 5.3.3 on page 28.

Wave Analysis Assumptions

In the analysis of this chapter, one dimensional waves are considered. This is because the wave generating transducer's face is set to be orthogonal to the axis that the particles will be actuated along. Higher dimensional wave analysis would require a much more intensive analytical treatment and is therefore beyond the scope of this thesis. 1-Dimensional treatment is also shown to describe the majority of particle movement under acoustophoretic force and is therefore deemed an acceptable assumption.

The source of the pressure wave in this chapter is assumed to be an ideal wave generator. That is to say that the dynamics associated with changing the transducer emitting state from off to on are neglected. While every transducer and voltage supply have associated dynamics, these are largely present in the underlying electrical system. As a rule of thumb, electrical systems are much faster than the mechanical excitation associated with the vibration that generates the pressure waves and is therefore deemed and acceptable assumption. This assumption is discussed when comparing the transient behavior of the presented wave equation to experimental results in Section 5.3.3 on page 28. .

The transducer pressure wave output frequency response is not analyzed in this chapter. The fact that true pressure wave amplitude being generated by the transducer varies has

experimentally found to not play a large role in the overall dynamics present on air bubbles experiencing the acoustophoretic force in this Thesis. The pressure output frequency response of the transducer is therefore assumed to be flat response and the divergence from this is considered a modelling uncertainty

5.3.1 Wave Analysis Derivation

As an initial analysis point, the pressure wave in the fluid is modelled as a harmonic time varying wave. An expression for the harmonic pressure field, $\mathbf{P}_{harm}$ is given as the following[17]:

$$\mathbf{P}_{harm}(t,x) = P_{amp} \cdot e^{j\cdot(\omega\cdot t - k\cdot x)} \tag{5.6}$$

P_{amp} is the amplitude of the pressure wave. k is the wave number of the wave given by Equation 5.7, c is the speed of sound in the fluid, and ω is the angular velocity of the pressure wave. t and x refer to to time and distance from the wave source, respectively.

$$k = \frac{\omega}{c} \tag{5.7}$$

The pressure wave propagation through the liquid can be modelled as the product of a step function and the harmonic wave equation. The step function causes the pressure field to propagate through the space of the fluid. The pressure wave travels at the speed of sound, c. A representation of this traveling field, $P_{harm.p}$ can be seen in Equation 5.8, where $\mathbf{u}(t - x/c)$ represents the step function propagating along the x axis away from the source.

$$\mathbf{P}_{harm.p}(t,x) = P_{amp} \cdot e^{j\cdot(\omega\cdot t - k\cdot x)} \cdot \mathbf{u}(t - \frac{x}{c}) \tag{5.8}$$

Whereby, the step function can be seen expressed in Equation 5.9

$$\mathbf{u}(y) = \begin{cases} 1, & y >= 0 \\ 0, & y < 0 \end{cases} \tag{5.9}$$

An inverted pressure wave, $P_{harm.p.i}$, is now presented. The property of this wave is that when the inverted wave is added to the wave shown in Equation 5.8, the total pressure field is zero. This mathematical abstraction serves as a method for being able represent the gradual disappearance of a field as this inverted wave "propagates" and cancels out the previous wave. This is shown in Equation 5.11 where $P_{harm.p.i}$ is added to another pressure wave, that is 180deg out of phase of the initial wave. This inverted wave begins to propagate when the wave source is no longer emitting. The time at which this occurs is denoted T_{end}. This can be seen in the following Equations:

$$\mathbf{P}_{harm.p.i}(t,x) = P_{amp} \cdot e^{j\cdot(\omega\cdot t - k\cdot x + \pi)} \cdot \mathbf{u}(T_{end} - (t - \frac{x}{c})) \tag{5.10}$$

$$\mathbf{P}(t,x) = P_{harm.p}(t,x) + P_{harm.p.i}(t,x) \tag{5.11}$$

It can be noted that after T_{end} there is no longer a pressure field present in the fluid.

When the wave has propagated throughout the length of the cabin, it will reflect off of the oposing wall to the transducer. When this occurs, some of the energy of the wave is dissipated on the wall and the remaining wave energy will be sent in the opposite direction back towards the transducer. The wave amplitude as it propagates towards the transducer will be reduced by a damping factor, β. To express this, the pressure field approximation is supplemented with the inclusion of another pressure wave expression, P_{R1}. The corresponding step function

acts in the opposite direction due the opposite travel direction. Because the time expressed in the equations shown starts from when the wave is first reaches the opposing end of the geometry, a delay variable, T_{delay} is added to this reflecting wave's step function. This refers to the time it takes for the wave to first reach the chamber wall.

$$P_{R1}(t,x) = \beta \cdot P_{amp} \cdot e^{j\cdot(\omega\cdot t - k\cdot(L-x)} \cdot \mathbf{u}(t - T_{delay} - \frac{L-x}{c}) \tag{5.12}$$

$$T_{delay} = \frac{L}{c} \tag{5.13}$$

L represents the length of the chamber. It can be noted that the direction of propagation in the step function from Equation 5.12 is opposite of that of Equation 5.8. It can also be seen that the sign of the x coefficient in the exponential equation has also been inverted from Equation 5.8 and it is positive in Equation 5.12

The corresponding inverse of this Equation 5.12 can be seen as follows:

$$P_{R1.i}(t,x) = \beta \cdot P_{amp} \cdot e^{j\cdot(\omega\cdot t - k\cdot(L-x)+\pi)} \cdot \mathbf{u}(T_{end} - (t - T_{delay} - \frac{L-x}{c})) \tag{5.14}$$

The fact that the wave will propagate an infinite times from each wall is used to create a general equation for the the waveform that is produced by the transducer.

$$P_{tot} = P_{left} + P_{right} + P_{left.i} + P_{right.i} \tag{5.15}$$

$$P_{left} = \sum_{n=1}^{\infty} \beta^{2\cdot(n-1)} \cdot P_{amp} \cdot e^{j(\omega\cdot t - k\cdot x - k\cdot L\cdot 2\cdot(n-1))} \cdot \mathbf{u}(t - \frac{x}{c} - 2\cdot(n-1)\cdot T_{delay}) \tag{5.16}$$

$$P_{right} = \sum_{n=1}^{\infty} \beta^{1+2\cdot(n-1)} \cdot P_{amp} \cdot e^{j(\omega\cdot t - k\cdot x - k\cdot L\cdot 2\cdot n)} \cdot \mathbf{u}(t - (1+2\cdot(n-1))\cdot T_{delay} - \frac{L-x}{c}) \tag{5.17}$$

$$P_{left.i} = \sum_{n=1}^{\infty} \beta^{2\cdot(n-1)} \cdot P_{amp} \cdot e^{j(\omega\cdot t - k\cdot x - k\cdot L\cdot 2\cdot(n-1)+\pi)} \cdot \mathbf{u}(T_{end} - (t - \frac{x}{c} - 2\cdot(n-1)\cdot T_{delay})) \tag{5.18}$$

$$P_{right.i} = \sum_{n=1}^{\infty} \beta^{1+2\cdot(n-1)} \cdot P_{amp} \cdot e^{j(\omega\cdot t - k\cdot x - k\cdot L\cdot 2\cdot n+\pi)} \cdot \mathbf{u}(T_{end} - (t - (1+2\cdot(n-1))\cdot T_{delay} - \frac{L-x}{c})) \tag{5.19}$$

5.3.2 Quasi Standing Waves

An interesting property that emerges from the expression for the pressure field shown in Equation 5.15 is that the summation of sinusoidal waves in a given space expresses the pressure field as a quasi standing wave. For the purposes of this thesis, quasi standing waves refers to pressure waves where the RMS of the sinusoidal waves along the x-axis is position dependent and not time dependent with local mimimum and maximums for every wavelength throughout the cabin. This can be seen when considering the harmonic wave equation shown in Equation 5.6 as a sum of two opposite direction travelling waves with the same frequency and amplitude :

$$P(x,t) = P_1 \cdot e^{\omega\cdot t - k\cdot x} + P_2 \cdot e^{\omega\cdot t + k\cdot x} = (P1 + P2) \cdot e^{\omega\cdot t\cdot i} \cdot (e^{k\cdot x\cdot i} + e^{-k\cdot x\cdot i}) \tag{5.20}$$

Taking the real component of Equation 5.20 gives the pressure amplitude of the wave and can shown to be the following:

$$P_{real}(x,t) = (P_1 + P_2) \cdot cos(k \cdot x) \cdot cos(\omega \cdot t) \tag{5.21}$$

In the steady state case where one of the waves has a different amplitude and phase, the resultant pressure wave is the following:

$$P(x,t) = P_1 \cdot e^{i(\omega \cdot t - k \cdot x + \phi_1)} + P_2 \cdot e^{i(\omega \cdot t - k \cdot x + \phi_2)} = e^{i \cdot \omega \cdot t} \cdot (P_1 \cdot e^{(i \cdot (\phi_1 - k \cdot x)} + P_2 \cdot e^{(i \cdot (\phi_2 + k \cdot x)}) \tag{5.22}$$

Taking the real part of Equation 5.22 gives the following:

$$P_{Re}(x,t) = P_1 \cdot (cos(\phi_1 - k \cdot x + \omega t) + P_2 \cdot cos(\phi_2 + k \cdot x + \omega \cdot t) \tag{5.23}$$

It can be noted that if, for a given frequency, that the wavelength is equal to the length of the chamber, the resultant pressure field from Equation 5.23 will appear similar to Equation 5.21. While the intuition behind Equation 5.23 is not as clear as Equation 5.21, the resultant pressure field at different frequencies has been plotted using a c value of 1430, a damping coefficient of 0.7, and initial field amplitude of 1 and can be seen in Figure 5.1.

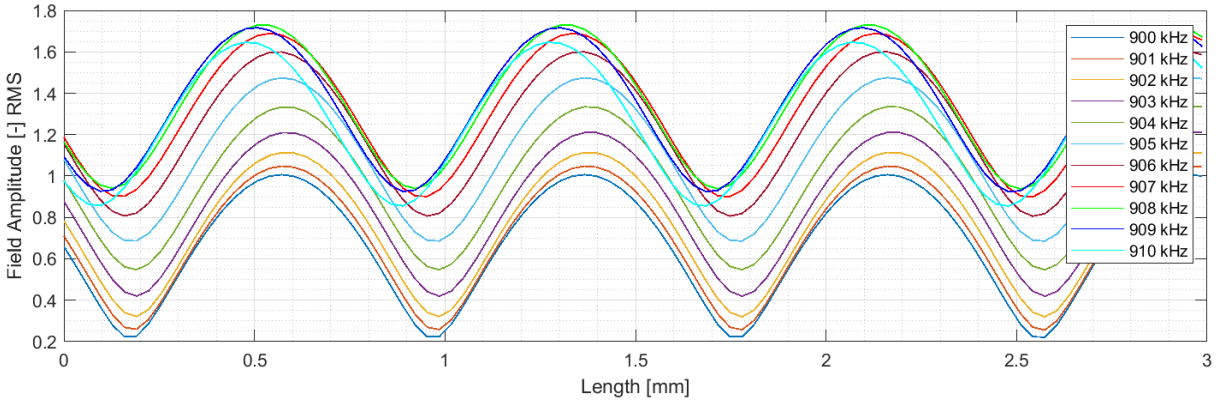

Figure 5.1: Plots of the RMS of the generated pressure fields as a function of distance from acoustic source. Because the RMS taken, this pressure wave is considered position dependent and not time dependent.

It can be seen from the location of the peaks of Figure 5.1 that there is a dependency between peak location along the x axis and frequency. This is to be expected as the wavelength of the waves changes as a function of frequency. Another point of note is that, as the frequency changes, the minimum and maximum values of the RMS of the fields change. This can be seen further illustrated in Figure 5.2.

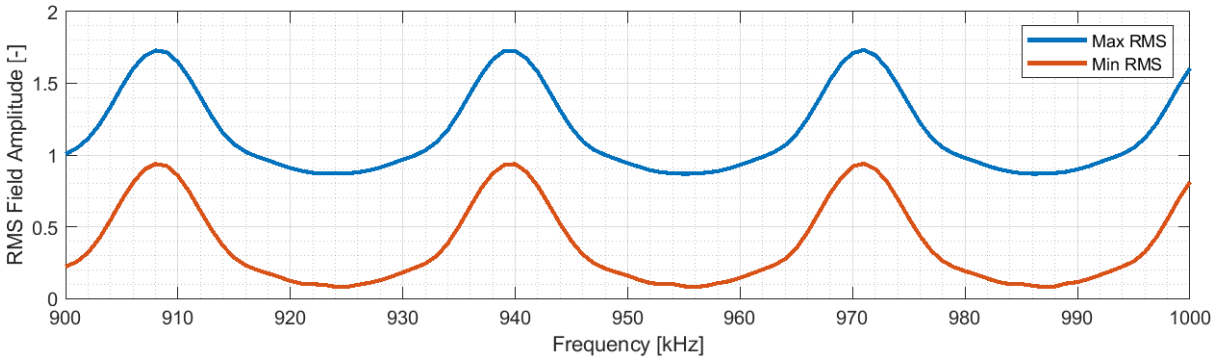

Figure 5.2: Minumum and maximum values of the pressure RMS tract the length of the cabin as a function of frequency.

It is the case that the difference between the minimum and maximum RMS of the signals in Figure 5.2 is shown to be independent of frequency. While the difference between the minimum and maximum RMS of a pressure wave is independent of frequency, this is not the case for the amplitude of the acoustophoretic force. This is because the amplitude of the acoustophoretic force is shown to be proportional to the product of itself and its spatial derivative.This means that the higher the positional RMS gradient of the pressure wave, the greater the acoustophoretic force.

5.3.3 Validation of Wave Expression

The experimental setup shown in the system scope has been used to test the validity of the presented pressure wave expression. In this section, the transducer used is the Benthowave BIL 8501-1000 driven at 150 V peak to peak sinusoidal waves. These tests were performed using olive oil as a fluid medium at room temperature with a speed of sound, $c_{l.oo}$ of approximately 1505 m/s and a density $\rho_{l.oo}$ of approximately 860 kg/m^3. 180 Wavelengths at a given frequency were generated by the wave generator and measurements of the pressure field were recorded using a hydrophone as shown in Figure 5.3.

Figure 5.3: This figure shows an image of the hydrophone and the transducer used to record pressure wave data and the yellow line denotes the position the image recognition algorithm considers the transducer face. The black region along the right side of the figure is the transducer face. This figure shows the features that have been extracted from the image processing. The red '+' on the hydrophone is the calculated center of the hydrophone.

Steady State Wave Comparison

For the steady state wave comparison, the hydrophone was used to record a waveform every 6 seconds. Just before querying the oscilloscope for the waveform, the camera took a picture of the fluid with both the transducer and the hydrophone visible.The distance between the center of the hydrophone was away from the transducer face was calculated. Between the six seconds interval between recordings, the hydrophone was slid slightly either forward or backward in the fluid. The RMS of the measured hydrophone voltage was then taken after the initial transient of the pressure wave had subsided The RMS of input waves with a frequency of 900 kHz has been plotted and can be seen shown in Figure 5.4. This experimental RMS data is plotted alongside the analytical RMS wave pressure generated using Equation 5.15 on page 26 after it has settled. A damping coefficient of 0.6 was used, and an added positional offset was added to the modelled wave to help align the modelled data with the experimental data. This position delay was added because the true speed of sound of the fluid is not known and therefore, the lack of alignment is assumed to be due to this. This is deemed acceptable

because this analysis is more interested in testing to what extent the wave equation is able to capture the relative change of wave position RMS as a function of changing position.

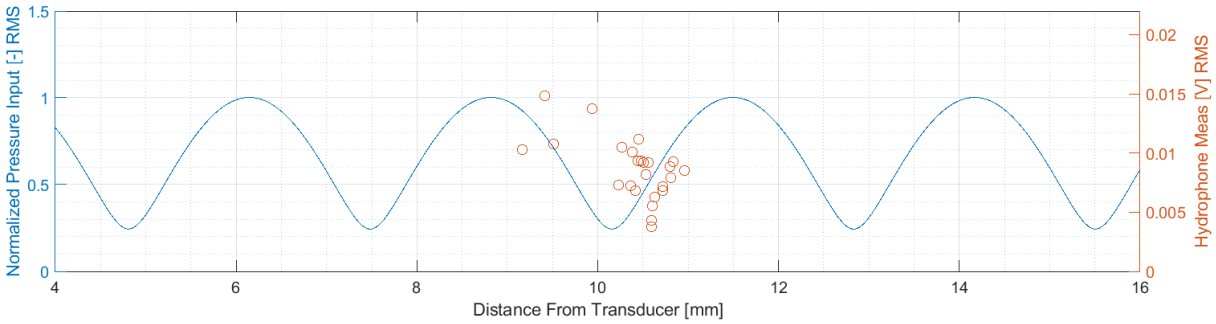

Figure 5.4: This figure shows a comparison of the steady state RMS of the wave equation as stated in Equation 5.15 as a function of position and the RMS of experimentally measured pressure waves at 900 kHz.

It can be seen that the trends of Figures 5.4 correspond well with the modelled waves. It can be noted that movement of the hydrophone between samples was difficult to perform over a larger range of positions than what was plotted in Figure 5.4. This is due to the wavelength of the pressure wave at 900 kHz being approxiamtely 2.5 mm and the measurements were taken by hand.

Transient Response

For the wave transient comparison, the hydrophone was used to record a waveform every 6 seconds. Just before querying the oscilloscope for the waveform, the camera took a picture of the fluid with both the transducer and the hydrophone visible.

Four waveforms have been selected to be compared to the measured responses and can be seen plotted in Figure 5.5. It can be noted that the amplitude of the axis of all Figures is held constant. This is because the output amplitude of the pressure wave that the transducer produces is the same regardless of distance and allows for the visualization of the relative changes in amplitude.

It can be seen from Figure 5.5(a) through 5.5(d) that, the transients of the modelled waves appear to correspond well with the overall tendencies of experimentally measured data.

When looking at the plots shown in Figure 5.5, it can be seen that the pressure starts at zero with a delay before the pressure wave starts. This is because, as modelled, the pressure wave has to first propagate to the location of the hydrophone. In the case plotted, this distance is in between 9 and 11 mm relative to the cabin length's 22.83 mm. Throughout all figures, the pressure wave has fully settled at around 100 micro seconds. The time it takes for a wave to propagate from the transducer to the opposite wall of the cabin is approximately 16 micro seconds. It can be seen from the figures that number of reflections it takes to achieve pressure field steady state time state is approximately 6 reflections, or 100 µs.

Figures 5.5(b) and (d) appear to correspond particularly well with the analytical approximation. The distances from the transducer causes the analytical expressions of the pressure wave to be near maximums and minimums for (b) and (d) respectively. This corresponds to the hydrophone being close to the node and anti nodes of the pressure field. This indicates that the analytical approximation appears to be a good approximation for the wave generated by the transducer.

It can be noted that the transducer dynamics have been chosen to be ignored for the analytical wave expression. This results in the blocky nature of the wave approximation. While the step change nature of the modelled waves do not precisely reflect the transducer

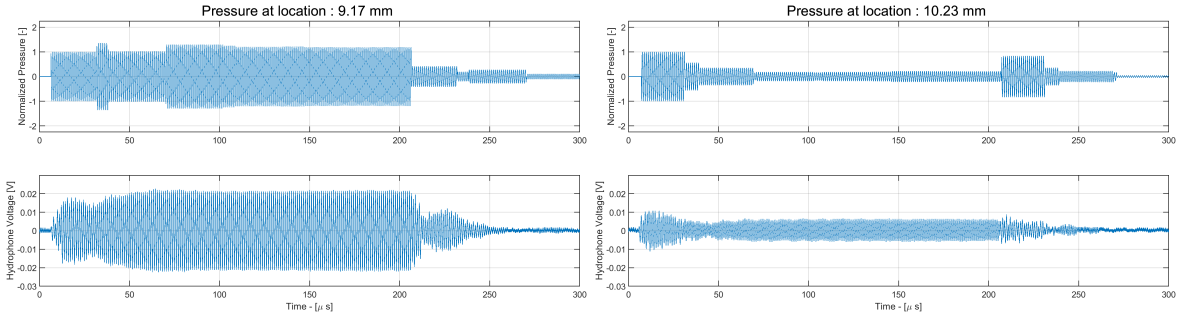

(a) 9.17 mm

(b) 10.23 mm

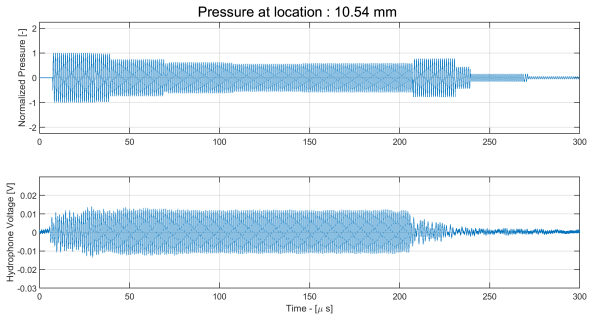

(c) 10.54 mm

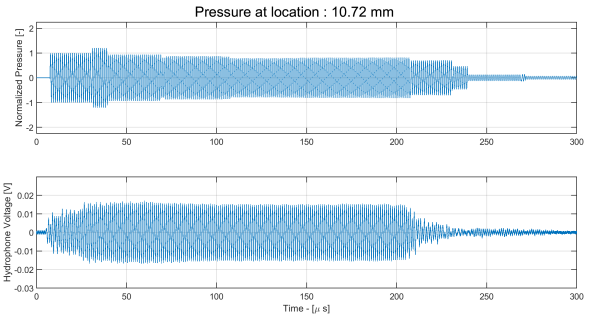

(d) 10.72 mm

Figure 5.5: The top plots in each figure show the force amplitude generated by the transient one dimensional wave approximation at different positions. The bottom plots in each subfigure show the force as measured by a hydrophone submerged in a fluid when the Bentowave transducer is made to generate 200 wavelengths at 700 kHz. The y axis are held constant between the different figures for the experimental data and the modelled waves.

turn on and turn off dynamics, the relative amplitudes appear similar and this assumption is validated.

Comments on Validation

There are several difficulties when comparing the modelled pressure wave response and the recorded one. The angle of incidence between the hydrophone and the generated wave was not able to be controlled, so the exact amplitude of the generated pressure field is difficult to verify. The spatial measurement characteristics of the hydrophone are not known and it could be the case that slightly angle differences could lead to large changes in measured in amplitude. However, the angle appeared to very similar between every queried sample, so this is assumed to be a negligible effect.

Another aspect of this validation that must be considered is that the speed of sound, $c_{l.oo}$ has not been experimentally validated for the given liquid in the fluid and has been taken as an approximate value for this type of fluid. The pressure field has also only been measured at discrete points at different distances away from the transducer face and, as such, the full continuum of the pressure field cannot be known. For these reasons, it is expected that, at a given distance away from the transducer face, an unknown position error exists in the resultant pressure waves. The positive and negative trend of the pressure amplitude for the analytical expression and the measured data appears to align, and, for this reason, the analytical wave expression is accepted.

As a whole, the proposed wave equation appears to do a good job at representing the experimentally measured pressure wave along a single axis away from the transducer.

5.4 Analytical Acoustophoretic Force Expression

The full derivation and simplification of the acoustophoretic force expression using the transient wave expression is mathematically tedious and can be found in Appendix A. This includes a dynamic model for the transient of the acoustophoretic force during the initial propogation of the pressure wave. The camera that is used by this thesis has a maximum framerate of 50 Hz. This is multiple orders of magnitude slower than the initial pressure wave transient and, for this reason, only the steady state expression is shown in this section.

An expression for calculating the acoutophoretic force up until the mth set of reflections has been shown to be equal the following:

$$F_p(m) = \frac{2 \cdot P_{amp}^2 \cdot \omega}{c} \cdot \sum_{n=1}^{m} \left[\sum_{i}^{n-1} \beta^{2(n+i)-3} \cdot sin\left(\frac{2L\omega}{c}(n-i-1) \cdot L - x) \right) + \beta^{2(n+i)-3} \cdot sin\left(\frac{2L\omega}{c} \cdot ((n-i+1) \cdot L - z) \right) + F_{p,last}(n) \right] \quad (5.24)$$

Where:

$$F_{p,last}(n) = \beta^{1+(n-1)\cdot 4} \cdot sin\left(\frac{2\omega}{c}(L-x) \right) \quad (5.25)$$

Practically, when Equations 5.24 and 5.25 are given numerical values for β, c, ω, and L, an expression for the force field can be expressed as the summation of a single cos and sin function with an angular frequency of $2 \cdot \omega k$, where k is the wave number of the fluid. The final wave field can therefore be expressed as the following, where n is the number of reflections and a_i and b_i are the numerically solved contributions from the i_{th} set of reflections:

$$F_{p,final} = \sum_{i=1}^{n} a_i \cdot cos(2 \cdot k \cdot x) + b_i \cdot sin(2 \cdot k \cdot x) = F_{amp} \cdot sin(2 \cdot \lambda \cdot x + \phi) \quad (5.26)$$

This allows for easy modelling of the system during steady state. The derivation from the force contribution from the velocity field, **V** at steady state, is the same as that for the pressure field due to the velocity field simply being a 90deg phase shifted version of the pressure field with a static gain [17]. This is given as the following:

$$F_v(n) = F_p(n) \cdot \left(-\frac{i}{\omega \cdot \rho} \right)^2 \quad (5.27)$$

Therefore, the the total acoustophoretic force is given below:

$$F_{ap} = \frac{4 \cdot \pi}{3} \cdot r_p^3 \cdot \left(\frac{2}{3} \cdot \tilde{\kappa} \cdot f_1 \cdot F_p(n) - f_2 \cdot \rho_l \cdot F_v(n) \right) \quad (5.28)$$

5.5 Analysis of the Dynamic Acoustophoretic Force

In this section, the acoustophoretic model presented in this chapter are now shown under different operating conditions. Unless otherwise stated, the parameters of this analysis are that shown in Table 5.1. These values are taken as they are used when validating the acoustophoretic forces in Chapter 6 and, as such, variance from these values give insights relevant to the interests of this thesis. Variance of the following parameters are considered; pressure wave frequency, reflection coefficient of the chamber.

Table 5.1: This is the table over initial parameters in this section

Parameter	Description	Value	Units
L	Distance from transducer to wall	22.83	[mm]
ρ_a	Density of Air	1.27	[kg/m^3]
c_l	Speed of sound in Olive Oil	1500 [26]	[m/s]
c_a	Speed of sound in Air	343[14]	[m/s]
ρ_l	Olive Oil Density	860	[kg/m^3]
P_{amp}	Pressure Wave Amplitude	1	[kPa]
β	Reflective Damping Coefficient	0.6	[]

Acoustophoretic Force as a Function of Frequency

The model presented in this chapter shows that acoustophoretic nodes and antinodes are be present along the x axis at a position that is dependent on the frequency. This can be observed for three frequencies in Figure 5.6.

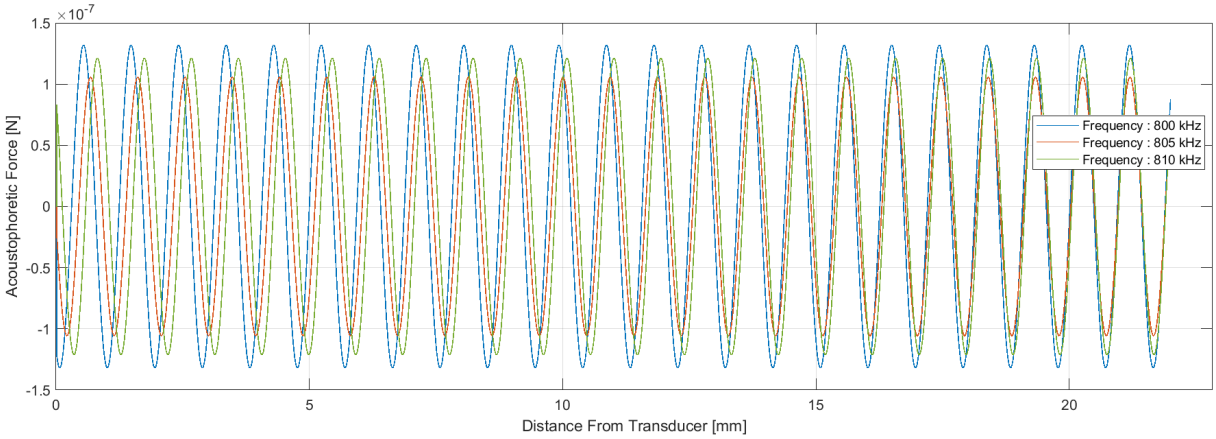

Figure 5.6: This figure shows the time averaged acoustophoretic as a function of distance from the transducer.

The first observation that can be made from Figure 5.6 is that the time averaged force field oscillates between a maximum and minimum value in a sinusoidal manner over the x axis. It can be found that the distance between oscillations is half the wavelength of the pressure field present in the fluid. Should a particle or air bubble be at a position where the force is not zero, it will experience a force in the direction of then nearest pressure node. The node of this wave is one of two equilibrium points that a bubble could find itself at. The other is that of a half wavelength away from a node, as no forces will be acting on the particle in this position. However in reality, streaming effects that exist in the fluid will push the bubble away from this position, so further consideration of it will not be made.

Another observation that can be made is that, as the transducer frequency is changed, the location of the node is also changed. The relative change of the node appears to be lesser, the closer it is to the opposing end of the chamber. This can more clearly be seen shown in Figure 5.7.

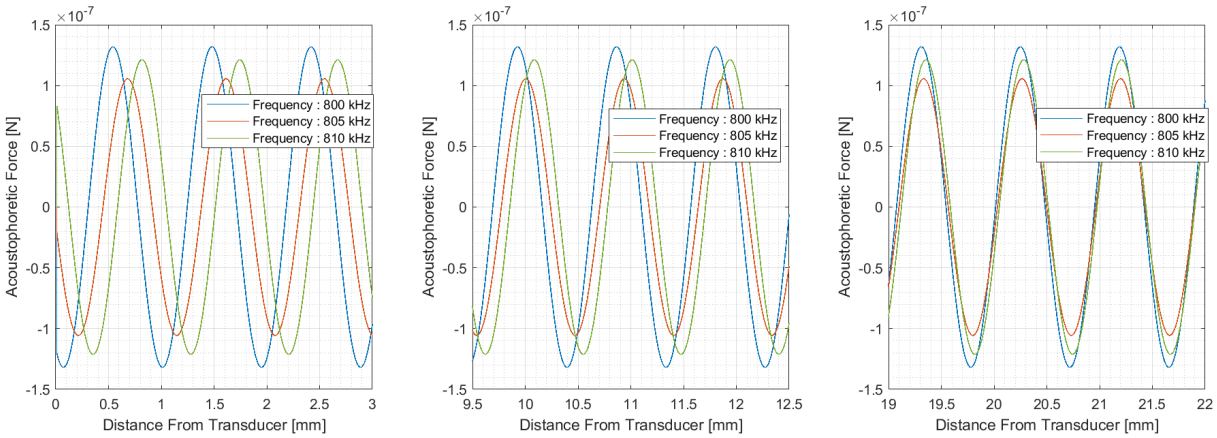

Figure 5.7: This figure shows the change of the acoustic field plotted at three different distances from the transducer. (Left) : 0 to 3mm. (Middle) : 9.5 to 12.5 mm. (Right) : 19 to 22 mm. This figure highlights relative movement of the maximum and minimums of the field at three different distances from the transducer.

From Figure 5.7, it can be seen that the movement of the node moves as a function of frequency and original node position. When looking at the left plot of Figure 5.7, the peak location change from a frequency of 800 kHz to 810 kHz is approximately .4mm. Comparing this to the right plot, the same change in peak location appears to be less than .1 mm. This shows that the nodes move much more as function of change in frequency the closer it is to the transducer with almost no movement at the maximum distance away from the transducer.

The movement of specific nodes as the input frequency is changed has been plotted in Figure 5.8. Nodes at approximately 0, 5, 12, 17, and 20 mm are shown to move over the frequency range of 600-800 kHz.

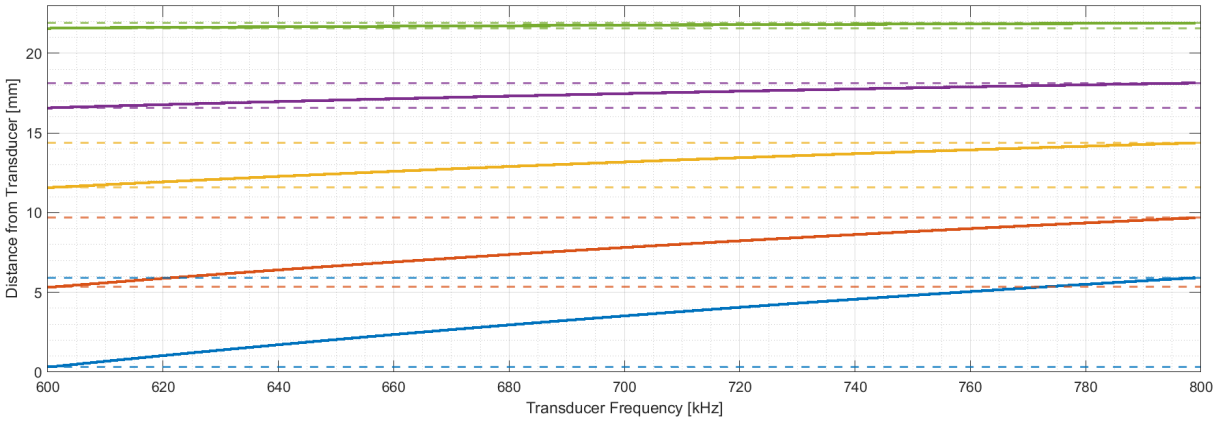

Figure 5.8: This figure shows the movement of node postions as a function of frequency. The different full colored lines at the beginning of the x-axis (600kHz) is where the initial node positions are. The different colors refer to the different start positions of the individual nodes with the dotted lines showing the upper and lower bounds of the given node's movement. (Blue) moves 6 mm, (Red) : moves 4mm (Yellow) : moves 3 mm. (Purple) Moves 2 mm, (Green) : Moves 0.2mm.

The fact that the movement of the particle is dependent on the position of the particle also presents a control difficulty. Giving a particle a reference position may not be feasible from a given initial position and frequency, given a limit change of frequency is allowed. One fortuitous observation that can be made from 5.8 is that the movement of the nodes appears to be smooth in the region from 601 to 799 kHz.

5.5.1 Acoustophoretic Force Amplitude as a Function of Damping

It was shown in the previous analysis step, that the amplitude of the acoustophoretic field is dependent on frequency. To more clearly show this dependence, the acoustophoretic force max amplitude has been plotted as a function of frequency over a 100 kHZ span and can be seen shown in Figure 5.9.

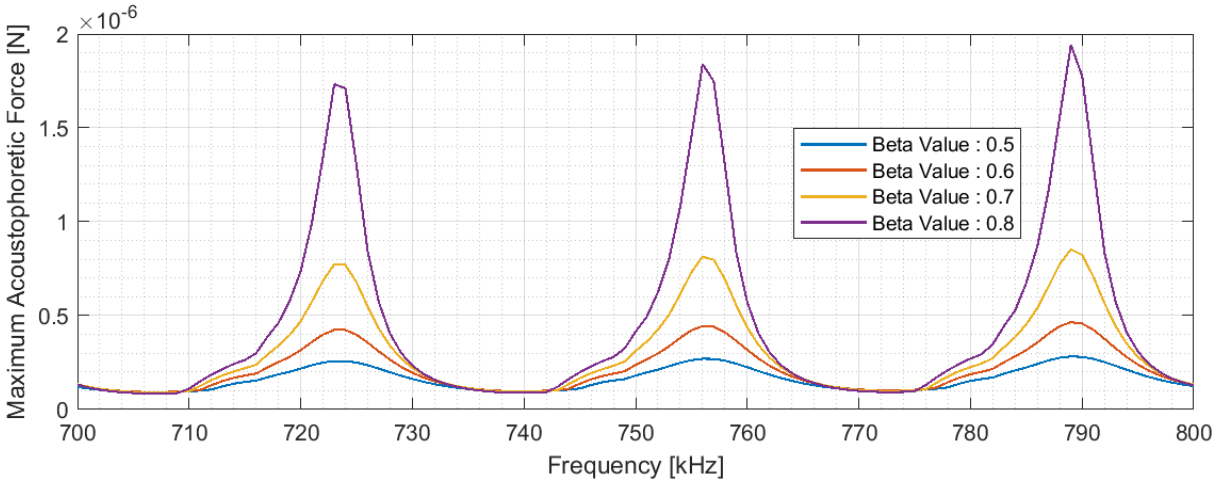

Figure 5.9: This figure shows the maximum value of force a 127μ m air bubble could experience as a function of frequency with a different damping values. The amplitude of the input pressure wave is 1kPa and is the same for every beta value.

In Section 5.3.3, it was found that a damping coefficient, β that seemed to fit reasonably well with the experimental data was a value of 0.6. For a beta value of 0.6, the maximum to minimum acoustophoretic force relationship is approximately a factor of 4. If the reflectivity is greater that this, then the ratio between the maximum and minimum force will become greater. An interesting thing to note is that the minimum force appears to be independent of damping coefficient. This means that, if the input to the system is the wave frequency, the input gain always has a minimum value and that particle position actuation through the use of acoustophoretic force should always be feasible.

5.6 Conclusion

In this chapter, a derivation of the dynamics pressure field has been derived and validated. A dynamic model for the acoustophoretic force as a function of fluid and particle parameters has been derived.

The expected relationship between acoustic wave frequency and force amplitude has been shown to be nonlinear, though apparently periodic as a function of frequency and shown to be bounded with respect to amplitude and continuous. The fact that the acoustophoretic force can be shown to maintain a minimum value and sign suggests that control of individual particles, if the contrast factors are large enough, should be possible to design.

Chapter 6

Air Bubble Modelling

Chapter Abstract

In this chapter, a model for the movement of particles is proposed and validated. The model consists of using Newton's second law to define the equation of motion for air bubbles. The motion along the horizontal axis has been shown to mostly be due to the viscous damping component of the fluid and the acoustophoretic force. The vertical movement has been shown to be due to viscous effects and buoyancy. It was shown that when the acoustophoretic force is present in the cabin, the viscous damping effect appeared to be lower, though this is interpreted as being part of an unknown streaming disturbance force in the fluid. Experimentally, bubbles were shown to move and settle at the acoustic nodes in the fluid, thus validating the x axis component of the acoustophoretic force expression.

6.1 Introduction

This chapter presents the actuation potential of air bubbles in commercially available olive oil by the acoustophoretic force. Olive oil has been selected at the fluid medium due to its high viscosity which acts to limit the terminal flotation velocity caused by the inherit buoyancy of the air bubble.

In this chapter, the general equations of motion are presented for a particle in a fluid with and without sonication. After this, the acoustophoretic force model is validated with experimental data. The findings of this chapter will be used when designing control structures for particles in the following chapters.

This chapter will be broken up into the following sections:

- Section 6.2 : Air Bubble Motion Without Pressure Field
- Section 6.3: Air Bubble Movement With Pressure Field Present

6.2 Air Bubble Motion Without Pressure Field

In this section, the motion of air bubbles are analyzed when no acoustic pressure field is present in the chamber. Air bubbles' vertical motion in olive oil are analyzed. This is done so that the viscous force can be found and is required to model the horizontal movement of air bubbles when the acoustic field is present.

The force balance for an air bubble along the vertical axis experiencing is assumed to consist of three components; a viscous damping component, a buoyancy force, and an unknown

streaming effect. The unknown streaming effect is due to turbulent motion in the fluid affecting the air bubble. This turbulence occurs because air bubbles are forcefully added to the fluid in order for there to be air bubbles present.This causes a turbulent internal fluid flow in the chamber. The force due to turbulence is not analyzed in this chapter, but acknowledged to be present in the motion measurements. The force balance can be expressed as the following along the vertical axis, y:

$$M \cdot \ddot{y} = F_{visc} + F_{bouy} + F_{streaming} \tag{6.1}$$

In this chapter, the viscous damping force is assumed to only be a linear function of the velocity of the particle and therefore the Stokes Drag force is used.[4]. The Coloumb and Stiction based nonlinear properties of the friction are chosen to implicitly be included in the unknown streaming disturbance present in the fluid. The particles in this chapter are assumed to be spherical in shape and therefore, the orientation of the particle does not affect the amplitude of the force. The viscous force can therefore be expressed as the following:

$$F_{visc} = -B_{visc} \cdot \dot{y}, \qquad B_{visc} = r_p \cdot \mu \cdot 6 \cdot \pi \tag{6.2}$$

Where μ refers to the dynamic viscosity of the fluid. Equation 6.1 can be rewritten into a state space formulation in the following manner:

$$\dot{\mathbf{x}} = \mathbf{A} \cdot \mathbf{x} + \mathbf{B} \cdot (F_{bouy} + F_{streaming}), \quad y = \mathbf{C} \cdot x \tag{6.3}$$

Where

$$\mathbf{A} = \begin{bmatrix} 0 & 1 \\ 0 & -\dfrac{B}{M} \end{bmatrix}, \quad \mathbf{B}_{visc} = \begin{bmatrix} 0 \\ \dfrac{1}{M} \end{bmatrix}, \quad \mathbf{C} = \begin{bmatrix} 1 & 0 \end{bmatrix}, \quad \mathbf{x} = \begin{bmatrix} y \\ \dot{y} \end{bmatrix} \tag{6.4}$$

F_{bouy} is the difference between the up-drift and gravity forces on the particle given as the following:

$$F_{bouy} = F_{up} - M \cdot g \tag{6.5}$$

With the upthrust, F_{up} being given as the following, where ρ_l is the density of the liquid, V_b is the volume of the spherical particle, and g is the gravitational constant taken to be 9.82.

$$F_{up} = \rho_l \cdot V_b \cdot g \tag{6.6}$$

The mass of the air bubble can be seen as the following:

$$M = \frac{4\pi}{3} \cdot r_p^3 \cdot \rho_{air} \tag{6.7}$$

Drag Coefficient of Air Bubble

When the air bubble rises due to buoyancy, it will attain a terminal velocity, $\dot{y}_{term}$ whereby the buoyancy force is equal to the drag force. This terminal velocity can be seen as a function of particle radius by using Equation 6.1 and setting the acceleration to 0:

$$\dot{y}_{term} = \frac{2\,g\,{r_p}^2\,\rho_l - 2\,g\,{r_p}^2\,\rho_{\text{air}}}{9\,\mu} \tag{6.8}$$

For validation, the positions of a series of air bubbles in olive have been recorded at room temperature as they float to the top of the liquid. The dynamic viscocity, μ of olive oil is taken to be 0.04 [3]. It has, on review of this thesis been shown that this viscocity of olive oil is appropriate for an olive oil temperature of approximately 40 degrees Celcius. At a

temperature of 25 degrees, the viscocity has a value of 0.08. The terminal velocities can be seen plotted as a function of bubble radius alongside Equation 6.8 as a function of the r_p in Figure 6.1 for olive oil at a temperature of 40 degrees and 25 degrees.

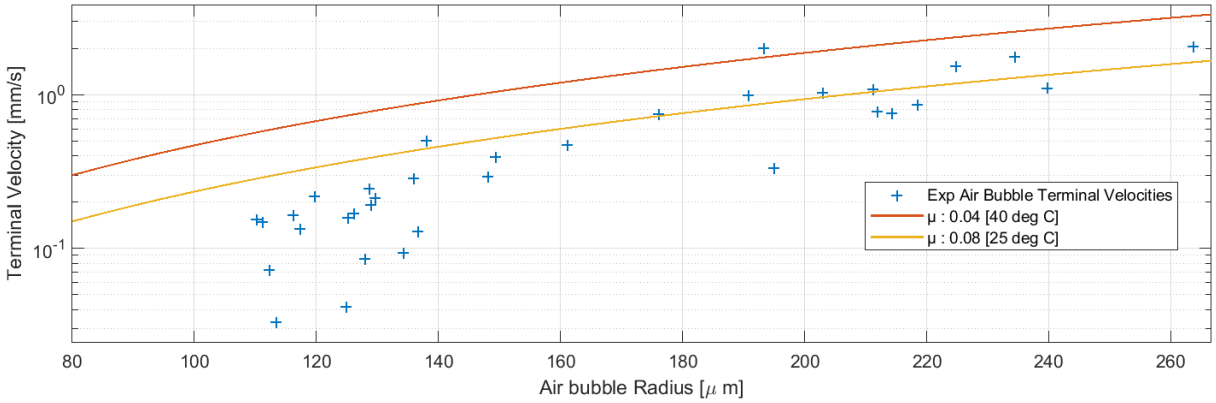

Figure 6.1: Comparison of the analytical and experimental terminal velocities of air bubbles where ρ_l = 860, μ =.04. The orange and yellow lines are the analytical estimated terminal velocity and the dots are the terminal velocities of measured air bubbles.

It can be seen from Figure 6.1 that the terminal floating velocity of air analytical expression becomes very poor for air bubbles with a lower radius than 160 µm. There are two possible reasons for this. The first is likely due to the method of calculating the bubble radiuses. The image detection algorithm uses an edge detection algorithm to define where the air bubbles are. The edges that are observed in the images are dark lines that are several pixels thick. This outer edges of these dark circles are what is defined as the particle radius. For a bubble radius of 120m, the diameter of the bubble is approximately 16 pixels wide. This means that if the true inside of the bubble is first after a layer of 3 or 4 dark pixels, it is very likely that the bubble radius would be overestimated by approximately a factor of 2.

Another reason why the estimate is poor is due to the fact that the frictional properties for small air bubbles may not be the same for larger bubbles. It could be reasoned that, as the air bubbles reduce in size, the energy required to cause small movements in the fluid does not scale linearly in comparison to when a larger amount of fluid is moved. Further exploration of this is beyond the scope of this thesis.

Due to aforementioned oversight by the author, the kinematic viscocity of the olive oil is taken to be 0.04 throughout the remainder of the thesis.

6.3 Air Bubble Movement With Pressure Field Present

In this section, the acoustophoretic model derived in Chapter 5 is validated. This section is broken up into validation sections: a qualitative validation where attraction of air bubbles to the modelled acoustophoretic nodes is demonstrated, and a parametric analysis in order to determine the amplitude of the acoustophoretic force. The bounding equation of motion for an air bubble's x axis motion is given as the following:

$$\ddot{x}_p = F_{ap} - B \cdot \dot{x}_p + F_{streaming} \tag{6.9}$$

The nonlinear state space representation of particle movement is therefore taken to be

$$\dot{\mathbf{x}} = \mathbf{A} \cdot \mathbf{x} + \mathbf{B} \cdot \left(F_{ap} + F_{streaming}\right), \quad y = \mathbf{C} \cdot x \tag{6.10}$$

Where

$$\mathbf{A} = \begin{bmatrix} 0 & 1 \\ 0 & -\frac{B}{M} \end{bmatrix}, \quad \mathbf{B}_{visc} = \begin{bmatrix} 0 \\ \frac{1}{M} \end{bmatrix}, \quad \mathbf{C} = \begin{bmatrix} 1 & 0 \end{bmatrix}, \quad \mathbf{x} = \begin{bmatrix} x_p \\ \dot{x}_p \end{bmatrix} \tag{6.11}$$

6.3.1 Qualitative Acoustophoretic Force Validation

In this section, the trends of bubbles moving towards the acoustic nodes due to the acoustophoretic force is demonstrated. This is tested by applying pressure waves to the chamber filled with olive oil when bubbles were present. The frequency of the input wave is then increased at approximately one second intervals. This has the effect of changing where the nodes are in the fluid, causing a force to be present on the particle until its position settles at a node. The movement of multiples particles as the frequency being generated by the transducer is changed can be seen shown in Figure 6.2.

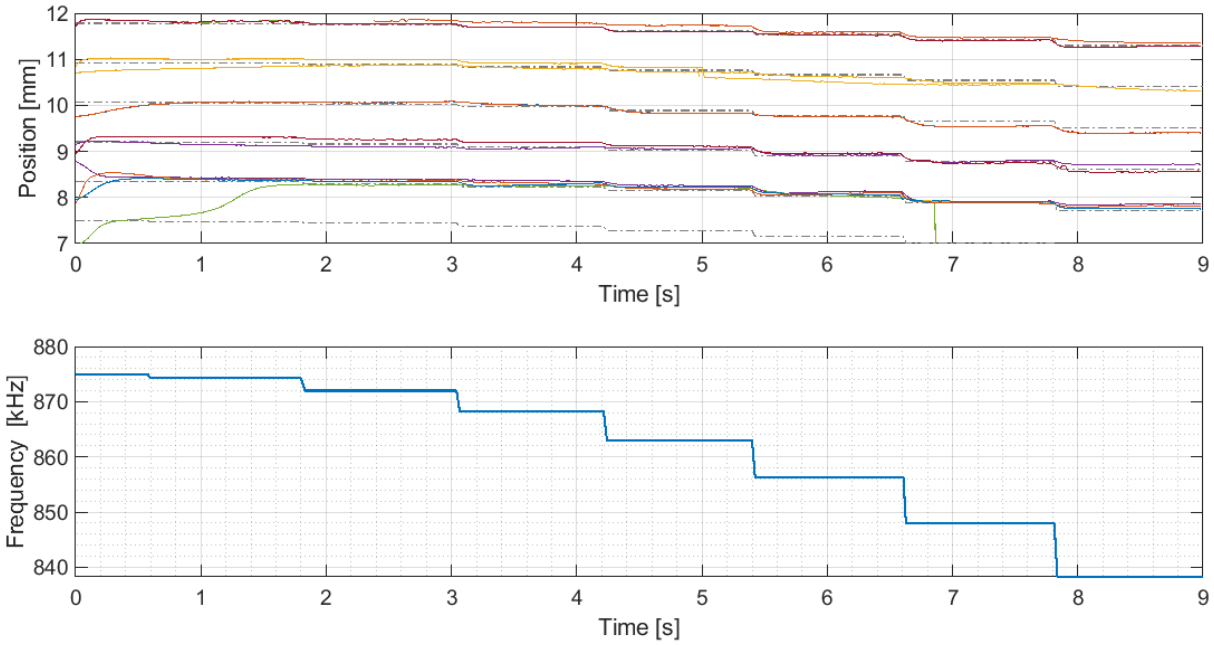

Figure 6.2: This top plot shows bubble position as the frequency generated by the transducer is changed and the bottom plot shows the driving frequency of the transducer. The voltage of the transducer is held constant at 150V peak to peak. The dotted lines in the top figure show the calculated node positions and the colored lines represent experimentally found bubble positions as acquired from analyzing video footage.

It can be seen from Figure 6.2 that the bubbles are attracted to the pressure nodes in the fluid. It was also observed that bubbles would sometimes travel from the nodes closer to the transducer to nodes further away from the transducer. An example of this can be seen at approximately 1 second on the bubble being represented by the green line. This bubble moves from the node at approximately 7.5 mm to the node at approximately 8.5. This effect was observed to occur more frequently for bubbles closer to the transducer. This is assumed to be due to the pressure wave having some degree of damping as a function of wave travel distance. Before the pressure wave has any reflections, its amplitude is the greatest. It could be theorized that, if this wave component with the highest amplitude has a position dependent damping, this would create a force gradient with a maximum value at the transducer face and minimum at the opposite chamber wall. The influence of this effect would then be attenuated for every consecutive wave reflection. This effect was found to occur more often, the closer the transducer was run to the transducer's resonant frequency of 960 kHz where the pressure

wave output is greatest. However, this effect did not occur very often, and would mostly occur when the turbulent flow was greatest. It is therefore considered to be a part of the unknown streaming force.

It can be surmised from Figure 6.2 that the qualitative property of the acoustophoretic forces attracting air bubble to the nodes of the quasi standing waves appears to be validated.

6.3.2 Parametric Analysis

From the acoustophoretic equation presented in Section 5.2 , it is shown that the amplitude of the acoustophoretic force is dependent on the square of the pressure amplitude of the wave. The actual amplitude of the pressure fields present in the fluid is not given by the transducer manufacturer[2] and difficult to measure experimentally, and for this reason, the pressure wave amplitude has been fitted to experimental data.

A single particle from the data in Figure 6.2 has been taken and has been plotted in Figure 6.3. The input frequency provides concurrently larger input frequency steps to the system and this allows for showing the acoustophoretic model over a large range of the changed node locations and current bubble positions.

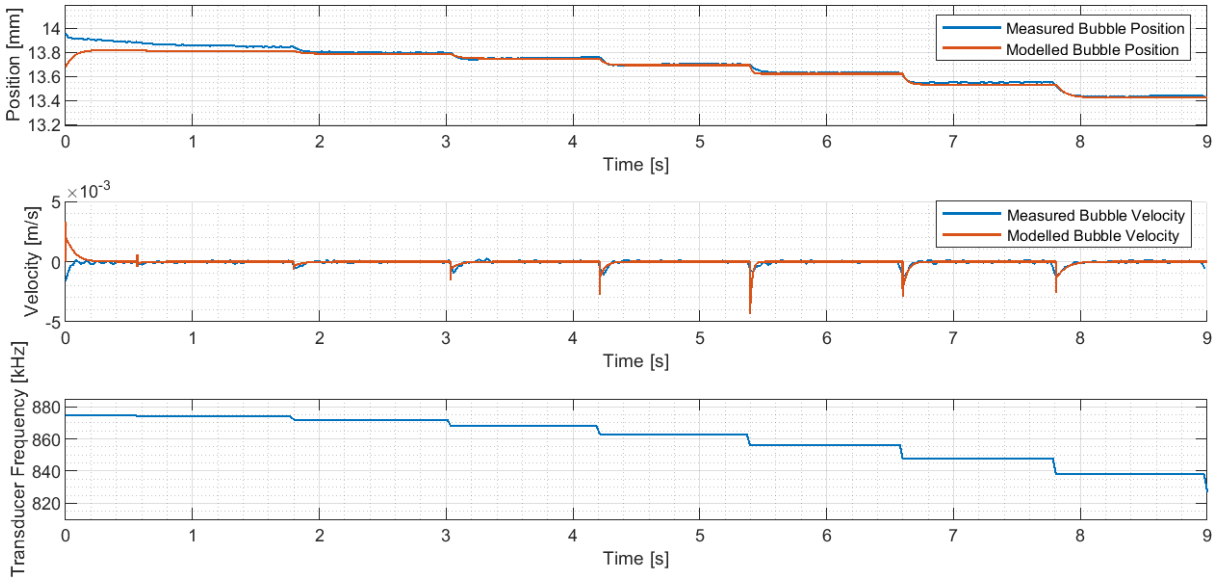

Figure 6.3: This figure shows the movement of a particle when affected by different input wave frequencies by the transducer. An offset of 0.3 mm is added to the modelled data to make them lie on top of each other. The modelled pressure wave amplitude is set to be 1 kPa and the fluid viscosity is set to .04. The particle radius here is measured and modelled to be 145 µm.

The disturbing acoustic streaming force has a stochastic element and which can cause the bubble to not lie directly at a given acoustophoretic node. An example of this can be seen in Figure 6.3 between 0 and 2 seconds. This is because the acoustophoretic force is a force that is greater the further away from the acoustic node the bubble is and therefore a relatively small acoustic streaming force could displace the bubble slightly. Multiple frequency change steps to the bubble are therefor necessary to properly validate the movement of particles.

It appears to be the case that the experimental bubble dynamics shown in Figure 6.3 aligns very well with the modelled bubble bubbles. Both the steady state movement of nodes and the velocity of the air bubbles as the pressure wave frequency is changed appear very similar to each other. While more rigorous analysis could be performed to find a better value for the pressure wave amplitude, the results appear to align well enough that it would be unclear

to what extent a greater numerical analysis of system parameters would provide a benefit and not just result in over fitting . For this reason, a pressure wave amplitude of 1kPa and a damping coefficient of 0.6 are accepted.

It was shown in the acoustophoretic force analysis in Section 5.5 that the change of the nodes relative to the change in frequency became less pronounced the further away from the transducer the bubbles were. To show that this also is the case experimentally, a number of bubbles are plotted at varying distances from the transducer and can be seen in Figure 6.4.

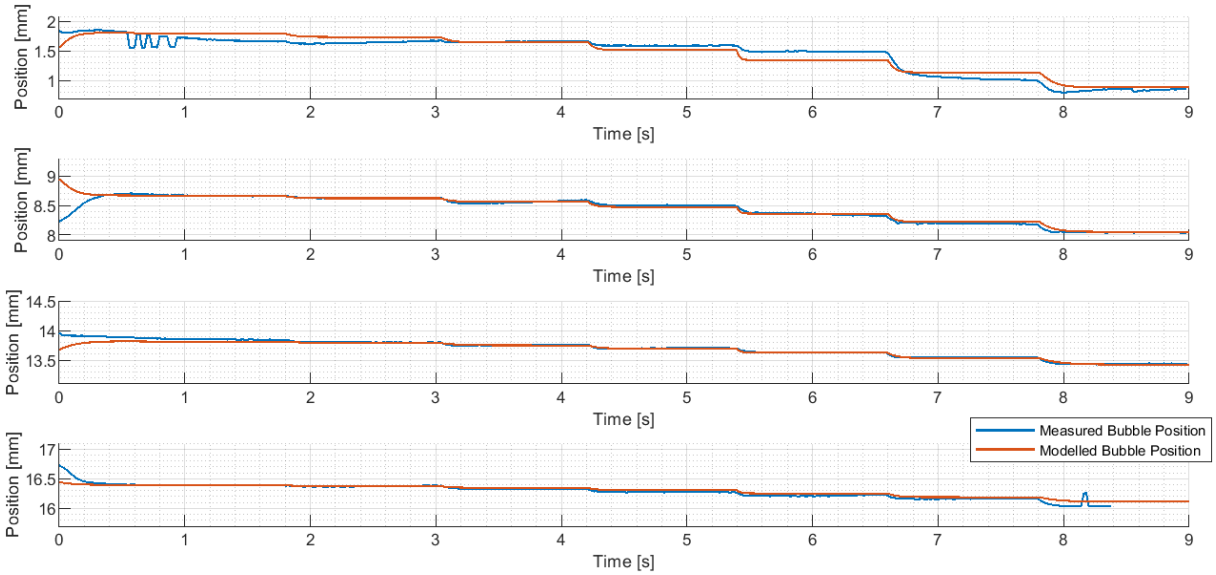

Figure 6.4: This figure shows how multiple bubbles move the same input frequency timeseries. The axis limit ranges are the same for all figures. The air bubbles radiuses are, from the top to bottom, : 133, 127, 101, and 105 micro meters. The input transducer frequency is the same as Figure 6.3. The movement of the modeled total node movement from the top figure down to the bottom figure are : 0.90 mm, 0.63 mm, 0.39 mm, and 0.28 mm. The axis limits are held the same in all plots to show the different absolute node movements.

It can be seen when comparing the bubble positions in the top and bottom plots of Figure 6.4 at 1 and 8 seconds that the total movement of both the measured and modeled bubbles reduces the further away from the transducer. The movement characteristics of the modelled and experimental data align very well for the four different bubbles shown.

To show that the the model for air bubble movement is appropriate, an air bubble with a size of 101 micro meters has been taken from Figure 6.4 and its velocity has been compared with simulated bubbles using different bubble radiuses in Figure 6.5.

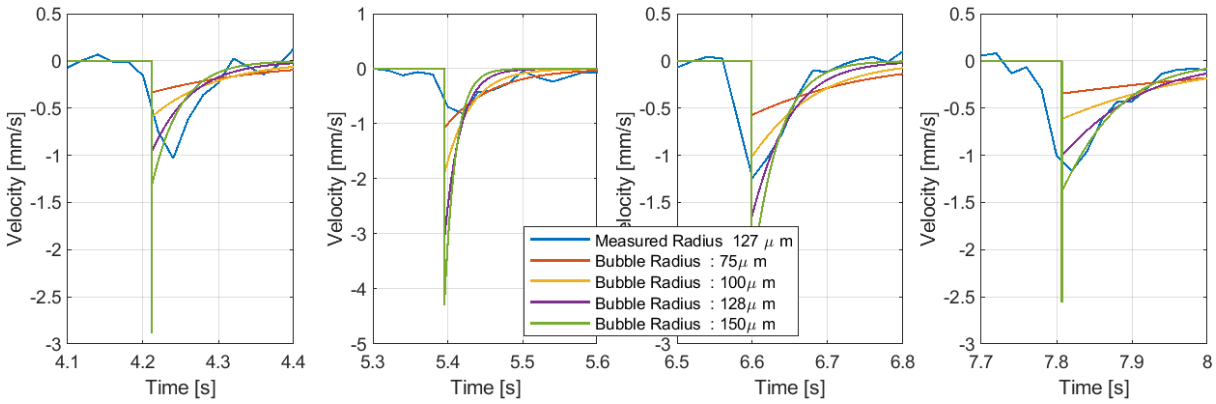

Figure 6.5: This figure shows the measuremtent velocity of a bubble simulated with the inputs of Figure 5.5 **WATCH THIS** compared to simulations of the same inputs whereby the radius is different from the measured data. The subplots show only when the input frequency is changed.

It can be seen in Figure 6.5 that for first, third and fourth figure, using the experimentally measured bubble radius causes the velocity of the modelled data to best align with the measured. It can be seen, however, that the peak value of the measured velocity does not necessary equal the peak value of the simulated. This could be due to the liquid parameter uncertainty, amplitude of the simulated pressure waves not aligning with the experimental, or the damping coefficient of the waves not equaling the experimental conditions. However, it is clear that the velocity change of the simulation appears very similar to the experimentally found data.

Analysis Comments

One consideration that must be taken into account when analyzing the motion of the bubble as a frequency reference is changed is the location of the particle relative to the transducer. The video that recorded the fluid with the air bubbles in it did not show the edge of either transducer. With a horizontal video resolution of 1280 pixels and a pixel per meter value of 1.33e-5, the video frame shows approximately 17 mm. While it was not measured it is assumed the center of the video corresponded to the center of the distance between the two transducers. This means that, when measuring from the left side transducer, the particle positions should have an offset of 2.7 mm.

The calculation of the acoustophoretic force is proposed analytically as an infinite sum. However, in order to calculate the force an air bubble would experiences, the expression has been calculated numerically. In order to model this practically, only 15 reflections are taken into account. This is because the amplitude of the reflective bubbles after this many reflections is less than 1e-8 of what the original pressure amplitude is.

6.3.3 Vertical Acoustic Interference

It has been experimentally observed that the presence of a pressure field in the cabin seems to apply a force on the bubble in the vertical direction. This changes the force balance of an air bubble to being the following:

$$\ddot{y} \cdot m = F_{bouy} - F_{drag} + F_{sonication} \tag{6.12}$$

An experimental test was performed under the same conditions as 6.1. However, in the beginning of the video, sonication was enabled for two seconds and then turned of. The

positions of the air bubbles was recorded and their terminal velocites were found. The results of this test can be seen plotted in Figure 6.6

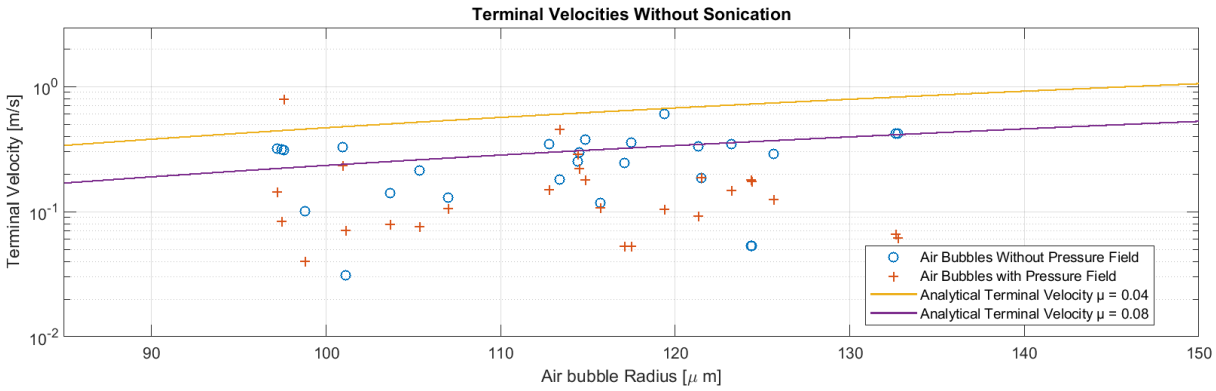

Figure 6.6: This figure shows the analytical expression (yellow and purple) for the expected terminal velocity of particles for air bubbles and the terminal velocity bubbles before and after a 900 kHz sinusoidal wave with a peak to peak voltage of 150 Volts from the Benthowave Transducer is activated. The same bubbles are analyzed with and without the pressure field present.

It can be seen in Figure 6.6 that there is a offset in the average terminal velocities of the air bubbles when the pressure field is present. This corresponds to this pressure field having a vertical force component that is a function to both the velocity of the particle and being depedent to the radius of the bubble squared.

There also appears to be a stochastic element to the change of the damping during the presence of the acoustophoretic force. It is likely that what appears to be stochastic is due to the two or three dimensional nature of the pressure field that is present in the liquid. It can be seen in its datasheet[2] that the Benthowave transducer has a multipole force generation characteristic that is not captured by the 1 dimensional approximation. It is unknown however, to what degree of accuracy one would have to be achieve in modelling before deterministic properties of the pressure waves can be determined with any degree of certainty. For this reason, this off axis force will have to be accepted as an intrinsic part of the system whereby the divergence from the expected force is accepted as system disturbance.

6.4 Conclusion

In this chapter, the model for the aristocratic forces presented in Chapter 5 was validated. The dynamics of air bubbles excited by acoustophoretics is dominated by the characteristics of the acoustophoretic force. The initial position of the air bubbles has shown to play a large role in the potential for actuation by changing the frequency of the pressure wave affecting the air bubble. The similarity between the modelled air bubbles and experimental dynamics means that the nonlinear model can be used as a tool for further developing identification methods and control strategies for air bubbles.

Chapter 7

System Identification of Bubble Movement

Chapter Abstract

This Chapter presents an Extended Kalman Filter used to characterize the unmodelled force affecting the movement of air bubble. The scope and purpose of the system identification methods used are introduced in Section 7.2. In Section 7.3, the model for an air bubble experiencing an acoustophoretic force implemented is implemented in the EKF. The EKF includes a disturbance force state that represents the non-modelled forces in the system. The selection process of the covariances in the EKF is presented which used the nonlinear model of an air bubble with simulated measurement noise to assign variance values which minimizes the error between output of the EKF and the nonlinear model. The disturbance force state of the EKF is then shown to be able to observe the amplitude and duration of a simulated disturbance force affecting the air bubble in the nonlinear model. The disturbance force estimate in the EKF is shown to be sensitive to noise on the measurements. The EKF is then used to observe experimental datasets from frequency step inputs and control data. The node position estimate of the EKF caused the disturbance state to attribute the difference between the experimental node positions and modelled node positions as a disturbance force. The EKF was shown to provide a reasonable estimate for the disturbing streaming force when the air bubble movement was small, but did not provide a good estimate when the air bubble moved far away from the initial node position. The sum of forces in the process model was shown to be able to be used as a potential tool for improving the modelling parameters.

7.1 Introduction

It has been shown in Chapter 6 that the experimentally measured movement of air bubbles corresponds fairly well with the proposed dynamic model of particles excited by the acoustophoretic force. However, there are still distinct points when the model diverges from the experimental data and this has, until now, been accepted to be due to an uncharacterised streaming effect in the fluid. This chapter gives a proposal for characterising this disturbance force on air bubbles with the use of an Extended Kalman Filter (EKF). In the process of developing this EKF, a Linear Kalman Filter was developed. The implementation of the LKF and a discussion of its findings can be seen in Appendix B. This chapter is broken into the following sections:

- Section 7.2 : System Identification Design goals

- Section 7.3 : Extended Kalman Filter
- Section 7.4 : Selection of Covariance Parameters
- Section 7.5 : EKF on Nonlinear Model Data
- Section 7.6 : EKF on Experimental Data
- Section 7.7 : Improving Model Parameters With EKF

7.2 System Identification Design Goals

In this section, the system identification scope, goals, and an overview of the input data used in this chapter are presented.

Scope

The Extended Kalman Filter methods used in this chapter is a parametric method. The expected parametric structure is shown in Figure 7.1.

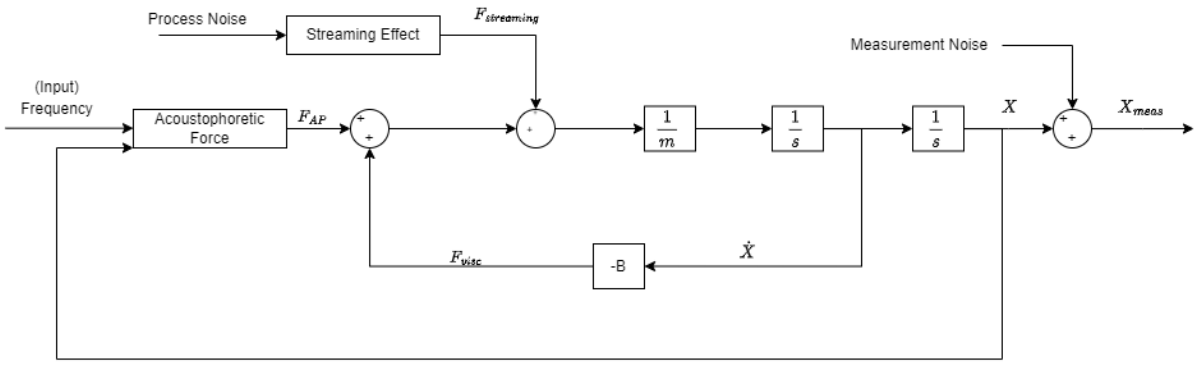

Figure 7.1: This figure shows an approximation of what the system structure is assumed to look like for a bubble's x axis motion. B corresponds to the viscous damping component of the fluid and m refers to the mass of the air bubble.

It can be observed from Figure 7.1 that the streaming effect is modelled as process noise with a streaming effect block. In this chapter, the process noise is assumed to be a stationary white noise input, whereas the streaming effect is some unknown transfer function that gives the streaming force a defined spectral characteristic. In reality, the streaming effect transfer function may not necessarily be a stationary transfer function. However, Kalman Filters have been shown to still give physically insightful estimates of unknown system parameters over a broad range of individual parameter nonlinearities. The Kalman Filters' state estimates are therefore interpreted by the author and discussed as they are shown.

Goal 1: Improved Estimation of System Behavior

There is a lack of an established model for the movement of particles in experimental setups similar to the one used by this thesis. A number of parameters in the dynamic model for air bubbles have been estimated such as the pressure wave amplitude, the exact densities and speeds of sound of the fluid and air bubbles, and the acoustic reflective damping coefficient of the cabin. For this reason, it is not unlikely that the system model parameters could be improved by analyzing the disturbing forces that are not classified by the presented model for

air bubbles. Therefore, improvements to the estimation of air bubbble dynamics will act as a metric for increasing the trustworthiness of the presented model and, therefore, is a desirable system identification outcome for this chapter.

Goal 2: Characterization of Acoustic Streaming Effect

It has previously been established in this thesis that the dominating factors that affect air bubbles during acoustophoretic actuation are: the acoustophoretic force, viscous damping, and a streaming effect of the fluid. While fairly good estimates can be made for the acoustophoretic force and viscous damping effects, it is impractical to try to estimate the streaming force. This is because estimation would require advanced imaging methods or computational fluid dynamic based models that cannot be simulated online. These methods are beyond the scope of this thesis, and the dynamic characterization of the unknown disturbance force using Kalman Filters is assumed to result in a similar outcome at a significantly reduced computational cost. The characterization of this complex disturbance is therefore a desired outcome of the methods used in this section.

Input and Data Selection

For the purpose of the design of the Extended Kalman Filters in this chapter, the system identification time series dataset set is a recorded air bubble that was used in Section 6.3. The air bubble trajectory and pressure wave frequency input can be seen shown in Figure 7.2.

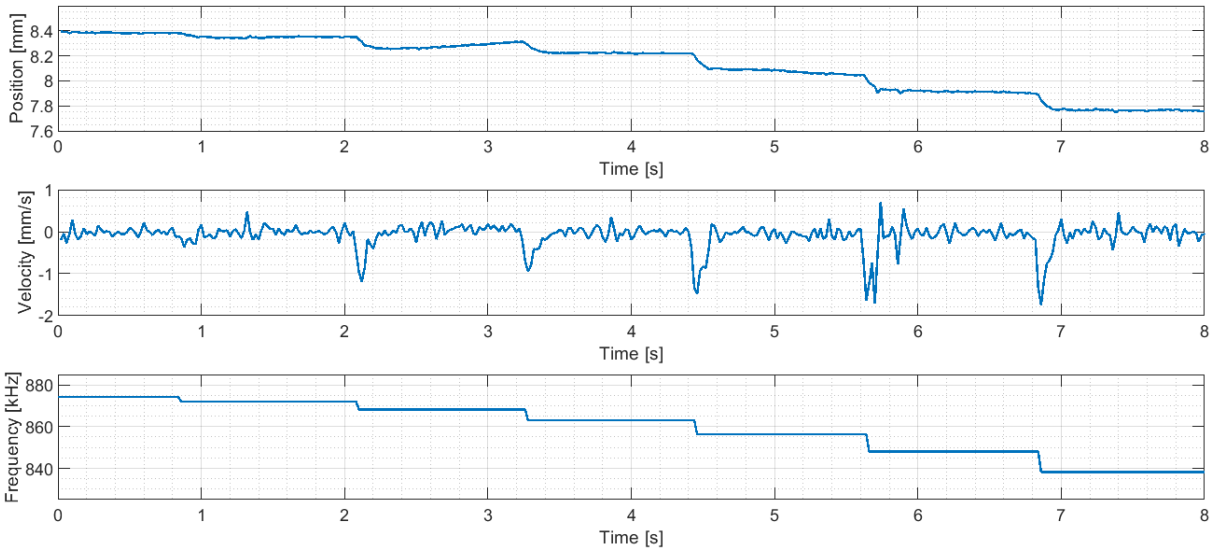

Figure 7.2: This figure shows the position and velocity of an experimentally recorded bubbles. The input freqency to the transducer is shown in the bottom figure. [color=green]The bottom figure needs updating

The input frequency and position dataset begins after the bubble has settled. The step times have also been selected so that the bubbles appears to have settled before the input is changed. The dataset has been selected because it shows how the bubbles responds to different wave frequency step sizes. This has been included because the acoustophoretic force has nonlinear components related to the amplitude of the wave frequency and position of the air bubble. The selected dataset demonstrates the air bubbles moving absolute position and has a wide range of input amplitudes and is therefore an appropriate test dataset.

7.3 Extended Kalman Filter

It has been shown in Appendix B that the Linear Kalman Filter is capable of generating what appears to be a reasonable estimate for what an acoustic streaming is. However, the fact that the estimation of dynamics present in the LKF are required to conform to the static system matrices upon initialization caused the disturbance state to have a hard time being decoupled from the disturbance due to linearization. Nonlinearities have been shown to exist in the amplitude of the acoustophoretic force as a function of the input frequency. Nonlinearities have also been shown to exist in the movement of nodes as a function of frequency. It is therefore beneficial to include these nonlinearities directly in the Kalman Filter and this has done with the use of an Extended Kalman Filter (EKF).

This section consists of first presenting the bounding equations of the EKF, followed by showing an implementation of the acoustophoretic equations in the EKF. [8]

Extended Kalman Filter Bounding Equations

The EKF algorithm consist of two steps: a prediction step where a system process model is used to estimate what the change of the system states is expected to be and an update step where the measured states are used to update the estimated value of the system states. The EKF can be used to estimate system state values given a discrete system in the form :

$$\dot{x}_k = f(x_k, u_k) + v_k, \qquad y_k = g(x_k, u_k) + n_k \tag{7.1}$$

Where $n(k)$ refers to a zero mean Gaussian noise with covariance N that represents the measurement noise, and $v(k)$ refers to the process noise affecting state with covariance M. The covariances are defined as the following, where $E\{x\}$ refers to the expected value of x:

$$E\{v(k) \cdot v^t(k)\} = N \qquad E\{n(k) \cdot n^t(k)\} = M \tag{7.2}$$

The EKF generates an estimate for x, denoted $\hat{x}$, which attempts minimizes the square error of x, where k is a given time step and j are the previous data values. It can be noted that the EKF cannot be said to be an optimal system observer due to the nonlinearities present in the system model:

$$\tilde{x}(k|j) = x(k) - \hat{x}(k|j), \quad min||\tilde{x}(k|j)||^2 \tag{7.3}$$

The state estimate is given by the following expression:

$$\hat{x}(k+1k+1) = \hat{x}(k+1) + \mathbf{K}(k+1) \cdot [y(k+1) - \mathbf{C}_d(k) \cdot \hat{x}(k+1|k)] \tag{7.4}$$

Here, $\mathbf{K}$ refers to the Kalman gain which is updated depending on how similar the measured states are to the process model in the EKF. The physical intuition behind this matrix is that a high relative gain value indicates more faith in the system model and a lower relative gain value indicates more faith in the measurements. The EKF estimation algorithm prediction step consists of the following:

$$\hat{x}(k+1|k) = x(k|k) + T_s \cdot f(x_k, u_k) \tag{7.5}$$

$$P^{-1}(k+1) = \mathbf{A}_d(k) \cdot P(k) \cdot \mathbf{A}_d^T(k) + V \cdot \mathbf{M} \cdot V^T \tag{7.6}$$

Equation 7.5 generates an updated estimate for the value of the x state based on the system model and is shown using a Forward Euler discretization, though other discretization

methods may be used. The discrete Jacobian of the system process model, $\mathbf{A}_d$, for the given timestep and the discrete linearized output matrix $\mathbf{C}_d$ are used when updating the system state error covariance matrix , $\mathbf{P}^-$. To calculate $\mathbf{P}^-$, the previous timestep's predicted state error and the preassigned covariance matrices $\mathbf{M}$ are also used. The system and output matrices are expressed as the following:

$$\mathbf{A}_d(k) = \frac{\delta f(x_k, u_k)}{\delta x_k}, \quad \mathbf{C}_d(k) = \frac{\delta g(x_k, u_k)}{\delta x_k} \tag{7.7}$$

The update step consists of three equations: updating the Kalman Gain in the form of Equation 7.8, updating the state estimate using Equation 7.9 , and updating the error state covariance using Equation 7.10.

$$\mathbf{K}(k+1) = P^-(k+1) \cdot \mathbf{C}_d^T(k) \cdot [\mathbf{C}_d(k) \cdot P^-(k+1) \cdot \mathbf{C}_d^T(k) + N]^{-1} \tag{7.8}$$

$$\hat{x}(k+1k+1) = \hat{x}(k+1) + \mathbf{K}(k+1) \cdot [y(k+1) - \mathbf{C}_d(k) \cdot \hat{x}(k+1|k)] \tag{7.9}$$

$$P(k+1) = [I - \mathbf{K}(k+1) \cdot C_d(k) \ \cdot P^-(k+1) \tag{7.10}$$

In Equation 7.10, **I** refers to an identity matrix with dimensions equal to the number of states.

Implementation of Acoustophoretic Force in EKF

This section shows how the nonlinear acoustophoretic force expression is implemented in the EKF. The expression for the system process matrix can be seen shown in Equation 7.11, where x_p refers to the air bubble position and F_{dist} refers to an immeasurable disturbance state attributed to the streaming effect in the fluid.

$$\begin{bmatrix} \dot{x}_1 \\ \dot{x}_2 \\ \dot{x}_3 \end{bmatrix} = \begin{bmatrix} f_{x1} \\ f_{x2} \\ f_{x_3} \end{bmatrix} = \begin{bmatrix} \dot{x}_p \\ \ddot{x}_p \\ \dot{F}_{dist} \end{bmatrix} = \begin{bmatrix} x_2 \\ \frac{F_{ap}}{m} - x_2 \cdot \frac{B}{m} + \frac{x_3}{m} \\ 0 \end{bmatrix} \tag{7.11}$$

The output state matrix is constant, linear, and represents measuring the position and velocity states of the particle:

$$\mathbf{C}_d(k) = \mathbf{C}_d = \begin{bmatrix} 1 & 0 & 0 \\ 0 & 1 & 0 \end{bmatrix} \tag{7.12}$$

The air bubble is assumed to be settled at the location of a node during the initialization of the EKF. This means that the initial node position can be excluded from the expression of the acoustophoretic force. The acoustophoretic model presented by this thesis has been shown to be good at predicting the movement of particles and nodes, but has offset errors for the location of specific nodes. If this initialization offset is added to the acoustophoretic force equation for a specific bubble, the fluid streaming disturbance force will not have to take into account this disturbance. The acoustophoretic force, F_{ap}, can therefore be approximated as the following :

$$F_{ap} = k_f \cdot sin(2 \cdot \lambda \cdot (\Delta x_{node} - \Delta x_p) \tag{7.13}$$

The expression for the system matrix, $\mathbf{A}_d$, is now given using Equation 7.7 :

$$\mathbf{A}_{cont|k} = \begin{bmatrix} 0 & 1 & 0 \\ -2\,k_f\,\lambda\,\cos\left(2\,\lambda\,(\Delta x_{node} - \Delta x)\right) & -\frac{B}{m} & \frac{1}{m} \\ 0 & 0 & 0 \end{bmatrix} \tag{7.14}$$

The difference between the expression given in Equation 7.14 and the system matrix used for the Linear Kalman Filter is that, for every timestep, k_f, λ, and x_{node} all have to be evaluated. While this puts a higher computational strain on the control system, this demand is still small compared to the image processing involved in air bubble position measurement and is therefore deemed an acceptable inclusion.

The evaluation of the node position for a given timestep is performed in the same manner that is done when performing the initial linearization shown in Section 8.4 on page 70.Repeated briefly, this is done by finding the nearest acoustic node using a 1D search algorithm to define this node position as being where the acoustophoretic force is a minimum. The difference between the nearest node and the initial air bubble position is subtracted from the node position in initialization of the EKF. The movement of this found node is then calculated for every timestep as a function of the input frequency.

The amplitude of k_f is found by using a lookup table that has been found at 1 kHz frequency interval. The k_f value can be seen plotted as a function of frequency in Figure 7.3.

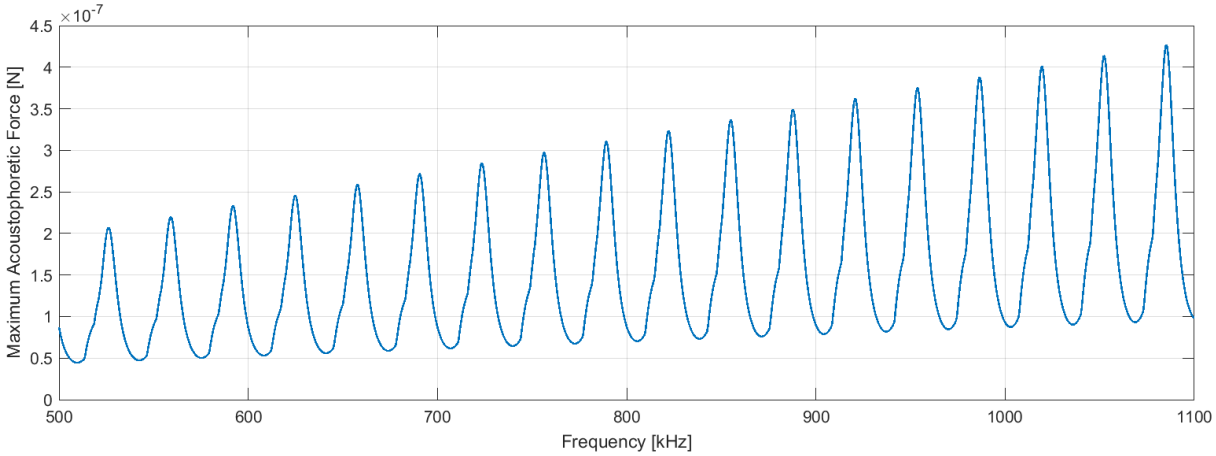

Figure 7.3: This figure show the maximum acoustophoretic force an air bubble with a radius of 100 µm experiences as a function of frequency.

The state estimation is performed using a Forward Euler Approximation in the following form :

$$\begin{bmatrix} x_{1.k+1} \\ x_{2.k+1} \\ x_{3.k+1} \end{bmatrix} = \begin{bmatrix} x_{1.k} \\ x_{2.k} \\ x_{3.k} \end{bmatrix} + T_s \cdot \begin{bmatrix} x_{2.k} \\ \frac{1}{m}\left(-2 \cdot k_{f.k} \cdot \lambda_k cos(2 \cdot \lambda_k \cdot (\Delta x_{node.k} - \Delta x_{1.k})\right) \\ 0 \end{bmatrix} \tag{7.15}$$

It has been found, when implementing the EKF in Simulink, that using the camera's framerate of 50 Hz as the sample rate for the state estimation, the EKF does not produce a meaningful estimate for the system state and state estimation blowup occurs. This is assumed to be because the movement and acceleration of a particle between sample steps is too large to accurately estimate accurate state positions. The solution for this instability is to perform oversampling in the state estimation. The state estimation step time has therefore been set

to $1e-4$ s. This means that the state estimation runs approximately 200 times between each frame. The rest of the EKF algorithm still uses the camera frame rate as a sample time and only samples from this over sampled state estimation every time a new frame is processed. This has been shown to provide calculation stability. It can be noted that k_f and the node position change are also only updated with the framerate. This is acceptable because the the nearest node to the air bubble does not change in the intersample period and the frequency is not changed between framerate samples.

7.4 Selection of Covariance Parameters

One of the challenges present when designing Kalman Filters as trustworthy disturbance observers is the selection of appropriate covariance values. This is because, if the values are selected incorrectly, the output of the EKF will not produce a good representation of the disturbance force present in the system. In this section, the EKF has been implemented in the nonlinear model and the selection process of the noise variances of the process noise and measurement noise values are presented. The initial state covariance, P^- is selected to be zero. The measurement noise matrix, $\mathbf{N}$, state process noise matrix, $\mathbf{M}$, and P^- matrix are defined to be the following:

$$\mathbf{N} = \begin{bmatrix} \sigma_x & 0 \\ 0 & \sigma_v \end{bmatrix}, \qquad \mathbf{P}^- = \begin{bmatrix} 0 & 0 \\ 0 & 0 \end{bmatrix} \qquad \mathbf{M} = \begin{bmatrix} m_x & 0 & 0 \\ 0 & m_v & 0 \\ 0 & 0 & m_d \end{bmatrix} \tag{7.16}$$

It can be seen that there is assumed to be no cross state covariance in the measurement and process noise matrices. This is because states in the system represent physically independent variables where it can be understood that the variables do not interact aside for how they do in the system process model. While adding cross state variances may improve the accuracy of the EKF state estimates, it adds significant complexity to the solution space as it more than doubles the amount of parameters that must be tuned. For this reason the cross state variances has been held at zero.

To add clarity in the presentation for the parameter selection process, the final tuned covariance values are shown in Equation 7.17.

$$\mathbf{N} = \begin{bmatrix} 3.2e-12 & 0 \\ 0 & 3.2e-9 \end{bmatrix}, \quad \mathbf{P}^- = \begin{bmatrix} 0 & 0 \\ 0 & 0 \end{bmatrix} \quad \mathbf{M} = \begin{bmatrix} 2.2e-11 & 0 & 0 \\ 0 & 5.4e-9 & 0 \\ 0 & 0 & 1e-16 \end{bmatrix} \tag{7.17}$$

7.4.1 Measurement Noise Selection

The noise covariance function can be estimated directly from the variance of measured position values when the input to the system is at rest. This can be approximated using the sample covariance as given by the following equation:

$$cov(A, B) = \frac{1}{N-1} \sum_{i=1}^{N} (A_i - \mu_A) \cdot (B_i - \mu_B) \tag{7.18}$$

Where μ refers to the sample means of dataset A and B. Due to the variance of the measured states being the covariance of the measured states themselves, the equation for the sample variance can be used instead:

$$\hat{\sigma}_A = \frac{1}{N-1}\sum_{i=1}^{N}(A_i - \mu_A)^2 \tag{7.19}$$

A section of the identification data has been selected that has been detrended and the sample covariances of the position, σ_{xp}, is 3.2e-12. and the velocity variance is the calculated at the numerical derivative of this value.

To show how the EKF estimates the position and velocity states when being run in the nonlinear model as the covariances deviate from the simulated noise can be seen shown in Figure 7.4.

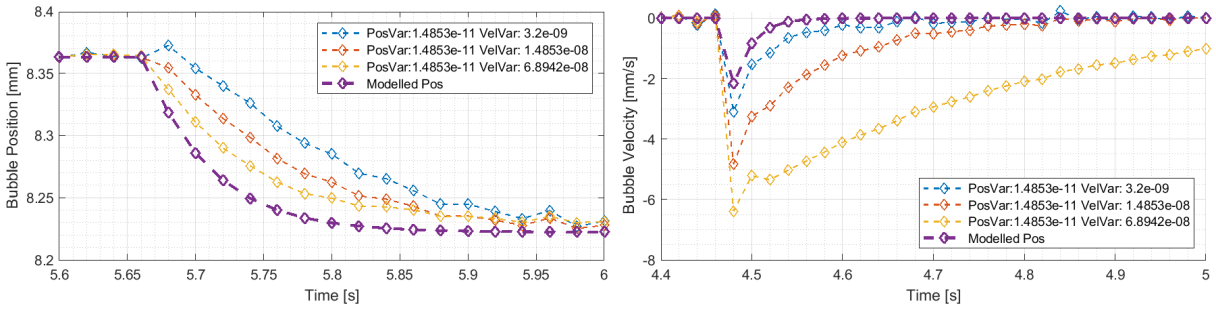

Figure 7.4: This figure shows the position and velocity state estimates generated by the EKF when the covariances are changed. The simulated noise has a variance of 3.2e-12 respectively. The red line represents selecting the covariances to be that which has the same ratio of position to velocity measurement noise covariances as the simulated noise on the measurements. The blue line represents having a higher position variance than the initial and yellow represents having a higher velocity variance.

It can be seen from Figure 7.4 that, while the position and velocity output states of the EKF follow the trajectories of the sampled data from the nonlinear model, there is an apparent tradeoff between the accuracy of the position data and the velocity estimate errors as the covariance values change. This can be seen when comparing the blue lines in the left and the right plots. These both have higher velocity state covariance relative to their position variances, therefore their velocity error is lower. The opposite pattern can be seen for the yellow lines in both figures which are better at estimating the position than velocity.

Due to the cross coupling between position and velocity variances when selecting appropriate measurement variance values, a larger solution space of the velocity and position measurement states variances has been found. This consists of running the EKF outputs for different values of position and velocity variances in the nonlinear model, with noise simulated on the position and velocity data. The metric for quantifying the performance of the EKF is therefore to calculate the error between the output of the EKF and the modelled positions and velocities without noise on the signal. A conglomerate error value is then found by calculating the minimum velocity and positional RMS error for each queried simulated in the solution space. This minimum error is then subtracted from every error value in the solution space and the logarithm of this normalized RMS is calculated across the solution space. These new normalized minimum position and velocity errors are squared and added to each other. This is referred to as the conglomerate error. When the conglomerate error is at a minimum refers to the points where the EKF is able to best estimate the position and velocity values. A surface plot over the queried solution space can be seen in Figure 7.5

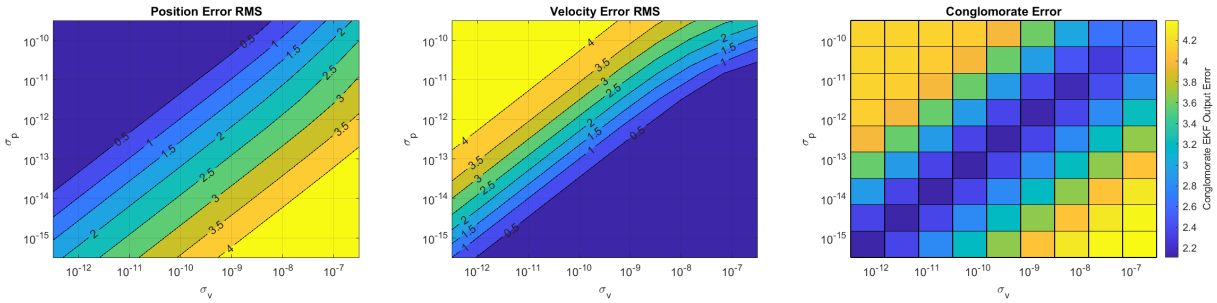

Figure 7.5: This figure shows the RMS error solution space of varying velocity and position variances in the EKF when varying the process variance values of the position and velocity states. The axes of the two plot are held the same with the left plot. There are 12 queried values in the position and velocity variances that the errors have been found in.

It can be seen when comparing the position and velocity solution spaces from the left and middle plots of Figure 7.5 that, by adjusting the measurement noise covariances, either a good position or velocity estimate can be found. When looking at the conglomorate error in the right plot, there is a trough of values where the congolomorate error is minimized. On thing that is interesting when looking at the conglomorate error, is that the minimum error shown in the trajectory has an approximate conglomorate error value of 2. The minimum conglomorate error occours when the ratio between the velocity and position noise is the same as that which is simulated.

The value that has been selected that for the measured noise sigma values are given seen below:

$$\mathbf{N} = \begin{bmatrix} 3.2e-12 & 0 \\ 0 & 3.2e-9 \end{bmatrix} \tag{7.20}$$

7.4.2 Process Noise Variance Estimation

This section demonstrates the design process of finding appropriate values for the process noise state variances. First the disturbance state estimation analysis is shown and then the position and velocity state variance analysis is presented.

Disturbance State Estimation

The process noise for the disturbance state acts as a force affecting the change of the velocity state, therefore the process variance values of the position and velocity states has been initially been set to zero. This is because the individual state estimate diverging from the measurement data is already attributed to the measurement noise. As an initial analysis point, the EKF has been implemented with a disturbance state covariance value, m_d of 1e-15 and the position states of the EKF can be seen plotted alongside the modelled air bubble position as the frequency input is changed in Figure 7.6. It can be noted that, because the nonlinear system equations are implemented directly in the EKF, the only disturbance in the system is due to the discretization of the system equations and interpolation effects in the calculation of the maximum acoustophoretic force.

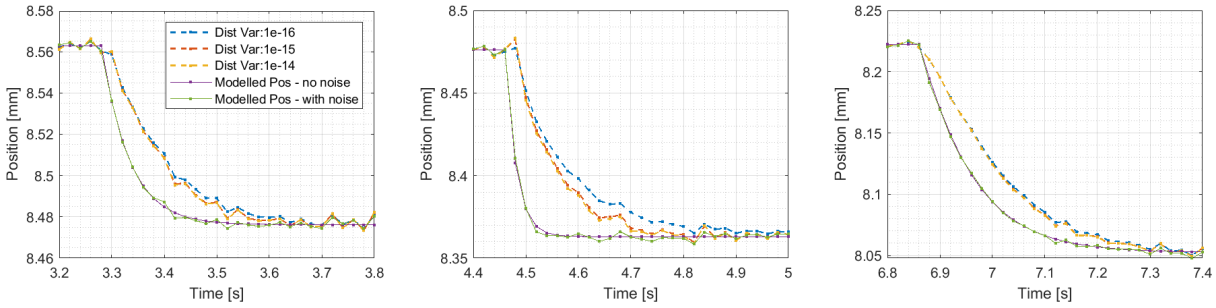

Figure 7.6: This figure shows the position the EKF state outputs over different disturbance state variances as the frequency input is changed..

It is to the surprise of the author that increasing the variance of the disturbance state does not cause the output of the EKF to match that of the simulated measurement state input. It can be seen however, that, as the disturbance state covariance increases , the measured position state begins to take in the characteristic change of the simulated measurement noise on the signals. This can be seen in the middle plot in between 4.6 and 4.7 seconds when comparing the green lines with the yellow and blue lines. The yellow line, representing a higher variance oscillates more with the measured noise than the blue line which has a lower covariance. This is also the case on the not shown velocity state.

It is worth considering that the step nature of the input excites high frequency components of the system dynamics. These high frequency components cannot be properly adapted to for frequencies above the Nyquist Frequency by the EKF without process noise covariance on the measured states. For this reason, the way that the disturbance appears in the position state is due to the EKF first adapting the disturbance state which is then used to calculated the change of the velocity state. The velocity state is then integrated and it is first here that the position is able to be made to follow the measured data. This adaptive EKF delay means that that the EKF disturbance state measurement effectively has a maximum bandwidth which is dependent on the sample rate for the EKF.

Position and Velocity State Variance

Implementing position and velocity state variances can be interpreted as allowing the state's process to deviate from the system model. Because the EKF is calculated at a sample frequency of 0.02, higher frequency dynamics can not be adapted to by the EKF. The inclusion of these state variances allows for an instantaneous dynamic to be present on the air bubble, attributed to process noise, that is not captured by the EKF. Process noise has the property as being a statistical distribution and therefore, can changing instantaneously.

The error solution space of varying the position and velocity state variance has been found in a similar manner as the solution space for varying the velocity and measurement solution spaces in Figure 7.5 on the previous page and can be seen shown in Figure 7.5 with a disturbance state variance of 1e-16. The initial search values selected for the position and velocity variance values are the respective state's measurement noise variances.

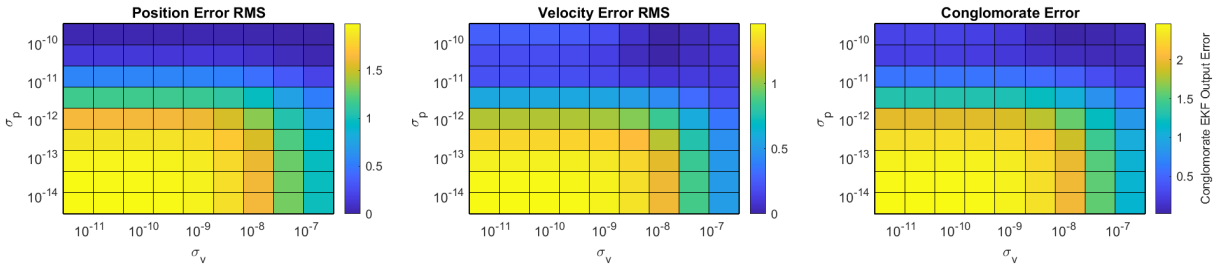

Figure 7.7: This figure shows the solution space for the position and velocity errors of the EKF compared the nonlinear model when varying the process variance values for the position and velocity states. The nonlinear model was modelled with noise on the position and velocity states and the output of the EKF is compared to the modelled air bubble position and velocities without noise. 12 values of position and velocity variance are shown varied.

When looking at the cool spots in the position error RMS in left graph Figure 7.7, it can be seen that the minimum error values lie on the edge of the queried solution space. This suggests that the state variance of the velocity should be further explored beyond the limits shown in Figure 7.7. It can seen in the middle plot, that the position error RMS approaches a minimum in the shown solution space. It can also be seen in the right plot that the minimum conglomorate error is shown to be close to zero. This means that, by increasing the state variances, the tradeoff between position and velocity state accuracy is minimized. It has not been shown, but another iteration of the solution space was solved for and the following values have been selected for the **M** matrix which corresponded to a minimum conglomorate error.

$$\mathbf{M} = \begin{bmatrix} 2.2e-11 & 0 & 0 \\ 0 & 5.4e-9 & 0 \\ 0 & 0 & 1e-16 \end{bmatrix} \tag{7.21}$$

The tuned EKF position and velocity states of the EKF can be seen plotted alongside the input states with and without noise in Figure 7.8.

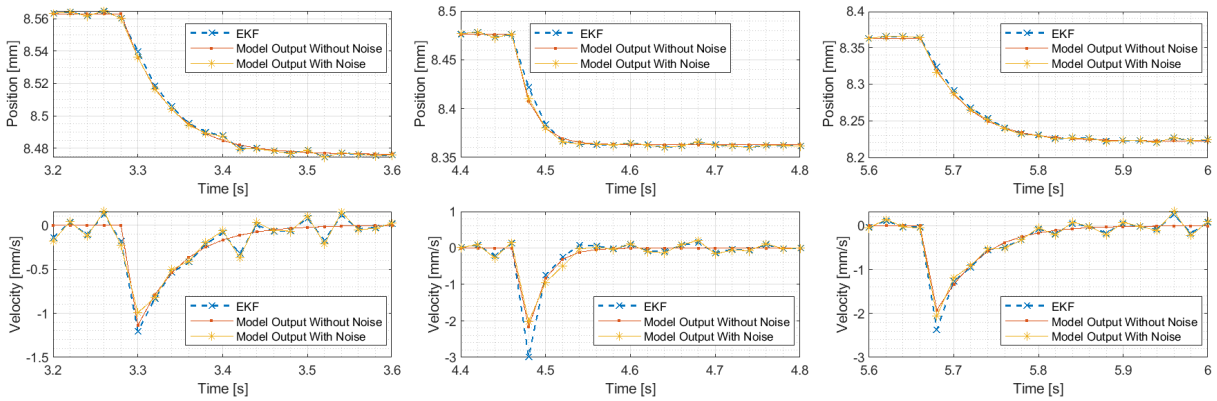

Figure 7.8: This figure shows the position and velocity outputs of the EKF as implemented in the nonlinear model right as the wave frequency is changed. Noise is simulated on the position and velocity measurements and the positions and velocities with and without the noise are shown.

It can be seen in Figure 7.8 that the velocity and position EKF states are are now able to instantaneously follow the measured states. It can be seen that, when comparing the blue and yellow lines in the different plots that the EKF velocity state appears to adapt to the noise on the measured signal. However, the measurement noise appears to be attenuated and the state errors have been shown to be minimized. On top of this, if the variance is made lower than

it is, the EKF cannot fully capture the true higher frequency dynamics of the air bubble. It may be the case that more tuning of the disturbance state covariance may be able to further improve the performance of the EKF but the performance of the EKF is deemed acceptable at the shown iteration.

7.5 EKF on Nonlinear Model Data

In this section, the output of the EKF is analyzed when being implemented in the nonlinear model. This is done by analyzing the forces that the EKF estimates there to be when running the nonlinear model. A simulated disturbance force is then applied to an air bubble in the nonlinear model during the system identification test trajectory and the EKF's ability to detect this disturbance is analyzed..

Considering the EKF Force Estimation

The trustworthiness of the EKF state outputs is determined by its ability to accurately characterise the dynamics of the process it is observing. In this section, this is analyzed by considering the force balance in the system process as simulated by the nonlinear model and comparing it to the force estimates in the EKF.

Every time a measurement is read by the the EKF, the prcoess model in the EKF directly estimates the forces that affect the air bubble that cause the change of the air bubble states.This can be seen in Equation 7.22.

$$\ddot{x}_2 = \frac{1}{m} \cdot \left(-B \cdot x_2 + F_{ap} + F_{dist}\right) \tag{7.22}$$

If the EKF force balance can be shown to be able to replicate the total forces in the nonlinear model, it can be considered to be able to accurately characterize the system dynamics. This can then be taken to say that it can correctly observe the disturbance force amplitude that deviates from this model, such as the streaming effect in the fluid. In order to demonstrate the EKF's capability of doing this, the force values as calculated in the EKF process model and the, the acoustophoretic force and friction force, as simulated in the nonlinear model, are measured and compared. The friction, acoustophoretic, and disturbance force terms, have been plotted in Figure B.4.

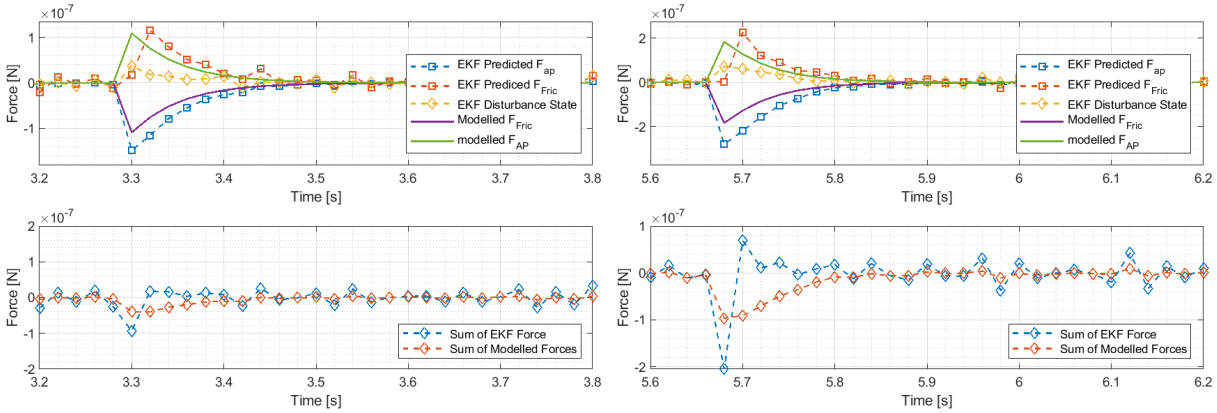

Figure 7.9: In the top plot of this figure, the force balance as output by the nonlinear model and the forces, as calculted in the EKF process model right as the input frequency is changed in a frequency step. The bottom plots show, the "Sum of EKF Forces" refers to the sum of the disturbance force state, the process modelled acoustophoretic force, and the friction force present in the EKF model. The "Sum of Modelled Forces" refers to the sum of the acoustophroretic force and friction force that are present on the modelled air bubble.

When looking at the forces in the top two plots of Figure 7.9, a number of observations can be made. The first is that the predicted acoustophoretic force, as seen by comparing the purple and blue lines, appears to be overestimated by the EKF, however its decaying characteristic appears to be similiar to what the modelled acoustophoretic force is. The second thing that can be observed is that the EKF friction force appears to have a timestep delay as can be seen by comparing the green and red lines. This occurs due to the low sampling time of the EKF, causing there to be a delay. When looking at the disturbance force, as represented by the yellow line, it appears to be good at counteracting the overestimation of the acoustophoretic force amplitude and compensating for the underestimation of the friction force amplitude.

When looking at the sum of forces in the bottom plots of Figure 7.9, it can be seen that, when input is first changed, the EKF appears to overestimate the total forces present on the air bubble. After this overestimation, for the next couple of timesteps after the change of input, the EKF underestimated the total the force on the air bubble. This is due to the adaptive nature of the EKF causing the disturbance force to try to compensate for the incorrectly estimated total force on the air bubble on the first timestep. It is also the case that the EKF has a, not shown, Kalman gain $\mathbf{K}$ and process model $\mathbf{P}$ matrix that is adapting to the measured states in the system. These adapting matrices attempt to cause the estimation state error to converge. The low sampling frequency means that a satisfactory rpresentation of the air bubble force balance in the EKF, right as the input is changed, difficult to achieve.

When considering the sum of forces in the EKF and modelled forces in the bottom plots of Figure 7.9, it can also be seen that the noise on the measured states cause there to be a stochastic variance on the sum of modelled force in the EKF. This can be seen in the bottom right plot between 5.8 and 6.2 seconds. It can also be considered that the mass of the air bubble is small relative to the forces acting on it and therefore high frequency components of the system dynamics necessarily will affect the air bubble to a high degree. In this manner, it is difficult to decouple the noise on the air bubble from the true system dynamics

It is, however, clear from the data in the bottom plot when the input to the system, and, therefore, the total forces acting on the bubble, is changed. It is therefore assumed that a lower frequency input dynamic would also be detectable as a function of the sum of EKF forces. Overall, this analysis demonstrates that the EKF is capable of characterizing the air bubble dynamics in the nonlinear model to a fair degree.

Ability to Observe Disturbance Force

In this section, the ability for the EKF to correctly characterise a step disturbance acting on the air bubble is shown. To demonstrate this, a disturbance step of 2e-7 N has been simulated as affecting the air bubble between 2.2 and 3 seconds and can be seen shown in Figure 7.10.

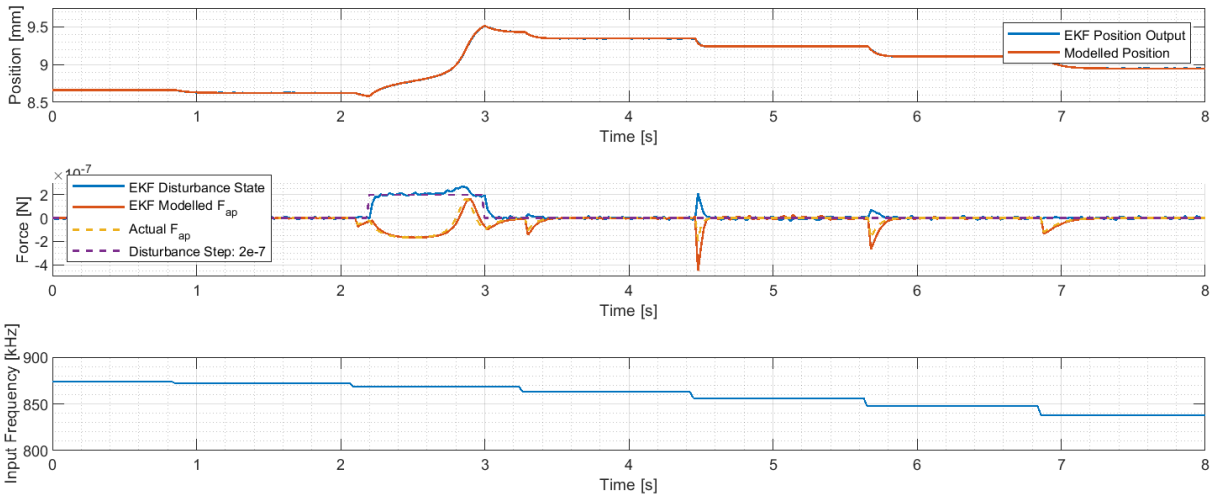

Figure 7.10: This figure shows the response of the EKF to a force step of 20e-7 N that occours between the times of 2.2 and 3 seconds. The "EKF Modelled F_{ap}" refers to the acoustophoretic force estimate from the EKF process model in the middle plot. The "Actual F_{ap}" refers to the modelled acoustophoretic force acting on the air bubble.

It can be seen that in Figure 7.10 that the EKF is able to both determine the amplitude and duration of the disturbance force affecting the bubble. It can be seen that the EKF is also capable of maintaining a good estimate for the acoustophoretic force when the air bubble moves to a different acoustic node. This can be seen in the top plot by the bubble position moving one wavelength away from its original node between 2 and three seconds. It can however, be seen as the air bubble settles at the new node at 2.8 seconds the disturbance force appears to have a small positive dip. This is due to the high frequency dynamic present on the acoustophoretic force as it quickly changes value. This dip is also shown to quickly disappear. Overall, the EKf is able to demonstrate the ability to characterise a disturbance force affecting the air bubble on the nonlinear model.

7.6 EKF on Experimental Data

In this section, the results of applying the EKF is shown on experimental data. This is first shown on the system identification dataset. The EKF is then applied to a control trajectory test set shown in Section 8.5 on page 77.

7.6.1 EKF on System Identification Test Set

The results of applying the EKF to an experimental test data set can be seen shown in Figure 7.11. The position and input frequency data has also been used to simulate the acoustophoretic force that would be experienced in the nonlinear acoustophoretic force model and this can be seen in the yellow line in Figure 7.11. The maximum acoustophoretic force for the given input frequencies has also been found and the maximum and minimum force an air bubble could experience before moving to a different node is shown as the dotted lines in Figure 7.11.

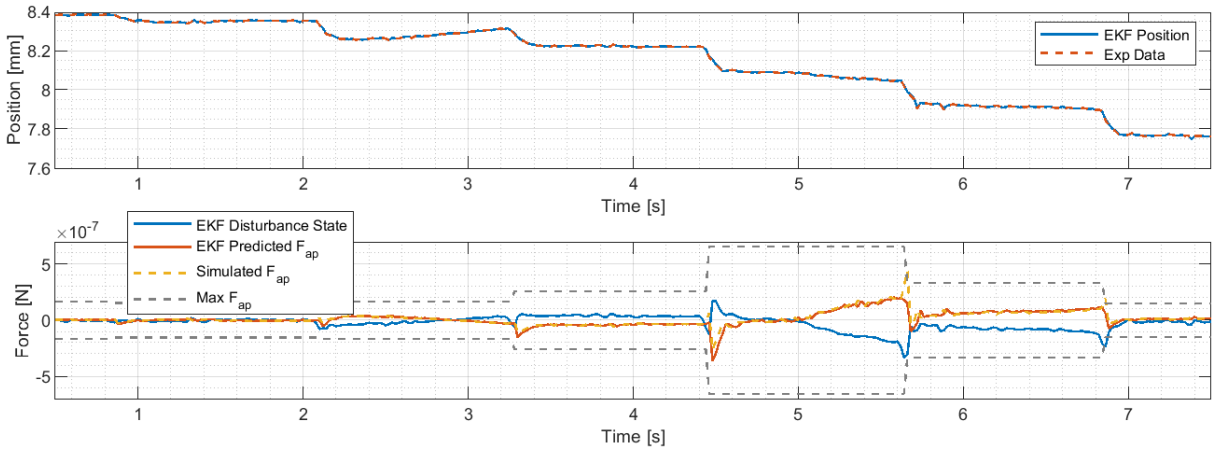

Figure 7.11: This figure shows the output of the EKF when being applied to the experimental system identification dataset. The frequency input is the same as what is shown in Figure 7.10. In the bottom plot, the "EKF Predicted F_{AP}" is the acoustophoretic force generated by the EKF process model. The "Simulated F_{AP}" is acquired by finding the force that the nonlinear acoustophoretic force expression would give for the air bubble position. "Max F_{ap}" refers to the calculated k_{max} for the input frequency.

The first thing that can be noted by the disturbance state of the EKF, as denoted by the blue line in the bottom plot in Figure 7.11, is that the disturbance state remains close to zero over the full dataset. This suggests that the air bubble remains close to the modelled node position over the full test dataset. It can also be seen, by looking at the blue line in the bottom plot that, while there are small disturbance force peaks when in the input is changed. It can also be seen that the highest disturbance force occurs when the maximum acoustophoretic force is highest. While this may be a true representation of the disturbance force on the bubble, it may also be the case that the maximum acoustophoretic force is estimated incorrectly. It can be understood that the maximum movement a bubble will experience from an acoustophoretic node would likely occur when the maximum acoustophoretic force is lowest. This aligns well with the fact that the air bubble has a large relative movement between 2 and 3 seconds when the acoustophoretic force is low. However, there is also a relatively high amount of movement between 4.5 and 5.5 seconds when the acoustophoretic force should be highest and it is therefore difficult to say conclusively how trustworthy the amplitude of the disturbance estimate is.

When looking at the acoustophoretic force in Figure 7.11 between 2.2 and 6.8 seconds, the acoustophoretic force slowly goes from being negative at 2.2 seconds, to positive at 3.2 seconds, and back to negative from 5 seconds to 6.8 seconds. This flowing characteristic of the disturbance aligns well with the interpretation of the acoustic disturbance force as a slowly changing random walk force. Skepticism must, however, be held when attempting to interpret the amplitude of the disturbance force, because a small change of the speed of sound in the fluid could or a different reflective damping coefficient could quickly lead to the modelled acoustophoretic force amplitude being very different from what is modelled.

Overall, the step-like nature of the input allows for observing the flowing nature of the fluid streaming effect. However, the step like nature of the input does not allow for discerning the reliability of the EKF over a larger range of air bubble positions, nor does it allow for seeing how the motion of the air bubble changes to a continuously changing input frequency.

7.6.2 Characterizing the Linearly Controled Bubble Response

In this section, control response data is analyzed to demonstrate the EKF's ability to illuminate parametric modelling uncertainty in the presented acoustophoretic force expression. For the

control response shown in Section 8.5 on page 77, the frequency input is a function of the reference position which changes slowly over the dataset. The input dataset for the test data shown in the previous section consists of a series of discontinuous steps between input values. The air bubble position, velocity, and input frequency, is taken from the control trajectory and is considered as just an input dataset for the EKF in this section. In this manner, the air bubble reference and control error are disregarded and not considered.

The calculation of the disturbance force is dependent on the fact that the acoustic node location is predicted correctly. The node position calculation in the EKf is shown plotted alongside the measured air bubble position over the control trajectory in Figure 7.12. For reader clarity, the acoustophoretic force expression present is repeated below.

$$F_{ap} = k_{max} \cdot sin(2 \cdot \lambda(x_{node} - x_{node.init}) - (x_p - x_{p.init})) \tag{7.23}$$

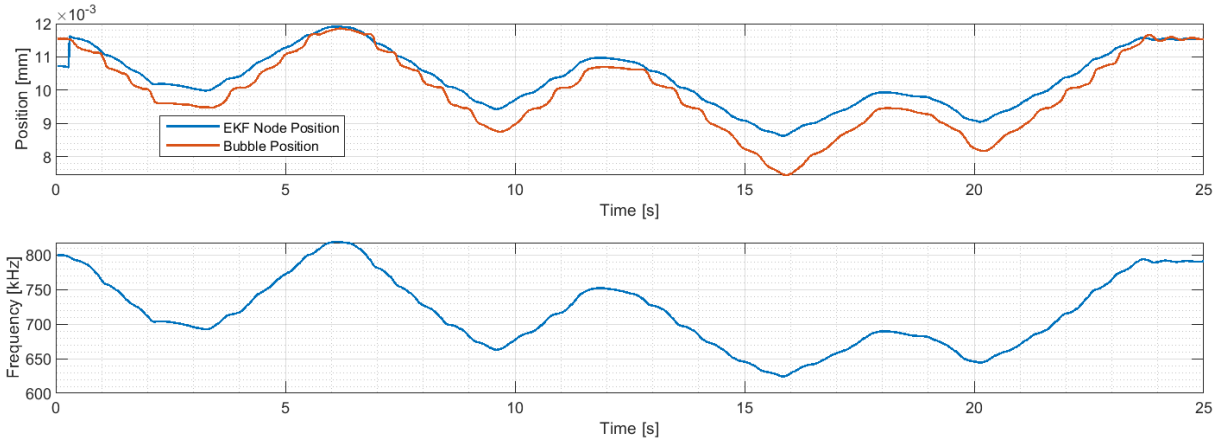

Figure 7.12: This figure shows the EKF's estimated node movement. The initial node position is taken to be the position of the node at 25 seconds. The minimum and maximum wavelength is 1.2 and .9 mm occurring at frequencies of 800e and 700 kHz respectively

It can be noted that the node position is controlled by a PI controller which functionally places the acoustic node closer to the reference location than the bubble. For this reason, it is not expected that the air bubbble position and node position should lie on top of eachother. The node position should instead oscilate between being at a higher position than the air bubble when the bubble has a positive velocity and a lower position when there is a negative velocity present. It can be seen that this is not the case in the dataset, as the node does not travel the same distance that the air bubble travels. It can be seen that, as the air bubble is moved further away from the initial position, the EKF node position appears to underestimate the change of the node position. Because the EKf has no mechanism for adapting to modelling uncertainties due to incorrect estimation of the node location, the disturbance force cannot give a meaning estimation for the streaming force on the bubble.

The input can be seen to change continuously between input values in the bottom plot of Figure 7.12. When a continuous input is used for the EKF, the relatively large instantaneous change that were found in disturbance state due to modelling discretization should be less prevalent. This is due to the fact that the node position is changed slowly, so the acoustophoretic force will change slower, and therefore, have lower amplitude high frequency components. This suggests that the maximum change of acoustophoretic force between time steps should be smaller, and the EKF should be better at maintaining state estimate continuity.

Consideration of the Force Balance

The EKF has shown the ability to maintain force balance continuity fairly well in the nonlinear model. This section analyzes the force balance as given by the EKF as the node settles at the end of the dataset. The fact that the force continuity is maintained by the EKF means that F_{dist} is solved for such that the change of the velocity corresponds to the forces present in the system. The equation of motion for the air bubble as implemented in the EKF is repeated here:

$$\ddot{x}_p = \sum F = -b \cdot \dot{x}_p + F_{ap} + F_{dist} \tag{7.24}$$

The force balance over the last couple seconds of the control trajectory, as calculated by the EKF, is shown in Figure 7.13. The last seconds of the control dataset is selected because the node position offset is taken to be at the settled node location, and therefore, the results of the EKF node estimate going from poor to good are shown.

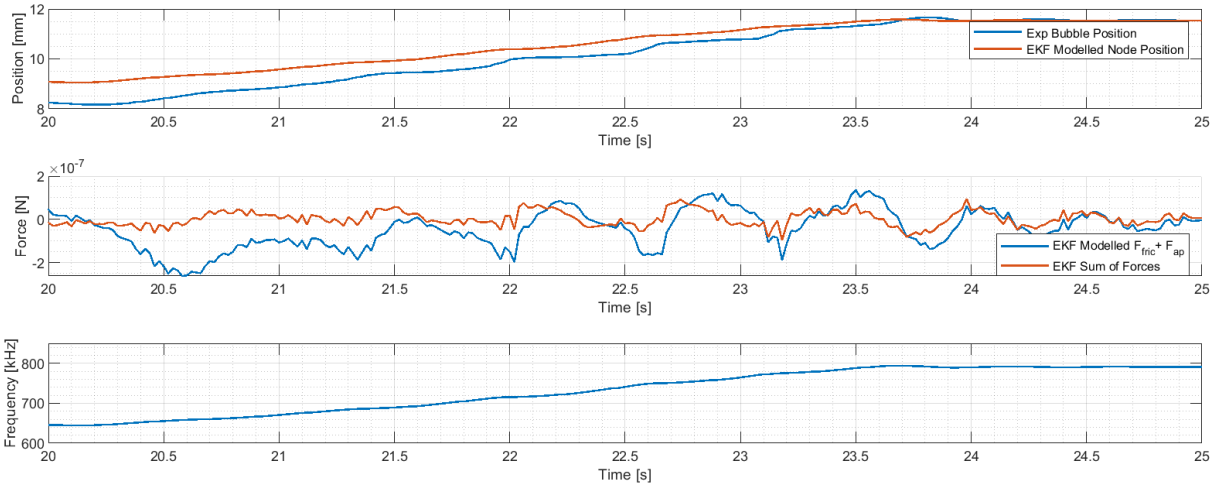

Figure 7.13: This figure shows the last seconds of the control trajectory. The "EKF sum of forces" in the middle plot refers to the disturbance state plus the acoustophoretic force expression plus the friction as calculated by the EKF process mode.

It can be seen in Figure 7.13 that the disturbance force returns to zero at the end of the dataset. This is due to node position appearing to correlate well the experimental bubble location. However, it can be seen in the middle plot, when looking at the the sum of forces and estimated forces without the disturbance force, the modelled force appears to be mostly cancelled out by the disturbance force. This is not what is expected, as, if the forces affecting the air bubble was properly estimated by the EKF, the disturbance should have minimal influence on the sum of forces.

The summation of the forces of the forces modelled by the EKF does, however give an idea of the total experimental forces present on the air bubble. When considering what constitutes the acoustophoretic force expression, there is both the node position and the amplitude of the attractive domain force. If the EKF process model is correct, the characteristics of the EKF sum of forces should align with the sum of the acoustophoretic force and friction the air bubble experiences as describe the by EKF process model. This can be seen to begin to be the case as from 22 seconds to 25 seconds. This is assumed to be the case because the node estimation becomes much closer to the "true" node location. It must, however, be held in mind, that the EKF was shown to not give a completely accurate estimate for the sum of forces on the air bubble when a step input was used. For this reason, further analysis is required to discern

how well the modelled sum of forces by the EKF can be considered representative of the true sum of forces present on an air bubble.

7.7 Improving Model Parameters With EKF

It is stated as a goal in the start of this chapter, that the system identification methods presented should be able to provide the ability to improve the system model. This section discusses methods in which the EKF can achieve this aim. This is done by first comparing the sum of forces that the EKF provides when applied to the previously shown control data. A discussion of how the nonlinear model can be used, along with the output of the EKF on experimental data, to tune the modelling parameters..

EKF Force Balance Compared to Maximum Acoustophoretic Force

In the control data trajectory, it was shown that the steady state error in the node position estimation limited the EKF's ability to characterise the acoustic streaming force affecting the air bubble. The other parameter of the acoustophoretic force, the maximum acoustophoretic force, is independent of the air bubble position and only a function of the input frequency. Because the input frequency is varied between 800 and 610 kHz over the control data input and the fact that acoustic resonance occurs with approximately 32 kHz intervals, the amplitude of the acoustophoretic force is expected to experience multiple maximums and minimums over the control input dataset as the velocity of the air bubble is high. Because the frequency is changed in a manner reminiscent to a ramp function in the control data, it can be expected that, as the input causes the acoustic field to go in and out of acoustic resonance, the sum of forces should oscillate in a similar manner. This is because the force acting on an air bubble goes from minimums to maximums as a function of this resonance. To demonstrate this being the case, the absolute sum of forces present in the EKF process model, has been shown plotted alongside the modelled maximum acoustophoretic force as it is changes due to the input and can be seen in Figure 7.14 on the facing page

It can be seen when looking at between 7 and 9 seconds in the top plot of Figure 7.14 that the maximum sum of force present on the air bubble ocurs the input frequency is changing. The fact that force peaks are present supports the peaky nature of the acoustophoretic force model. On top of this, the sum of forces have peak values that appear at a similar frequency in which the simulated maximum acoustophoretic force occurs. As a whole, the peaks from the sum of EKF forces appear to line up with the maximum acoustophoretic force.

There are also a number of points where the peak force experienced by the air bubble does not precisely align with the modelled maximum acoustophoretic force. This can be seen to be the case at approximately 7 seconds where the maximum sum of forces peaks after the modelled force peaks. This may, however, be due to the adaptive nature of the sum of forces presented by the EKF. The sum of forces adapts to conform to the measurement data and this could likely cause a delay on where the maximum force peak occurs. This is reinforced by the fact that the resonance occurring at this time is only present for a very short amount of time as seen in the yellow lines.

The analysis of the sum of forces affecting the air bubble is made difficult due to the fluid streaming force affecting the air bubble. The presence of this force could make the air bubble be pushed away from the acoustic nodes at any time over the dataset. This means that there is an expected variance on the peak locations when looking at specific given force peak.

Overall, the sum of force peaks appear to align well with the modelled acoustophoretic force peaks and it is difficult to decouple the adaptive nature from the EKF disturbance state

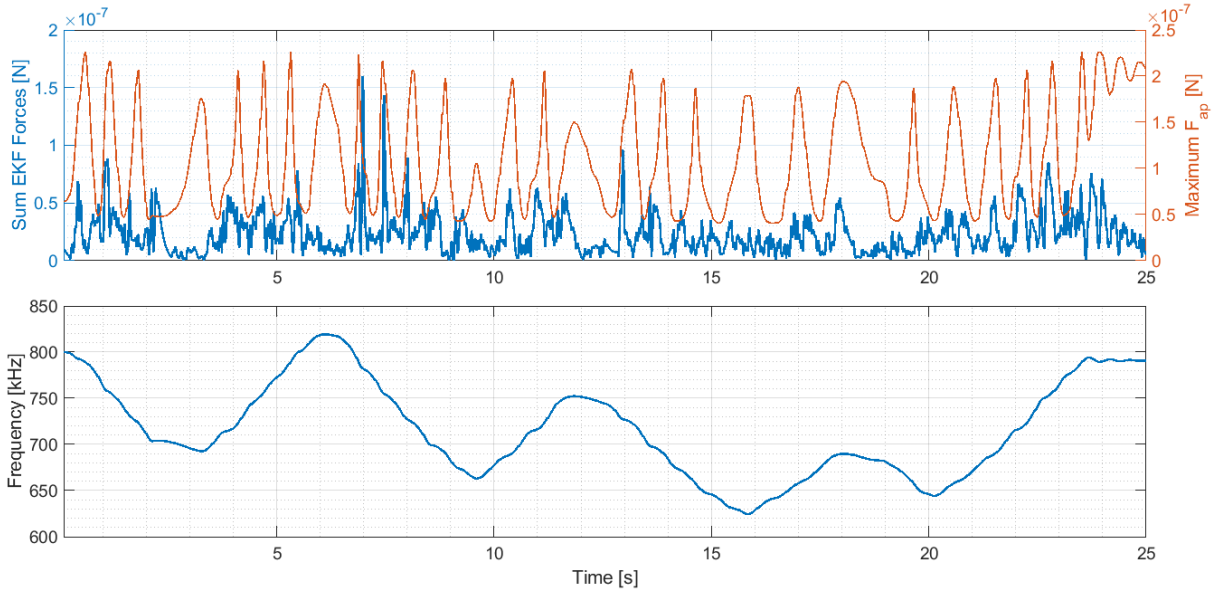

Figure 7.14: This figure shows the sum of forces generated by the EKF when using the experimental control dataset compared to the maximum acoustophoretic force that is generated by the acoustophoretic force expression for the given frequency. The sum of force in the left axis of the top plot refers to the summation of the acoustophoretic force, the friction force, and the disturbance state force as is calculated in the process model.

measurement from the "true" force maximums and minimums affecting the bubble..

Comparing Modelled Data to Experimental Control Data

It has been shown that it is difficult to make qualitative arguments about the nature of the force experienced by an air bubble from the sum of forces by the EKF from experimental data alone. However, the fact that the maximum force, as calculated by the EKF, experienced by the air bubble aligns relatively well with the maximum acoustophoretic force suggests that further analysis of the control data may be able to provide additional information about the acoustophoretic force affecting the air bubble. In this section, the control input frequency data and initial air bubble position are used as inputs in the nonlinear model. The results of using the EKF on the modelled air bubble is then compared to the results of the EKF on the experimental bubble location. This is used to show where the modeling uncertainties are. The nonlinear model response to the control frequency input and initial position can be seen plotted alongside the measured control data in Figure 7.15.

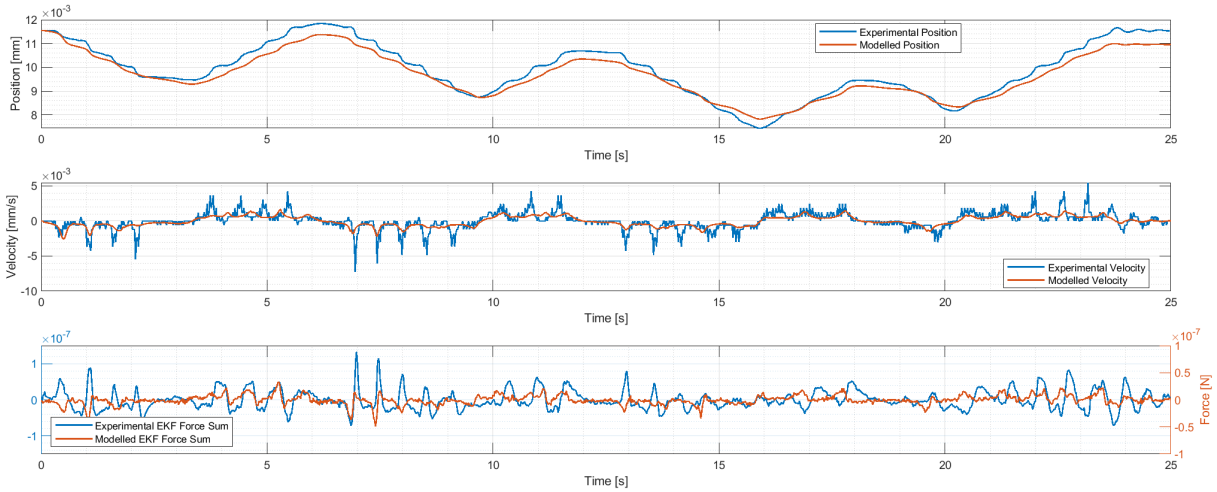

Figure 7.15: The control input frequency dataset is used as the input for the nonlinear model and has been plotted along the experimentally found bubble movement. In the bottom plot, there are two different axis for the blue and orange lines, respectively, and this allow for easier comparison of their waveform characteristics.

It can be seen in the top plot of Figure 7.15 that the node movement of the modelled air bubble does not exactly capture the experimental air bubble movement change. This suggests that the modelled speed of sound in the liquid is likely higher than that of the experimental fluid. A higher speed of sound would cause the acoustic wavelength in the fluid to be shorter and, therefore there will be less node movement.

Another modelling uncertainty that can be seen when looking at the middle plot in Figure 7.15 is that the modelled velocity underestimates estimates the experimental velocity. This can be seen to be the case over the whole dataset. This could be caused by a number of factors. One reason could be due to the friction expression for air bubbles not being representative of the single constant damping coefficient used. In the air bubble modelling chapter, it was also suggested that the air bubble recognition algorithm may greatly overestimate the air bubble radius due to the low resolution of the camera used. This would also mean that the air bubble actually has a lower radius than what is modelled. This would lower the frictional coefficient experienced by the bubble relative to the acoustophoretic force and could cause the velocity to peak in a manner more reminiscent of the measured data.

The input frequencies to the nonlinear and experimental model is the same and, for this reason, the times at which the air bubble velocity changes the most, and, therefore, where the air bubble experiences the highest acoustophoretic force are expected to line up with eachother. It can be seen that this is not entirely the case when looking at the velocity and sum of forces output by the EKF in the last 10 seconds of the control trajectory. This can be seen plotted more clearly in Figure 7.16

Because the frequency input and sampled measurements fed to the EKF in the nonlinear model are sampled at the same sample frequency as the experimental data, the influence of the delay effect from the EKF adapting to the data can be expected to be the same. For this reason, if the nonlinear model and the experimental are both excited primarily by the acoustic force, the times at which the sum of forces are highest should be the same. When comparing the experimental and modelled EKF force sums in the bottom plot of Figure 7.16, it can be seen that the frequency of the maximum sum of forces occurs appears to be different form each other. This can be seen between the times of 20 seconds and 25 seconds in the bottom plot where the experimental force peaks at a higher frequency than the modelled. This likely occurs due to the previously noted incorrect estimate for speed of sound in the fluid. This speed of sound determines at what frequencies the acoustic resonance occurs in the fluid. The

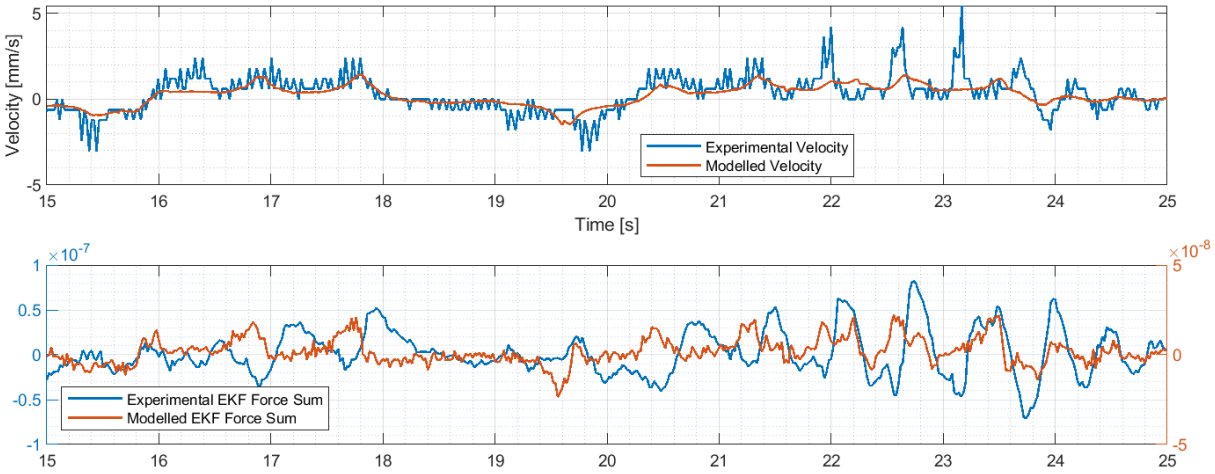

Figure 7.16: This figure shows the last 10 seconds of the velocity and sum of forces data shown in Figure 7.15

results shown in the figure further reinforces the fact that the speed of sound is estimated to be higher than what the experimental fluid's speed of sound is, because a lower speed of sound in the fluid would mean that the frequency interval between acoustic resonance occurring in the fluid would be greater. This would lead to the acoustic force peaks occurring at a lower frequency than what is used in the nonlinear model, similar to what is shown in the experimental data.

7.7.1 Model Improvement Discussion

The qualitative differences between the modelled and experimental air bubble velocity change and sum of force characteristics shown in Figure 7.16 are admittedly quite minimal. This, added to the fact that the noise is present on the signals, suggests that the used acoustophoretic force expression is a good estimation for the true experimentally occurring acoustophoretic force. To conclusively improve the air bubble model, a different dataset would be beneficial. Using a simple input frequency ramping input would likely allow for more clear differences in the trends between the modelled and experimental change of velocity characteristics. If this was the case, the limitation of the EKF sample frequency would not play as large of a role when interpreting the force balance of the EKF process model.

The generated sum of forces by the EKF can be considered as producing an expression that has the same qualitative characteristics as the true forces affecting the air bubble. Skepticism must be held when comparing the amplitude between the experimental and modelled sum of forces as there is likely an experimental streaming force, that is hard to decouple from the shown force. The sum of forces amplitude is also hard to use as a metric as there are multiple factors that cause a force difference between the experimental and control data and it is easy to misattribute amplitude differences to the wrong modelling parameters. With that said, comparing the characteristics between the modelled force and experimental force generate by the EKF has demonstrated the ability to be used as a metric for improving modelling parameters.

One potential improvement for the EKF would be to add a node movement offset state. This would potentially allow for the EKF to able to characterise the streaming force on the air bubble over a larger position range. This was not included in the presented EKF as the tuning of this extra state must be performed with caution, as it would be very easy for the streaming force affecting the bubble to be attributed to the change of this state. The fact that there exists a mapping between the true node position and the input frequency would need to be taken

into account and this would likely require a different type of Kalman Filter.

7.8 Chapter Conclusions

This chapter has shown that the presented Extended Kalman Filter has demonstrated the ability to characterise the acoustic streaming force on an air bubble when the air bubble remains close to its initial position. It has also demonstrated the ability to potentially be used as a tool for improving the parameter estimation in the air bubble model. The fact that the node position of the modelled air bubble was not the same as the experimental air bubble movement in the control dataset was a conclusively limiting factor in the ability for the EKF to be used to characterise the streaming force affecting the air bubble over as the air bubble moved far away from its initial position. When interpreting the output of the EKF, the frequency components of the system dynamics present on the air bubble must also be taken into account. Overall, the EKF has demonstrated promise as a tool that can be used when analyzing the position and velocity data of air bubbles experiencing the acoustophoretic force.

Chapter 8

Air Bubble Linear Control Design

Chapter Abstract

This chapter presents the control scope and a linear control structure proposal to actuate air bubbles. This consists of defining the control requirement and presents a system reference trajectory with a maximum reference position change of 1 mm/s and zero steady state error. The acoustophoretic force is then and the dynamics of air bubbles is shown to be a static gain at low frequencies and has a second order damping characteristic close to the Nyquist frequency set by the camera frame rate. Two PI controllers are then designed. The first was shown to be tuned too aggressively and the disturbance present due to the difference between the nonlinear model and the linearized model caused instability. A second controller was then designed with a lower proportional gain that was shown to work experimentally and in the nonlinear model over a large range of air bubble radii. The second controller demonstrated good disturbance rejection and had satisfactory performance for the designed requirements.

8.1 Introduction

In this chapter, the acoustophoretic force is linearized and the linearized dynamics for air bubbles experiencing the acoustophoretic force are analyzed. This analysis is used to design a linear control strategy that can actuate the air bubbles along a predefined reference both in the nonlinear model for and experimentally. This chapter consists of the following sections:

- Section 8.2 : Control Objectives and Scope
- Section 8.4 PI Controller for Individual Particle
- Section 8.5 : Updated PI Controller

8.2 Control Objectives and scope

Control Scope

Air bubbles larger than 200 μm will not be considered when designing the control structure. This is because their bouyancy force in olive oil makes it so that it is deemed impracticable to cause it to actuate to a position before it floats beyond the range of the camera.

It has also been decided that particles smaller than 50 mm will not attempted to be controlled. This is because the radius of these particles are less than 5 pixels and the image recognition algorithm used by this thesis cannot reliably recognise objects of this size. On top

of this, in olive oil, these particles float very slowly in the fluid and are therefore, limited in the number of solid particles they can quickly be actuated toward.

In order to simplify the control design process, the amplitude of the voltage supplied to the transducer is held constant. While the Bentowave transducer does has a frequency dependent pressure output wave amplitude gain, what this output gain actually is taken appearing in the form of a disturbance.

The input frequency has also been given a saturation limit of 400 kHz to 1200 kHz. When the controller is initialized, an initial frequency of 800 kHz is assigned to the transducer. This has been implemented because the datasheet for the Bentowave shows that its output pressure wave amplitude is greatest in this range.[2]

Design Objectives

In designing the control structure for the air bubbles, the interest of this thesis is to achieve multiple aims. These will be presented and explained in terms of priority below.

Design Objective 1: Dynamic Performance : 1 mm per second

The first control objective is the dynamic performance of the air bubble actuation. The reason for this requirement is that the air bubbles that will be actuated experience a buoyancy force. The purpose of the designed control structure is to cause a bubble to reach a plastic particle before the bouyancy causes the bubble to float past the plastic. A value of 1 mm per second has been selected due to it being lower than the approximate maximum speed that was seen when changing the input frequency when designing the Extended Kalman Filter in Chapter 7. This has been shown to be a sufficient requirement to achieve bubble/plastic collision.

Design Objective 2: Zero Steady State Error

Zero steady state error is a requirement because the control goal is to cause air bubbles to interact with solid particles in the fluid. For this reason, it is required that air bubbles must be made reach the reference location with zero steady state error to ensure contact.

Design Objective 3: Capable of Rejecting Streaming Disturbances

Bubbles are added to the olive oil by manually shooting a syringe filled with air into the cabin. The bubbles are added with a high force because it is the impact of the air with the bottom of the cabin that causes the volume of air to break apart chaotically and spreading small bubbles throughout the cabin. When this occurs, a chaotic turbulent flow is present in the cabin. This turbulent flow of the fluid imparts a force on the bubbles and plastic particles in the fluid. This acts as a disturbance on the particle that the control strategy must be able to reject. It is also recognised that the 1D field wave approximation used in this thesis is only an approximation of the actual pressure field in the cabin and therefore, modelling uncertainties exist will appear as disturbances must be rejected.

Control Reference Trajectory

A reference control trajectory has been selected that controllers designed in this section are tested on. This trajectory can be seen in Figure 8.1.

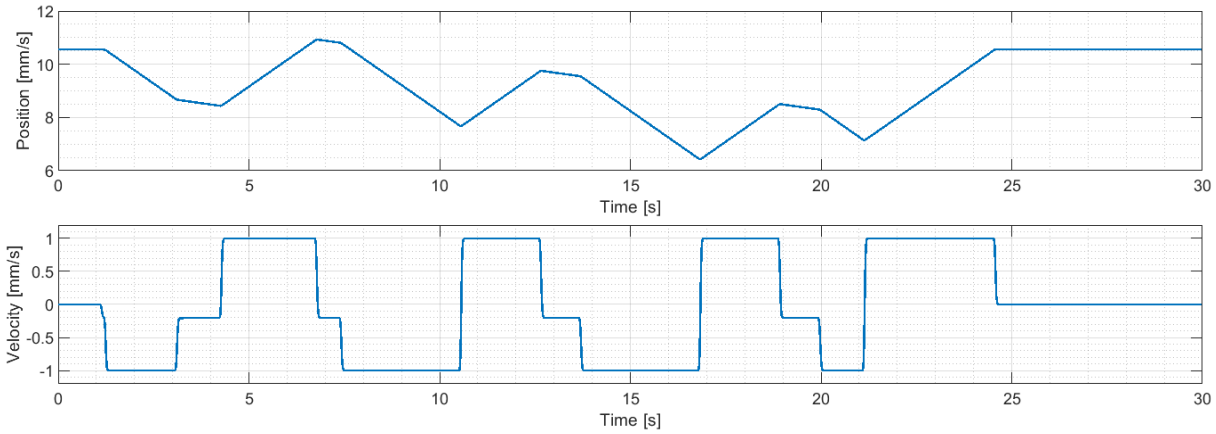

Figure 8.1: This figure shows the control reference trajectory the controllers will be tested on.

The selected trajectory shown in Figure 8.1 consists of moving the bubble up and down with a max slew rate of 1 mm/s. When the controller is initialized, the initial bubble position is added to the control trajectory. The maximum movement that the controller makes the bubble move is 4.5 mm. This trajectory requires a large input frequency range, making sure that the controller will be able to make bubbles move to many of the plastic particles in the recorded image frame.

8.3 Linearization of Air Bubble Model

In this section, physical intuition, along with a first order Taylor Approximation is used to generate a linear parametric model for air bubbles. This model is used for the design of the linear controllers presented in this chapter.

The force acting on an air bubble has been shown to be a attraction towards the nearest node of the quasi standing waves. For this reason, if the pressure wave that is being transmitted from the transducer is held constant, the x axis motion of the particle, x_p, can be approximated as a mass damper system with a nonlinear spring component and an unknown streaming force:

$$m \cdot \ddot{x} = b_{visc} \cdot \dot{x} + F_{streaming} + F_{ap}(f, x) \tag{8.1}$$

Where the acoustophoretic force can be expressed as Equation 8.2, with $k_{amp}(f)$ being the mapping of the amplitude of the acoustophoretic force to a given frequency:

$$F_{ap} = k_{amp}(f) \cdot sin(2 \cdot \lambda \cdot (x_{node} - x_p)) \tag{8.2}$$

When the frequency is held to be constant, the node position, x_{node} can be seen to be mapped to a set of locations that exist a half wavelength of the acoustic pressure wave from eachother. That is to say that there are multiple node positions in the fluid that are all constant for a given frequency. It has also been shown in Section 5.3.3 on page 28 that the settling time of the pressure wave is approximately 2 orders of magnitude faster than the refresh rate of the camera used. This means that when the frequency is changed, the node location can be considered to change instantaneously from the perspective of the controller.

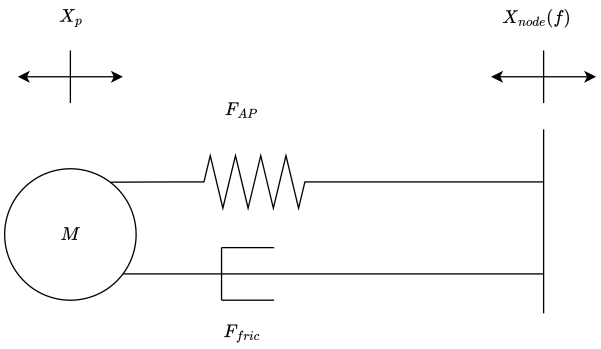

Figure 8.2: This figure shows a mass damper system made to be representative of the forces acting on a air bubble when acoustophoretic forces are present.

For a small change of frequency where the node movement, incited by $k_{node}(\Delta f)$, is small, there can be assumed to be a linear mapping between between the node position and frequency. This was shown during the analysis of the acoustophoretic force characteristics in Figure 5.8 on page 33. In this way, the node position from Equation 8.2 can be linearized to the following:

$$F_{AP} = k_{amp}(f) \cdot sin(2 \cdot \lambda \left((x_{node,f0} + k_{node.\Delta f} \cdot \Delta f) - (x_{p0} + \Delta x_p) \right)) \tag{8.3}$$

If the air bubble has settled and the streaming effects are small when the system is initialized, the initial node position and bubble location can be assumed to lie on top of eachother and these terms can be disregarded. The acoustophoretic force can thereafter be expressed as the following:

$$F_{AP,\Delta} = k_{amp}(f) \cdot sin(2 \cdot \lambda (k_{node.\Delta f} \cdot \Delta f - \Delta x_p) \tag{8.4}$$

This function is linearly approximated using a first order Taylor Approximation as Equation 8.5. This approximation requires the assumption that the particle will always be close to a node or else the sin(x) = x approximation does not hold. This approximation also assumes that the acoustophoretic force is constant over the frequency range used. This will be discussed shortly.

$$F_{AP,\Delta} = k_{amp.f_0} \cdot 2 \cdot \lambda \cdot k_{node.\Delta f} \cdot \Delta f - k_{amp.f_0} \cdot 2 \cdot \lambda \Delta x_p \tag{8.5}$$

Replacing the coefficients multiplied by Δf and Δx in Equation 8.5 with k_f and k_{xp} respectively, where k_f is the change of node position due to frequency and k_{xp} is the linearized amplitude of the acoustophoretic force, allows for expressing the acoustophoretic force in change variable form. The change variable expression for the equation of motion for a particle is expressed by placing Equation 8.5 into Equation 8.1 with the new coefficients:

$$m \cdot \Delta \ddot{x}_p = -b \cdot \Delta \dot{x}_p - k_{xp} \cdot \Delta x_p + k_f \cdot k_{xp} \cdot \Delta f + F_{streaming} \tag{8.6}$$

This expression can now be rewritten in the Laplace domain:

$$\Delta x_p(s) = \frac{-k_f \cdot k_x}{m \cdot s^2 + b \cdot s - k_x} \cdot \Delta f(s) + \frac{1}{m \cdot s^2 + b \cdot s - k_x} \cdot F_{streaming}(s) \tag{8.7}$$

The state space formulation of the linearized system equations are shown below, with the exclusion of the disturbance state, $F_{streaming}$:

$$\dot{\mathbf{x}} = \mathbf{A} \cdot \mathbf{x} + \mathbf{B} \cdot F_{rad}, \quad y = \mathbf{C} \cdot x \tag{8.8}$$

Where

$$\mathbf{A} = \begin{bmatrix} 0 & 1 \\ -\frac{k_{xp}}{M} & -\frac{B}{M} \end{bmatrix}, \quad \mathbf{B} = \begin{bmatrix} 0 \\ \frac{k_f \cdot k_{xp}}{M} \end{bmatrix}, \quad \mathbf{C} = \begin{bmatrix} 1 & 0 \\ 0 & 1 \end{bmatrix}, \quad \mathbf{x} = \begin{bmatrix} \Delta x \\ \Delta \dot{x} \end{bmatrix} \tag{8.9}$$

:

Numerical values are found for k_f and k_{xp} for the initial bubble position and wave frequency are now found and the output of the linearized model is shown. k_{xp} will be considered first. This term corresponds to the maximum acoustophoretic force a bubble could experience if it was in an antinode. To demonstrate the variance of the maximum acoustophoretic force amplitude as a function frequency, it has been solved for numerically for a bubble with radius of 100 μm and is shown plotted in Figure 8.3.

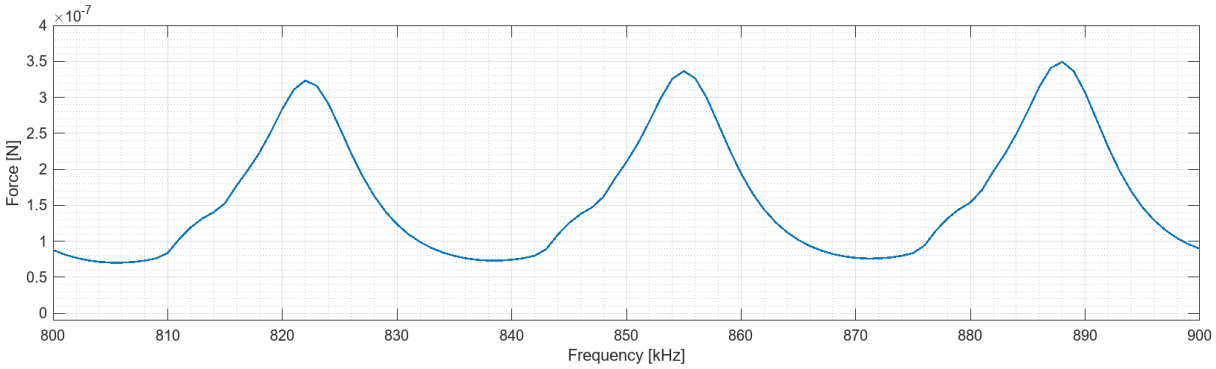

Figure 8.3: This figure shows the maximum attractive force an air bubble with a radius of 100 µm will experience in olive oil as a function of frequency.

It can be seen that the value of maximum acoustophoretic force and, therefore k_{xp}, varies periodically as a function of frequency with a slight gradient over the range shown. The value that has been selected as a linearizatino point is $1.5 \cdot 10^{-7}$ because it is at approximately halfway between the maximum and minimum values. This means that the streaming force estimate will always be somewhat close to the expected value, though it is worth considering that, it can still be off by a factor of up to 2.5. Bubbles are expected to controlled to different reference locations and this is done by moving acoustic nodes along with the air bubble. For this reason, the frequency is expected to span over multiple acoustic maximums and minimums during the control trajectory and, therefore, choosing a middle value for the amplitude of the acoustophoretic force is a necessary and acceptable compromise.

It can be noted from Equation 5.28 on page 31 that the k_{xp} coefficient scales with an η value as given below, where r_{p0} is 100 μm as given in Equation 8.10.

$$\eta = \left(\frac{r_p}{r_{p0}} \right)^3 \tag{8.10}$$

The second value that must be estimated is k_f. If the air bubble dynamics are considered to be similar to a mass spring damper system, this coefficient can be thought of as the prestressing a spring could experience that would make the bubble attracted to different steady state locations. It has been shown in Figure 5.8 on page 33 that the change of node positions is dependent on the initial bubble position.

The method selected for numerically linearizing the change of node position is to use the acoustophoretic force expression to find the nearest node location from an initial air bubble position. The method of finding the nearest node location is to perform a one dimensional search algorithm to find the nearest node by defining this to be the point where the acoustophoretic

force is at a minimum. The found nearest node location will be within one half wavelength of the reference air bubble location and therefore, the movement of this node is deemed representative of the movement for the real experimental node. With an input frequency of greater than 700 kHz, the modelled node location will always be within 1 mm of the the reference bubble and therefore, the modelled bubble should move similarly to the reference bubble. After this nearest node is found, the simulated frequency in the acoustophoretic force is adjusted by 5 hertz in the positive and negative direction and the found change of the node locations are used to calculate k_f using Equation 8.11:

$$k_f = \frac{\Delta x_{node}}{\Delta f} = \frac{x_{node.f+5Hz} - x_{node.f-5Hz}}{10Hz} \tag{8.11}$$

The node change constant can be seen for the different initial bubble locations in Table 8.1.

Table 8.1: This table shows the different node constant values as the distance from the transducer is changed. The initial bubble location refers to the experimentally found initial bubble position.

Initial Bubble Location	k_f
8.4	2.653e-8
12.7	1.873e-8
15.4	1.248e-8

It can be noted from Table 8.1 that the change of the node location varies by a factor of greater than 2 for the bubble locations shown, with the bubbles closer to the transducer having a greater node movement coefficient. This corresponds to there being a different input gain value, k_f in the system, as the absolute value of the position state diverges from the initial linearization point. This also means that, as the bubble begins to move further away from the initialized node, the greater the error of the node position estimation and, therefore, the greater the expected disturbance experienced by the air bubble as compared to the linearized dynamics.

8.4 Design of PI controller For Specific Particle

This section presents the design process of a PI controller that is capable of controlling the horizontal position of an air bubble in olive oil. This is done by first analyzing the air bubble linear dynamics, followed by assigning PI controller parameters. The designed controller is then tested on the nonlinear model and on experimental data. A specific air bubble with a radius of 100µm at an initial distance from the transducer of 8.4 mm is used when designing the PI controller.

Initial linearized values for have been evaluated for the chosen bubble and can be seen shown in in Table 8.2.

Table 8.2: This table gives an overview of the air bubble parameters upon initialization of the LKF.

Position	Nearest Node	r_p	K_x Value	K_f Value	B	M
8.4	8.6	127e-6	1.7e-8	3.1e-3	9.6e-5	7.5e-9

8.4.1 Linearized Model Dynamics

The state space matrix form of the linearized system is repeated below:

$$\dot{X} = \mathbf{A} \cdot X + \mathbf{B} \cdot u \tag{8.12}$$

$$Y = \mathbf{C} \cdot X \tag{8.13}$$

Where

$$\mathbf{A} = \begin{bmatrix} 0 & 1 & 0 \\ \frac{-k_f}{m} & -\frac{B}{m} & \frac{1}{m} \end{bmatrix}, \quad \mathbf{B} = \begin{bmatrix} 0 \\ \frac{k_x \cdot k_f}{m} \end{bmatrix} \tag{8.14}$$

The linear model has been plotted alongside experimental data and can be seen in Figure 8.4.

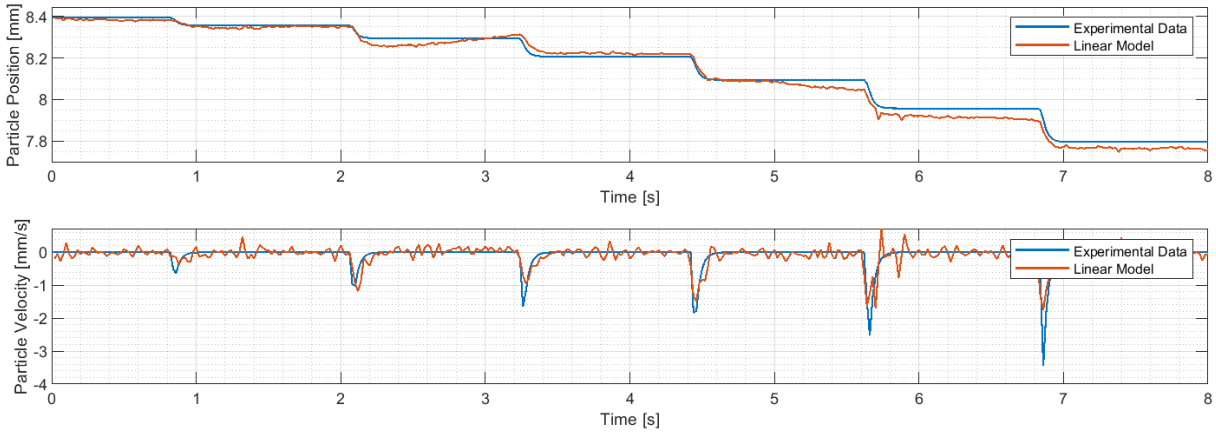

Figure 8.4: The linear model is plotted alongside the experimental data from a constantly increasing step input. For a particle with a radius of 100 µm and an initial distance of 8.4 mm from the transducer face.

It can be seen in Figure 8.4 that the linear model appears to fit very well with the experimental data. For this reason, the linear model is deemed acceptable for control design. To better understand the dynamics for the air bubble, a bode plot of the pulse transfer function system dynamics has been plotted and can be seen shown in Figure 8.5.

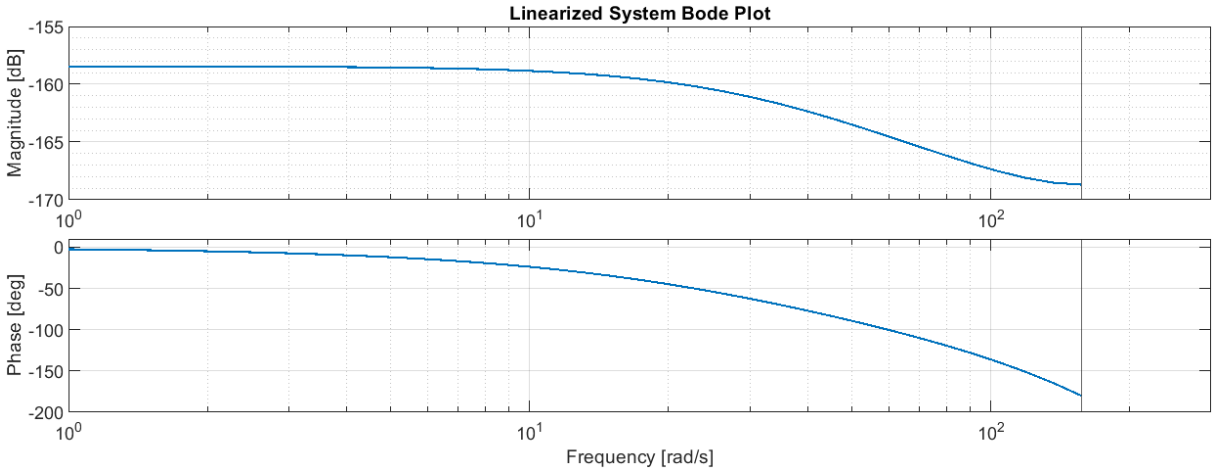

Figure 8.5: This figure shows the bode plot of the pulse transfer function of an air bubble with a radius of 127 µm at a distance of 11 mm away from the transducer. The black line indicates the Nyquist frequency and is located at 25 Hz, or 157 rad/s.

A couple of things can be noted from this bode plot. The first is that, for frequencies less than 10 rad/s, the system response is a static gain. This makes intuitive sense as when the input frequency is changed, the position of the attractive domain force is changed to a given position and it is here that the air bubble will settle. It is worth acknowledging that the steady state gain is dependent on the distance the air bubble is from the transducer. To ease analysis, this section only analyzes the dynamics for a given air bubble at a given position and this change of steady state gain can be considered as a disturbance. Air bubbles are only made to move up to 3 mm from the initial linearization point and therefore this disturbance is assumed to be small and manageable by the low frequency disturbance rejecting properties of a PI controller.

There is also a break point at approximately 10 rad/s and this is due to the viscous effect of the fluid, giving the system a natural damping. The damping of the system also changes with how close the system is to resonance. When the input frequency is close to resonance, the acoustic attractive force will be greater and the break frequency will be pushed to a higher frequency. The opposite occurs when the input frequency is far away from resonance. The selection of the attractive node force for the linearization point is such that the acoustic force amplitude will be both greater and less than the linearization point as the input frequency changes during particle position actuation.

8.4.2 Specifying Bubble Dynamics

A simple PI controller has been designed such that the gain margin and phase margin is high. The bode plot of this can be seen in Figure 8.6. The controller parameters can be seen in the Equation below:

$$G_{cont.c}(s) = \frac{k_i}{s} \cdot (s + k_{pol}) = \frac{5e6}{s} \cdot (s + 100) \tag{8.15}$$

$$G_{contr.d}(z) = k_p + \frac{T_s \cdot k_i \cdot (z+1)}{2 \cdot (z-1)} \tag{8.16}$$

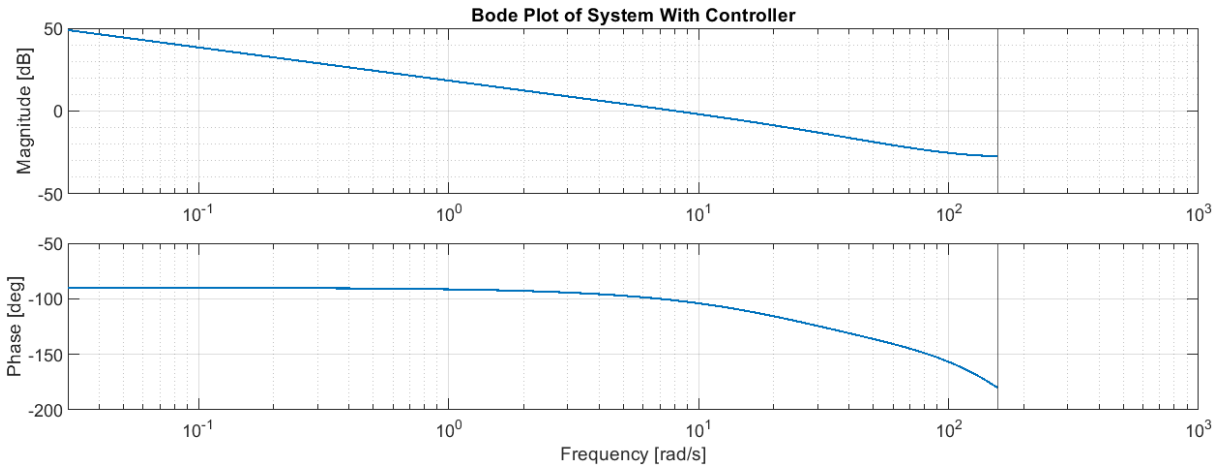

Figure 8.6: The bode plot of the pulse transfer function of the system and PI controller. The black line indicates the Nyquist Frequency of the system. The gain margin is 28 deg at 157 rad/S and the phase margin is 78 deg.

It can be seen in Figure 8.6 that the bandwidth of the system is just over a decade before from the Nyquist Frequency. The controller design goals stated that the dynamic response of the system should be able to follow a reference of 1 mm/s. For this reason, the controller

is decided to be tuned fairly aggressively and, an outcome of this is to make the bandwidth fairly close to the Nyquist Frequency. A difference between the bandwidth and the Nyquist Frequency is deemed to be acceptable for the linear system, and has been shown to be sufficient in the nonlinear system. To demonstrate this, the controller has been implemented and the control response from the nonlinear and the linear model have been plotted alongside each other in Figure 8.7

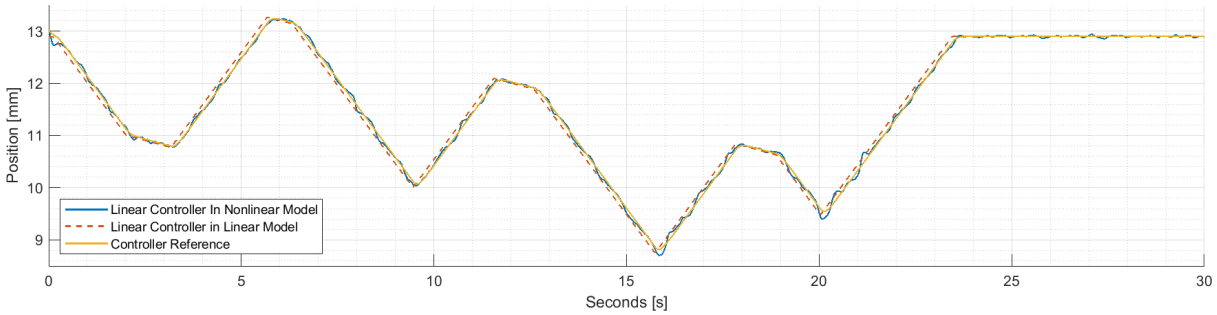

Figure 8.7: This figure shows the position response of an air bubble being controlled by the PI controller with a k_p value of 5e6 and a k_i value of 100 implemented in the nonlinear model on an air bubble with a radius of 127µm.

It can be seen from Figure 8.7 that the controller is able to actuate the bubble to the desired location. However, at times, 16 and 21 seconds, the controller appears to have difficulty actuating the particle and oscillation can be seen when the reference velocity changes sign. The fact that this oscillation only occurs intermittently suggests that the disturbance the system experiences can be shown to vary throughout the assigned reference trajectory. This oscillation coincides with the amplitude of the acoustophoretic force being near a minimum. This reduces the actuation potential of the input and causes the air bubble to oscillate.

To further demonstrate the difference between the linear and nonlinear model, the position and velocity error when implementing the controller on the linear and nonlinear model can be seen plotted in Figure 8.8

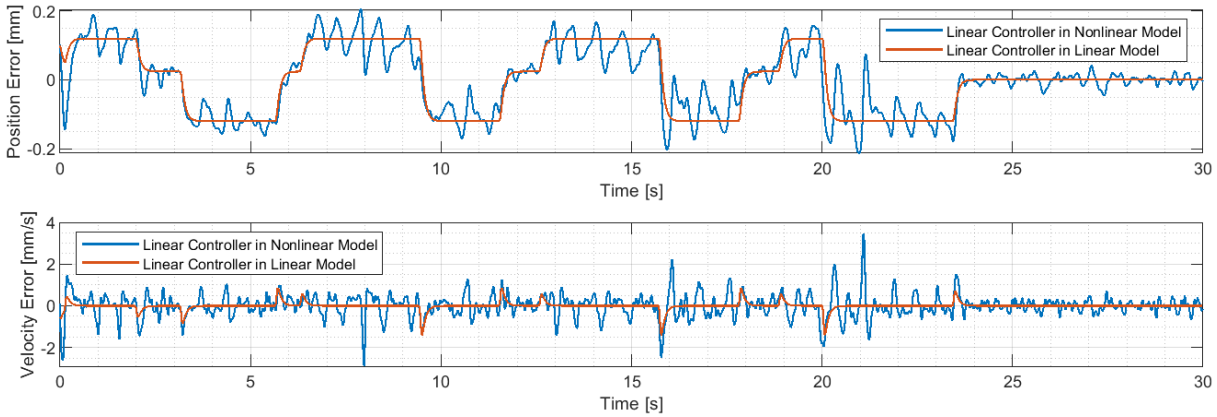

Figure 8.8: This figure shows the position error (top) and velocity error (bottom) when implementing the linear controller in the nonlinear and linear model, respectively

When looking at the top plot in Figure 8.8, a number of observation can be made about the controller design. The first is that the low frequency response between the linear and nonlinear model appears to be similar. The difference is the oscilation that occurs when the velocity reference is not zero. This oscillation occurs due to the constantly changing damping of of the system associated with the amplitude of the attractive force varying greatly over the large range of frequency that the input experiences.

Disturbance Rejection

The oscillatory disturbance that the controller has to reject in the nonlinear model is due to the changing maximum acoustophoretic force on the air bubble as the frequency is changed. This changing force can be interpreted as a disturbance force that the PI controller has to reject. The frequency of this disturbance f_{dist} can be understood as a function of the slew rate and the input frequency. The maximum and minimum force every time the input causes acoustic resonance in the system. Acoustic resonance occurs every time half the pressure wave wavelength aligns with the length of the chamber. Resonance is modelled to occur at the following frequencies:

Freq	720 [kHz]	752 [kHZ]	783 [kHz]
Frequency Difference Between Resonance	32 [kHz]	32[kHz]	31 [kHz]

Using the previously established k_{node} value, the expected disturbance frequency, f_{dist} can be solved for by using the following equation, where v_{max} is the maximum allowed change of reference position:

$$f_{dist} = \frac{v_{max}\left[\frac{m}{s}\right]}{\text{Node Movement per Freq}\left[\frac{m}{Hz}\right] \cdot \text{ Freq per Resonance } [Hz]} = \frac{.001}{k_{node} \cdot 32000}[Hz] \quad (8.17)$$

This can then be used to calculate what the frequency of the expected disturbance is when the bubble is moving at the maximum reference velocity:

Distance From Transducer	8.4 [mm]	12.7 [mm]	15.4 [mm]
$k_x\left[\frac{m}{Hz}\right.$	2.65e-8	1.86e-8	1.25e-8
$f_{dist}[Hz]$	1.2	1.68	2.488

It can be noted that the further away the bubble is from the transducer, the higher the expected disturbance frequency will occur. Because the k_x value is lower for the further away bubbles, these bubbles also experience a lower steady state gain. This lower steady state gain reduces the bandwidth of the PI controller. Because the controller cannot be tuned more aggressively due to Nyquist Frequency stemming from the sample frequency of the camera, this disturbance must be accepted as an expected component of the system's control response and little more can be done to mitigate this effect.

Disturbance is also present to the system in the form of the acoustophoretic streaming force. To test to what extent the control system is able to reject disturbance forces, a sawtooth disturbance force, meant to represent the unknown streaming force has been modelled in the nonlinear system and the control response when this occurs can be seen plotted in Figure 8.9.

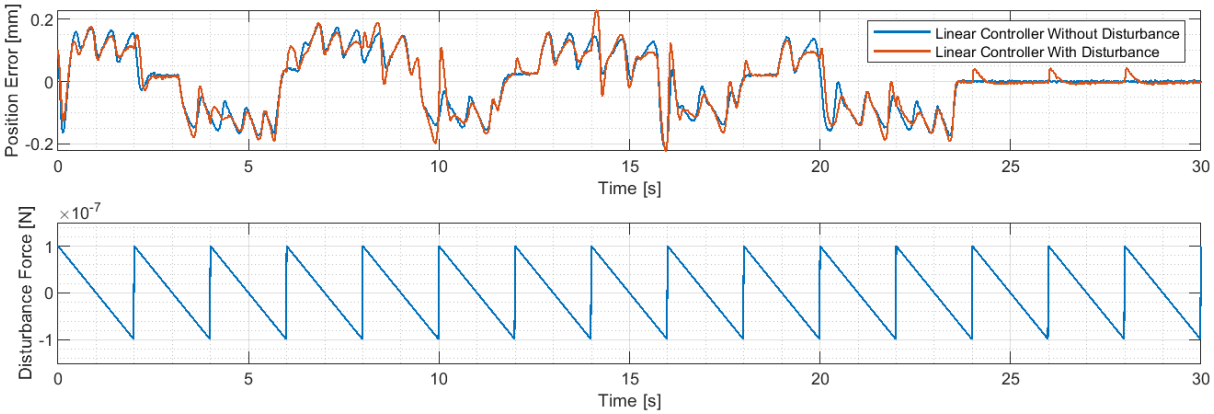

Figure 8.9: This figure shows the difference between the error of the system with and without a sawtooth disturbance with an amplitude of 10e-8 N and a frequency of .5

It can be seen in Figure 8.9 that the linear controller that has been designed is capable of rejecting a periodic sawtooth disturbance with an amplitude of 10 N. The disturbance rejecting capability of the PI controller is shown to be able to acceptably reject the disturbance. It can be noted that if the disturbance is greater than this, the controller fails. This is acceptable, because the disturbance shown in the Extended Kalman Filter in Figure 7.11 on page 57 showed that the disturbance is shown not to often be higher than this.

8.4.3 Experimental Results

The linear controller has been implemented in the experimental setup. A particle of size 105 micrometers has been controlled and the trajectory can be seen in Figure

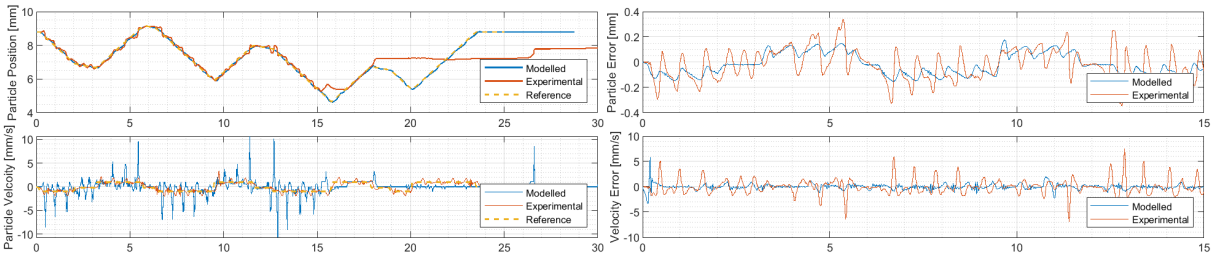

Figure 8.10: This figure shows the velocity and position reference for a bubble with particle radius 105 μm. The top and bottom left show the experimental position and velocity plotted along side the same particle modelled in the nonlinear model and the reference trajectory. The two right figures shows the modelled and experimental position and velocity errors.

The data shown in Figure 8.10 is representative of the control response when different bubbles have been attempted to be controlled. The controller had difficulty controlling particles over the full reference trajectory. This appears to be the case because the disturbing oscillation that occours is greater than what has been modelled. The oscillatory nature of the disturbance and its frequency being similar to that which was modelled suggests that the qualitative characterization of the disturbing oscillation is correct, though its amplitude appears to be underestimated. This is likely due to either an underestimation of the amplitude of the pressure wave generated by the transducer or an incorrectly estimation the wave reflection damping coefficient in the model.

Another thing that can be considered from the control response shown in Figure 8.10 is that the controller is capable of actuating the particle for the majority of the reference trajectory and it is first after 15 seconds that the controller fails. This is the the same case as was

found experimentally for other bubbles. The experimental implementation of the controller has shown bubbles are able to be controlled for a travel distance of up to 3.5 mm. If the plastic particle that the bubble is made to be actuated towards is close enough to the initial bubble position, the controller may still be viable for its intended purpose, as the disturbance is shown to be highest when the air bubble travels larger distances. For this reason, if the air bubble only travels a short distance, the expected disturbance can be expected to be lower. Ultimately, the failure of the control response shown in Figure 8.10 shows that the PI controller is likely tuned too aggressively.

Bubbles With Different Radius

One factor that has been shown to worsen the PI controller's response is if the controlled bubble radius is not the same as the bubble that was used during linearization. When the bubble radius is changed, so does its mass and viscous force and therefore, its dynamics. To show how the PI controller fails to actuate particles with a different radius than was used for design control, the controller was made to actuate a particle with a radius of 77µm. The results of using the PI controller in the nonlinear model and experimentally can be seen plotted in Figure 8.11.

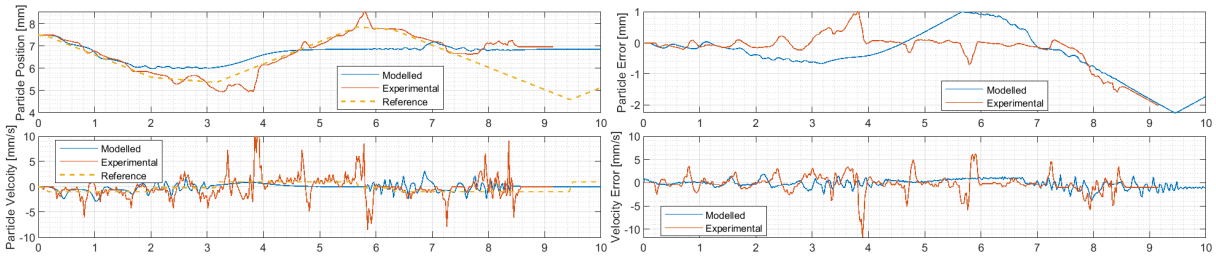

Figure 8.11: This figures shows the control response of an air bubble with a radius of 77µm. The two left plots are the position and velocity plots. The two right plots are the position and velocity error. The model input saturates at a frequency of 400 kHz between 4 seconds and 8 seconds. The experimental input frequency saturates from 8 seconds.

It can be seen in Figure 8.11 that the air bubble appears to be easier to control experimentally than in the model, however they both demonstrate failure of the control system. This is because the input frequency saturates at 6 seconds and is no longer controllable. This has been shown to be the case for all bubbles with a radius less than 90 µm. To demonstrate what the influence of changing the mass and damping of bubbles does to the dynamics, bode plots over the pulse transfer function of air bubbles with different radiuses can be seen shown in Figure 8.12

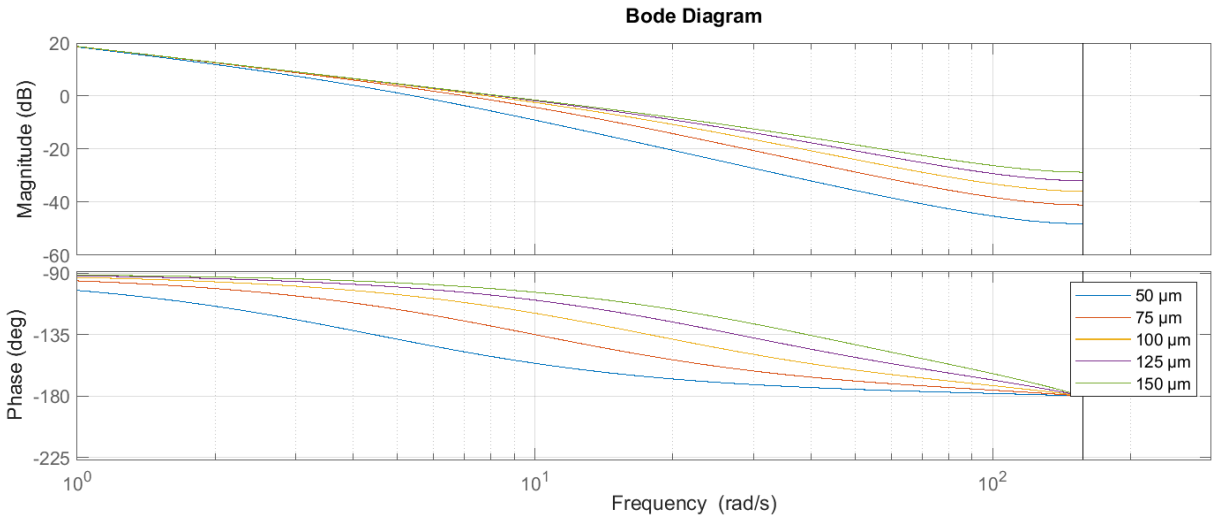

Figure 8.12: This figure shows the bode plot of different air bubble as the the radius is changed.

It can be seen in Figure 8.12 that the break frequency is reduced as the bubble radius reduces. On top of this, the phase shift is also pushed to lower a frequency. This acts to reduce the phase margin of the controller and reduces the disturbance rejecting capability, increasing the likelihood of instability. To more clearly show the trends associated changing the bubble radius size for the system response with the PI controller, a table over the phase and gain margins of different air bubble radius has been made and can be seen in Table 8.3.

Table 8.3: This table gives the gain and phase margin of an air bubble as the bubble radius is changed.

Bubble Radius	Gain Margin [dB]	Phase Margin [deg]	Bandwidth [rad/s]
50	257.5	39.1	5.5
75	112.9	54.7	7.1
100	62.6	66.0	7.9
125	39.5	73.3	8.3
150	27.2	78.0	8.5

What can be seen when looking at the phase margins from Table 8.3 is that the smaller the particle, the lower the phase margins. On top of this, the bandwidth appears to be connected to the particle radius size, with the larger particles having a higher effecting bandwidth. The bandwidth trend has diminishing effects after a radius of approximately 100 µm. It can also be seen that there is a trade off between gain and phase margin as the bubble size reduces, with small bubbles having a higher gain margin, implying better disturbance rejection, but a lower phase margin, suggesting higher susceptibility to oscillation and instability.

8.5 Updated PI Controller

Another controller has been designed with a lower proportional gain, k_p. The new controlled system margins and bandwidth can be seen as a function of bubble radius in Table 8.4

Table 8.4: This table gives the gain and phase margin of an air bubble with the old and new controllers. The old control parameters are : kp = 5e6 , ki 100. The new control Parameters are kp=2e6, ki = 100.

	Old Controller			New Controller		
Radius	GM [dB]	PM [deg]	BW [rad/s]	GM [dB]	PM [deg]	BW [rad/s]
50	257.5	39.1	5.5	643	56.9	2.9
75	112.9	54.7	7.1	282.4	71.8	3.3
100	62.6	66.0	7.9	156.5	79.2	3.4
125	39.5	73.3	8.3	98.85	83	3.4
150	27.2	78.0	8.5	68.1	85.1	3.5

By reducing the input gain from 5e6 to 2e6, the phase margin is able to be maintained above 55 deg for the bubble radius range of interest. On top of this, the gain margin is also maintained to be high. The cost of this is the reduction of the particle bandwidth. However, the bandwidth range over the bubble radius is held quite stable, only varying by approximately 17 percent. The consistency of the system response parameters make it a more appropriate controller for the control case and it is therefore accepted. The new controller has been shown to be much more stable than the previous controller and an experimental example of the control trajectory has been been plotted alongsisde the modelled response in Figure 8.13.

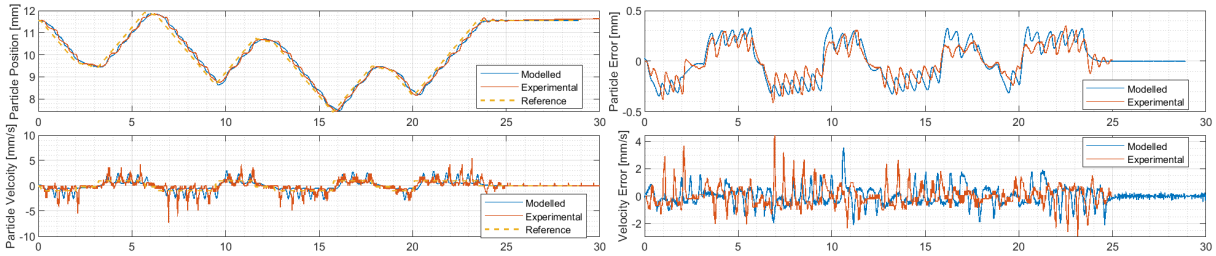

Figure 8.13: This figure shows the experiemtnal control response to the new controller with a bubble radius of 80 µm.

One surprising thing of note when looking at the top right plot of Figure 8.13 is the similarity between the experimental and simulated error dynamics. The error oscillation occurring when the velocity is not zero has a very similiar oscilation frequency and amplitude as to that which was modelled as can be seen when comparing the orange and blue lines between 4 and 6 seconds and 7 and 9 seconds. When looking at the bottom right figure, the velocity error appears to have higher peak values, but otherwise appear to be very similiar in the order of magnitude. The velocity error is also not used in the control law and therefore the difference in the amplitude peaks is acceptable.

Node Skipping

While the similiarity between the modelled response and experimental response shown in Figure 8.13 is striking, this conformity between the modelled response and experimental response does not always occur. Sometimes, the acoustic streaming disturbance force influences a bubble with a high enough force that the bubble is not able to follow the acoustic attractive force of the nearest node.

The PI controller can be thought to act as a "guide" that pushes the bubble along with a single acoustic node by moving that node to the desired reference location slow enough that the bubble can follow along. However, when a bubble starts to experience a disturbance force that the controller is not able to reject, the integrator component of the controller continues to

integrate the input value and thus, the node location. This can cause the input to "skip" a node and have the bubble fall behind to an adjacent acoustic node. An example of the controller almost loosing control of the bubble but then regaining control can be seen plotted in Figure 8.14.

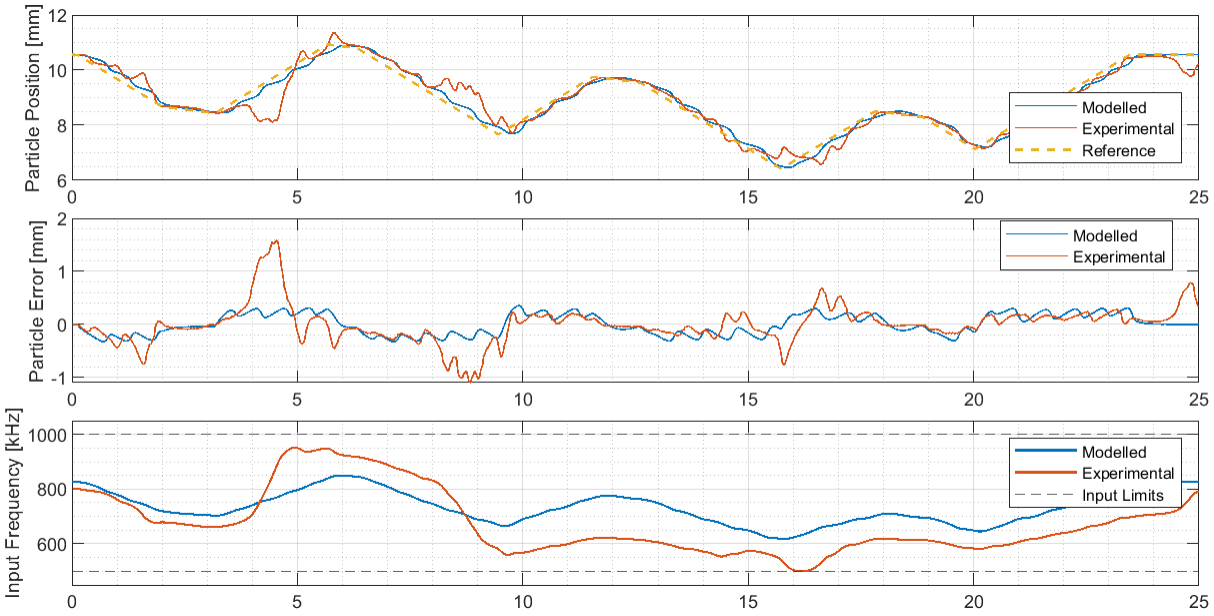

Figure 8.14: This figure shows the trajectory of a particle with radius of 80µm and a ki and kp of 100 and 2.5e6 respectively. The input gain is seen to almost saturate in the experimental setup at 4 and 6.5 seconds.

It can be seen when looking at the bottom plot of Figure 8.14 that, for the majority of the bubble trajectory, the experimental and modelled input appear very similar. There are, however, two locations when they diverge. This is at approximately 4 seconds and 8 seconds. Here, a large jump occours in the difference between the modelled and experimental input frequencies. When looking at the middle plot, this can be seen to coincide with the air bubble getting a high velocity and changing acoustic node paths.

In Figure 8.14 it is shown that the controller is still able to correctly actuate the bubble even if an acoustic node is "skipped". This has been shown to be the case for the majority of the bubbles that were actuated, though, sometimes, control of the bubbles was lost. Overall, despite this occurring, the controller is able to to achieve the design objectives.

8.5.1 Discussion

Node Control

One aspect that was explored during the writing of this thesis was the use of the nonlinear model to use the modelled node movement as an input saturator. The purpose of this was to ensure that the input to the system would never cause the bubble to be further away than the nearest acoutophoretic force peak. In this manner, the acoustophoretic force that the bubble would experience would be made to be made to saturate at the maximum or minimum of the sin function. Ultimately the implementation of this proved difficult due how much the input frequency changed during operation and was replaced by the reference slew rate limitor which resulted in a similar outcome. Further development of this control strategy could be explored as an option for an improvement of the control response.

Dynamic Loop Shaping

Another opportunity for the improvement of the control response that was considered is to create a different linear controller every time the system is initialized. In this manner, the gain and phase margin could be specified from the initialization of the control system and a more consistent control response could be acquired. The controller used in this section was shown to be able to achieve the design purpose, this method was not required. The bottleneck of the system was shown to be the low sample frequency from the camera and for this reason, the method was not implemented, though it is likely this method could improve the control response.

Tighenting Input Saturation

The input saturation that was implemented for the transducer was put in place to limit the effect of the transducers output frequency response. This is because the output pressure amplitude of the transducer at the transducer's resonant frequency is much higher than at different frequencies and had a tapering off affect as the frequency difference from resonance increased. This variation was ultimately accepted as being a part of the disturbance the bubbles would experience, as the actual location of the acoustic nodes was not affected by the transducer output pressure amplitude. Only the amplitude of the attractive acoustophoretic force was changed due to the transducer frequency response. Because the reference position trajectory had a fairly slow slewrate, this disturbance was shown not to have that high of an influence on the overall control response.

A method that was experimented with during this master's thesis was to limit the span that the output of the controller would change to be a much tighter frequency range. This worked by having the transducer simply jump to a lower or higher frequency that would result in the node position being located at the same distance. This limited the operating the frequency range the transducer would output and reduced the influence of the transducer's own frequency response. The designed PI controller was shown to be mostly robust against this disturbance, though when the transducer was at resonance, bubbles would sometimes be pushed from node to node and control was lost. A smaller frequency range would reduce the influence of this problem and could be a topic for further control design.

8.6 Conclusion

The PI controller designed in this chapter demonstrated the ability to actuate air bubbles over a large range of positions. The natural disturbance rejecting properties of a PI controller made it an adequate fit for the design purpose. The control design process was limited by the low sample frequency of the camera, and a controller with a higher bandwidth than the one shown would likely experience more stability issues than the one demonstrated.

Chapter 9

Conclusion

This Master's Thesis has demonstrated both the practical viability for merging the fields of acoustofluidics with flotation along with presenting an integrated mechatronic based approach to the analysis of air bubbles experiencing the acoustophoretic force.

The control strategy presented for the single axis control of air bubbles was shown to be able to facilitate the interaction between air bubbles and plastic in a manner that was satisfactory with the hardware limitations present. The lack of attractive force between the air bubbles and plastic particles in olive oil means that further testing and iterations of the Acoustic Tweezing Aided Flotation system is required before the system can be considered an implementable technology, though the opportunities that the approach presents are intriguing.

The 1D dynamic acoustophoretic force equation presented by this thesis was shown to provide a sound basis for further dynamic analysis of air bubbles. The modelling uncertainties present during the application of this force expression was also shown to be characterisable by the presented Extended Kalman Filter for an air bubble at rest with a constant sinusoidal pressure wave frequency. The Extended Kalman Filter's lack of robustness against modelling uncertainties associated with the incorrect selection of modelling parameters means that further iterations of the Extended Kalman Filter are required before a "general" solution to the characterization of the fluid streaming force affecting an air bubble is achieved.

In summary, this Thesis serves as a single straw placed on the hay bale required to achieve Acoustic Tweezing Aided Flotation.

Chapter 10

Further Work

The following topics provide areas to continue research on:

More Rigorous Approach to Pressure Field Equation

This Thesis took a minimalist approach to the modelling of the pressure fields in the fluid. The approach taken by this thesis demonstrated the practical use of a simplified 1D model of pressure fields. With the computational capacity available in modern engineering, a more numerically intensive approach, such as computational fluid dynamics, to the characterization of the acoustophoretic force is an intuitive next step for the analysis required for higher dimensional control strategies. With a simple geometry, the multipole output characteristics of the transducer wave generation could also be taken into account, allowing much higher degree of accuracy to be achieved while acoustic modelling.

Inclusion of More Axis of Control

The air bubble control structures shown in this thesis only controlled the horizontal air bubble movement directly with the buoyancy effect of air bubbles allowing for effective control of vertical movement. The last directional plane, the depth plane, was not controlled by the methods presented.This could be achieved through the use of a second transducer set orthogonal to the first transducer. This method does require depth directional feedback. An easy solution to this is to add a second camera. However, simply pulsing the bubble along this access could likely also achieve air bubble plastic partial interaction, as when the bubble goes out of focus of the camera, the bubble edges being to blur and this could potentially used as a metric for depth directional position.

There is the potential for two axis pressure waves interacting with each other and potentially reducing the control potential for this method. This requires more research, though the findings by [1] suggest that this may not be a significant hurdle.

Alternative Control Strategies

This thesis has taken focus on the viability for acoustic tweezing to facilitate air bubble particle interaction. For this reason, an individual bubble control strategy has been selected. However, when an individual particle is actuated, all of the air bubbles in the fluid also experience an acoustophoretic force and are attracted to the nearest acoustic node. It could therefore be theorized that much more plastic could be moved with a "sweeping" air bubble motion. This could potentially have the effect of performing a windshield wiper movement and a region

of particles could be swept away from a region of the cabin. This is left as a topic for further research.

Flotation Based Approach

The ease of implementation of the Acoustic Tweezing Aided Flotation system opens up the opportunity for taking a more flotation centered approach the analysis of the benefits of including acoustophoretic forces of ATAF. The analysis lens of the ATAF system taken by this thesis is one the field of mechatronic control whereby the micro scale interacting forces between the air bubbles and microplastics was largely hand waved and the emphasis was placed on the milliscale actuation of the air bubbles. Taking a more mineral processing and flotation based approach to ATAF system design would likely produce a more industrially viable version of the approach.

Visual Processing

A large amount of time was spent designing the visual processing algorithms used in the analysis and distinguishment between air bubble and plastic particle.There are qualitative difference between the properties of air bubble and plastic particles that the imfincircles() MatLAB function is not good at distinguishing. Recent advancements in machine learning for visual processing could practically be applied in this pursuit. A machine learning approach applied to the characterization of air bubbles and particles would likely quickly outperform the methods used by this Thesis. This could potentially reduce the computational strain on the controller and provide a benefit in design of similar systems.

Bibliography

[1] M Baudoin and J.-L Thomas. "Acoustic Tweezers for Particle and Fluid Micromanipulation". eng ; jpn. In: *Annual Review of Fluid Mechanics* 52.1 (2020), pp. 205–234. ISSN: 0066-4189.

[2] *Bentowave Transducer Datasheet : BII7580*. https://www.benthowave.com/products/Specs/BII7580Datasheet.pdf. Accessed: 2014-05-29.

[3] Jean-Philippe Bonnet et al. "Dynamic viscosity of olive oil as a function of composition and temperature: A first approach". In: *European Journal of Lipid Science and Technology* 113 (Aug. 2011). DOI: 10.1002/ejlt.201000363.

[4] Christopher Brennen. "Cavitation and Bubble Dynamics". In: *Cavitation and Bubble Dynamics* 44 (Jan. 1995). DOI: 10.1017/CBO9781107338760.

[5] Patrick S. Bäuerlein et al. "Fate of microplastics in the drinking water production". In: *Water Research* 221 (2022), p. 118790. ISSN: 0043-1354. DOI: https://doi.org/10.1016/j.watres.2022.118790. URL: https://www.sciencedirect.com/science/article/pii/S0043135422007436.

[6] Yuran Chen et al. "A review of effects and applications of ultrasound in mineral flotation". In: *Ultrasonics Sonochemistry* 60 (2020), p. 104739. ISSN: 1350-4177. DOI: https://doi.org/10.1016/j.ultsonch.2019.104739. URL: https://www.sciencedirect.com/science/article/pii/S1350417719307503.

[7] Fenglian Fu and Qi Wang. "Removal of heavy metal ions from wastewaters: A review". In: *Journal of Environmental Management* 92.3 (2011). Cited by: 7131, 407 – 418. DOI: 10.1016/j.jenvman.2010.11.011. URL: https://www.scopus.com/inward/record.uri?eid=2-s2.0-78650520448&doi=10.1016%2fj.jenvman.2010.11.011&partnerID=40&md5=ffe4b3631b10d44ef9ae0a624edf9769.

[8] Matthias Holland. *An introduction to the extended Kalman filter*. eng. Mathematics research developments. New York: Nova Science Publishers, 2020. ISBN: 9781536188752.

[9] M.H. Kandemir et al. "Selective particle separation on centimeter scale using a dual frequency dynamic acoustic field". eng. In: *Ultrasonics* 114 (2021), pp. 106411–106411. ISSN: 0041-624X.

[10] Carsten Lassen et al. "Microplastics: Occurrence, effects and sources of releases to the environment in Denmark". In: 2015. URL: https://api.semanticscholar.org/CorpusID:131888965.

[11] Peter B Muller et al. "Ultrasound-induced acoustophoretic motion of microparticles in three dimensions". eng. In: *arXiv.org* (2013). ISSN: 2331-8422.

[12] Ron Musiak, Bart Lipkens, and Neeraj Magotra. "Design of a control system for acoustophoretic separation". eng. In: (2013), pp. 1120–1123. ISSN: 1548-3746.

[13] Muhammad Salman Nasir et al. "Innovative technologies for removal of micro plastic: A review of recent advances". In: *Heliyon* 10.4 (2024), e25883. ISSN: 2405-8440. DOI: https://doi.org/10.1016/j.heliyon.2024.e25883. URL: https://www.sciencedirect.com/science/article/pii/S2405844024019145.

[14] *NATIONAL WEATHER SERVICE: Speed of Sound*. https://www.weather.gov/epz/wxcalc$_s$*peedofsound*. Accessed: 2014-05-29.

[15] Tan Dai Nguyen et al. "Acoustofluidic closed-loop control of microparticles and cells using standing surface acoustic waves". In: *Sensors and Actuators B: Chemical* 318 (2020), p. 128143. ISSN: 0925-4005. DOI: https://doi.org/10.1016/j.snb.2020.128143. URL: https://www.sciencedirect.com/science/article/pii/S0925400520304937.

[16] J. Nilsson et al. "Review of cell and particle trapping in microfluidic systems". In: *Analytica Chimica Acta* 649.2 (2009), pp. 141–157. ISSN: 0003-2670. DOI: https://doi.org/10.1016/j.aca.2009.07.017. URL: https://www.sciencedirect.com/science/article/pii/S0003267009009222.

[17] Allan D Pierce. *Acoustics: An Introduction to Its Physical Principles and Applications*. eng. Third edition. Cham: Springer Nature, 2019. ISBN: 3030112144.

[18] Kim Ragaert, Laurens Delva, and Kevin Van Geem. "Mechanical and chemical recycling of solid plastic waste". In: *Waste Management* 69 (2017), pp. 24–58. ISSN: 0956-053X. DOI: https://doi.org/10.1016/j.wasman.2017.07.044. URL: https://www.sciencedirect.com/science/article/pii/S0956053X17305354.

[19] Joseph Rufo et al. "Acoustofluidics for biomedical applications". In: *Nature Reviews Methods Primers* 2.1 (2022). Cited by: 97. DOI: 10.1038/s43586-022-00109-7. URL: https://www.scopus.com/inward/record.uri?eid=2-s2.0-85130265808&doi=10.1038%2fs43586-022-00109-7&partnerID=40&md5=bdad452967088ab73355af24613496ee.

[20] Mikkel Settnes and Henrik Bruus. "Forces acting on a small particle in an acoustical field in a viscous fluid". eng. In: *Physical review. E, Statistical, nonlinear, and soft matter physics* 85.1 (2012), pp. 016327–016327. ISSN: 1539-3755.

[21] Paul Stevenson. *Foam Engineering: Fundamentals and Applications*. Cited by: 251. 2012. DOI: 10.1002/9781119954620. URL: https://www.scopus.com/inward/record.uri?eid=2-s2.0-84891584153&doi=10.1002%2f9781119954620&partnerID=40&md5=2d8496b51bae02756e0be144ebf02acf.

[22] Richard C. Thompson et al. "Plastics, the environment and human health: current consensus and future trends". eng. In: *Philosophical transactions of the Royal Society of London. Series B. Biological sciences* 364.1526 (2009), pp. 2153–2166. ISSN: 0962-8436.

[23] Chong qing Wang et al. "Flotation separation of waste plastics for recycling—A review". In: *Waste Management* 41 (2015), pp. 28–38. ISSN: 0956-053X. DOI: https://doi.org/10.1016/j.wasman.2015.03.027. URL: https://www.sciencedirect.com/science/article/pii/S0956053X15002214.

[24] Hui Wang, Yingshuang Zhang, and Chonqing Wang. "Surface modification and selective flotation of waste plastics for effective recycling——a review". In: *Separation and Purification Technology* 226 (2019), pp. 75–94. ISSN: 1383-5866. DOI: https://doi.org/10.1016/j.seppur.2019.05.052. URL: https://www.sciencedirect.com/science/article/pii/S1383586618336724.

[25] B.A. Wilis. "Flotation science engineering: K.A. Matis (ed.) Marcel Dekker, Inc., New York, 1995. 558 pps. Price 175.$ISBN0-8247-9264-5$". eng. In: *Minerals Engineering* 8.4 (1995), pp. 577–577. ISSN: 0892-6875.

[26] Jing Yan et al. “A sound approach: Exploring a rapid and non-destructive ultrasonic pulse echo system for vegetable oils characterization”. In: *Food Research International* 125 (July 2019), p. 108552. DOI: 10.1016/j.foodres.2019.108552.

Appendix A

Acoustophoretic Force Derivation

This Appendix links the expressions for the puressure waves to the acoustophoretic force equation. The MatLAB symbolic toolbox is used to aid in the algebra and symbolic differentiation performed in this section. This analysis will be broken up into three sections: the steady state pressure field forces, the initial transient, and the stopping transient.

A.1 Steady State Acoustophoretic Forces

The steady state expression for the pressure wave in the cabin can be expressed as the sum of Equations 5.16 Equations 5.17 when neglecting the heaviside function. The expression for the pressure field for the first four reflections can be expressed as the following:

$$\mathbf{P}(x,t) = \sum_{n=1}^{4} \beta^{2\cdot(n-1)} \cdot P_{amp} \cdot e^{j(\omega\cdot t - k\cdot x + 2\cdot(n-1)\cdot L/c)} + \sum_{n=1}^{5} \beta^{1+2\cdot(n-1)} \cdot P_{amp} \cdot e^{j(\omega\cdot t - k\cdot x + k\cdot(2\cdot n)\cdot L)} \tag{A.1}$$

The complex conjugate of Equation A.3 is given as the following:

$$\mathbf{P}^{*}(x,t) = \sum_{n=1}^{4} \beta^{2\cdot(n-1)} \cdot P_{amp} \cdot e^{j(-\omega\cdot t + k\cdot x - 2\cdot(n-1)\cdot L/c)} + \sum_{n=1}^{5} \beta^{1+2\cdot(n-1)} \cdot P_{amp} \cdot e^{j(-\omega\cdot t + k\cdot x - k\cdot 2\cdot n\cdot L)} \tag{A.2}$$

The spatial derivitive of Equation A.3 is given as the following

$$\nabla\mathbf{P}(x,t) = \sum_{n=1}^{5} -k \cdot \beta^{2\cdot(n-1)} \cdot P_{amp} \cdot e^{j(\omega\cdot t - k\cdot x + 2\cdot(n-1)\cdot L/c)} + \sum_{n=1}^{5} k \cdot \beta^{1+2\cdot(n-1)} \cdot P_{amp} \cdot e^{j(\omega\cdot t - k\cdot x + k\cdot 2\cdot n\cdot L)} \tag{A.3}$$

The pressure dependent contribution to the acoustophoretic force from the first reflection (n = 1) is given as the following :

$$F_{p,n=1} = real(\mathbf{P}^{*} \cdot \nabla\mathbf{P})_{n=1} = \frac{2 \cdot p_{amp}^{2} \cdot \beta \cdot \omega}{c} \cdot sin(\frac{2 \cdot \omega}{c}(L - x)) \tag{A.4}$$

For simplification of the next few terms, the following constants are introduced:

$$\sigma_1 = \frac{2 \cdot P_{amp}^{2} \cdot \omega}{c}, \quad \sigma_2 = \frac{2 \cdot c}{\omega}, \quad \sigma_3 = \frac{L \cdot \omega}{c} \tag{A.5}$$

To ease in readability, the equations are rewritten in vector form:

$$F_{p,n=1} = \sigma_1 \left[\beta\right] \cdot \left[sin(\frac{2\omega}{c} \cdot (L - x))\right] \tag{A.6}$$

$$F_{p,n=2} = F_{n=1} + \sigma_1 \begin{bmatrix} \beta^3 \\ \beta^5 \end{bmatrix} \cdot \begin{bmatrix} sin\left(\frac{2\omega}{c} \cdot (-x)\right) + sin\left(\frac{2\omega}{c} \cdot (2L - x)\right) \\ sin\left(\frac{2\omega}{c} \cdot (L - x)\right) \end{bmatrix}^T \tag{A.7}$$

$$F_{p,n=3} = F_{n=2} + \sigma_1 \begin{bmatrix} \beta^5 \\ \beta^7 \\ \beta^9 \end{bmatrix} \cdot \begin{bmatrix} sin\left(\frac{2\omega}{c} \cdot (-L - x)\right) + sin\left(\frac{2\omega}{c} \cdot (3L - x)\right) \\ sin\left(\frac{2\omega}{c} \cdot (-x)\right) + sin\left(\frac{2\omega}{c} \cdot (2L - x)\right) \\ sin\left(\frac{2\omega}{c} \cdot (L - x)\right) \end{bmatrix}^T \tag{A.8}$$

$$F_{p,n=4} = F_{n=3} + \sigma_1 \begin{bmatrix} \beta^7 \\ \beta^9 \\ \beta^{11} \\ \beta^{13} \end{bmatrix} \cdot \begin{bmatrix} sin\left(\frac{2\omega}{c} \cdot (-2L - x)\right) + sin\left(\frac{2\omega}{c} \cdot (4L - x)\right) \\ sin\left(\frac{2\omega}{c} \cdot (-L - x)\right) + sin\left(\frac{2\omega}{c} \cdot (3L - x)\right) \\ sin\left(\frac{2\omega}{c} \cdot (-x)\right) + sin\left(\frac{2\omega}{c} \cdot (2L - x)\right) \\ sin\left(\frac{2\omega}{c} \cdot (L - x)\right) \end{bmatrix}^T \tag{A.9}$$

An expression for calculating the force up until the mth set of reflections can be given as the following

$$F_p(m) = \sigma_1 \cdot \sum_{n=1}^{m} \left[\sum_{i}^{n-1} \beta^{2(n+i)-3} \cdot sin\left(\frac{2L\omega}{c}(n - i - 1) \cdot L - x\right) \right.$$
$$\left. + \beta^{2(n+i)-3} \cdot sin\left(\frac{2L\omega}{c} \cdot ((n - i + 1) \cdot L - z)\right) + F_{p,last}(n) \right] \tag{A.10}$$

Where:

$$F_{p,last}(n) = \beta^{1+(n-1)\cdot 4} \cdot sin\left(\frac{2\omega}{c}(L - x)\right) \tag{A.11}$$

Practically, when Equations A.10 and A.57 are given numerical values for β, c, ω, and L, an expression for the force field can be expressed as the summation of a single cos and sin function with an angular frequency of $2 \cdot \omega k$, where k is the wave number of the fluid. The final wave field can therefore be expressed as the following, where n is the number of reflections and a_i and b_i are the numerically solved contributions from the i_{th} set of reflections:

$$F_{p,final} = \sum_{i=1}^{n} a_i \cdot cos(2 \cdot k \cdot x) + b_i \cdot sin(2 \cdot k \cdot x) \tag{A.12}$$

This allows for easy modelling of the system during steady state.

The derivation from the force contribution from the velocity field, **V** at steady state, is the same as that for the pressure field due to the velocity field simply being a 90deg phase shifted version of the pressure field with a static gain. This is given as the following:

$$F_v(n) = F_p(n) \cdot (-\frac{i}{\omega \cdot \rho})^2 \tag{A.13}$$

Due to the expression for the steady state force field existing in the transient expression for the wave equation, the force field will first be shown at the end of Section A.1.1.

A.1.1 Initial Transient

In this Section, similiar to how the expression for the steady state acoustic force with reflecitons was derived, an expression for the first few terms of the transient wave equations will be calculated and a general expression for the nth reflection will be extrapolated. The analytical differentiation will be performed with the help of MatLAB's symbolic toolbox afterwhich, physical intuition about the system will aid in reducing the expression. If one considers the wave transient before any reflections have occoured, Equation A.14 can be used to represent the pressure field in a 1D space.

$$\mathbf{P}_{init}(t,x) = P_{amp} \cdot e^{j\cdot(\omega\cdot t - k\cdot x)} \cdot \mathbf{u}\left(t - \frac{x}{c}\right) \tag{A.14}$$

The fact that the step response is used has the added benefit of being able to be differentiated analyticaly. Differentiating Equation A.14 gives Equation A.15, where $\mathbf{P}_{harm}$ refers to the harmonic wave equation as was given in Equation 5.6:

$$\nabla P_{init} = \frac{\delta P_{init}}{\delta x} = \frac{1}{c}\cdot\delta\left(t-\frac{x}{c}\right)\cdot\mathbf{P}_{init}(t,x) + \mathbf{u}\left(t-\frac{x}{c}\right)\cdot\frac{\delta\mathbf{P}_{harm}}{\delta x} \tag{A.15}$$

$$\frac{\delta\mathbf{P}_{harm}}{\delta x} = -\frac{P_{amp}^2\cdot\omega}{c}\cdot e^{j\cdot(\omega\cdot t - k\cdot x)} \tag{A.16}$$

Equation A.14 can be combined with Equation A.15 to give an expression for the real product of the pressure field and its gradient:

$$F_{p,tr,n=0} = Re(\mathbf{P}^*_{init}\cdot\nabla\mathbf{P}_{init}) = -\frac{P_{amp}^2\cdot\omega}{c^2}\cdot\delta\left(t-\frac{x}{c}\right)\cdot\mathbf{u}\left(t-\frac{x}{c}\right) \tag{A.17}$$

A couple of observations can be made to Equation A.17. The first is that the product of the step and impulse function must be equal to the impulse function. A second observation is that a single wave being generated in a medium will only have an influence on the particles when it is first turned on. It can also be easily verified that a travelling pressure wave without an initial transient will have a net force of zero.

Because the heaviside step function and dirac delta function are distributions and not a function, its arguemnt does not need to be differentiated as according to the chain rule. However, the dirac function that is present in the system will still be included. This is because the impulse force that will be calculated will excite a mechanical object; the particle in question. This particle has an expression for its impulse response therefore meaning that the presence and amplitude of this dirac function has a physical significance.

The force of the first set of reflections is given using the same notation as the previous section:

$$F_{p,tr,n=1} = \sigma_1\begin{bmatrix}\beta^0\\ \beta^1\\ \beta^2\end{bmatrix}\cdot\begin{bmatrix} -\frac{1}{2\omega}\cdot\delta\left(t-\frac{x}{c}\right)\cdot\mathbf{u}\left(t-\frac{x}{c}\right) \\ -sin\left(\frac{2\omega}{c}(L-x)\right)\cdot 1\left(\frac{x-2L}{c}+t\right)\cdot\left[1\left(\frac{x}{c}-t\right)-1\right]+\sigma_4 \\ \frac{1}{2\omega}\cdot\delta\left(t+\frac{x}{c}-\frac{2L}{c}\right)\cdot\mathbf{u}\left(t+\frac{x}{c}-\frac{2L}{c}\right)\end{bmatrix} \tag{A.18}$$

Where σ_4 refers to the following term :

$$\begin{aligned}\sigma_4 = -\frac{1}{2\omega}\cdot\Bigg[&\delta\left(t+\frac{x}{c}-\frac{2L}{c}\right)\cdot cos\left(\frac{2\omega(L-x)}{c}\right)\cdot\left[1\left(\frac{x}{c}-t\right)-1\right]+\\ &\mathbf{u}(\frac{x-2L}{c}+t)\cdot cos\left(\frac{2\omega(L-x)}{c}\right)\cdot(\delta\left(\frac{x}{c}-t\right))\Bigg]\end{aligned} \tag{A.19}$$

The argument of the delta and step functions in the first term of Equation A.19 can be shown to have the following relationship:

$$\delta\left(t+\frac{x}{c}-\frac{2L}{c}\right)=\begin{cases}1, & T_\delta=0, \quad T_\delta=t+\frac{x}{c}-\frac{2L}{c}\\ 0, & T_\delta\neq 0\end{cases} \tag{A.20}$$

$$u\left(\frac{x}{c}-t\right)-1=-u\left(t-\frac{x}{c}\right) \tag{A.21}$$

Where

$$\mathbf{u}(t,x)=\begin{cases}1, & T_1\geq 0, \quad T_1=t-\frac{x}{c}\\ 0, & T_1<0\end{cases} \tag{A.22}$$

The expressions for the arguments T_1 and T_δ can be shown to have the following relationship be equal to eachother:

$$T_\delta=0\rightarrow t=-\frac{z}{c}+\frac{2L}{c} \tag{A.23}$$

$$T_1\geq 0\rightarrow t-\frac{z}{c}\geq 0 \tag{A.24}$$

$$z\leq L, \quad t\geq\frac{L}{c} \tag{A.25}$$

Because the physical limits of the system are $0\leq x\leq L$ and $t\geq 0$ the contribution from the dirac function will be present in the system. The time arguemnts in Equation A.19 have the following relationships:

$$T_\delta=t-\frac{z}{c}, \quad T_1=t+\frac{z}{c}-\frac{2L}{c} \tag{A.26}$$

$$\begin{gathered}t+\frac{z}{c}-\frac{2L}{c}\geq 0, \quad t-\frac{z}{c}=0\\ \frac{2z}{c}-\frac{2L}{c}\geq 0, \quad z\geq L\end{gathered} \tag{A.27}$$

The impulse function only has physical significance beyond the boundary conditions and therefore terms with this value will be neglected when looking at the next terms of the force. Equation A.18 can be shown to reduce to the following:

$$F_{p,tr,n=1}=\sigma_1\begin{bmatrix}\beta^0\\ \beta^1\\ \beta^2\end{bmatrix}\cdot\begin{bmatrix}-\frac{1}{2\omega}\cdot\delta\left(t-\frac{x}{c}\right)\\ sin\left(\frac{2\omega}{c}(L-x)\right)\cdot 1\left(\frac{x}{c}+t-\frac{2L}{c}\right)+\delta(t+\frac{x}{c}-2T_d)\cdot cos(\frac{2\omega(L-x)}{c})\\ \frac{1}{2\omega}\cdot\delta\left(t+\frac{x}{c}-\frac{2L}{c}\right)\end{bmatrix}^T \tag{A.28}$$

Which can be rewritten as:

$$F_{tr,M1}=\sigma_1\left[\beta^1\right]\cdot\mathbf{F}_{tr,M1}+\sigma_5\cdot\left[\beta^0\right]\boldsymbol{\delta}_{t-\frac{x}{c}}+\sigma_5\cdot\begin{bmatrix}\beta^1\\ \beta^2\end{bmatrix}\boldsymbol{\delta}_{t+\frac{x}{c}-2T_d} \tag{A.29}$$

$$\mathbf{F}_{tr,M1}=\left[sin\left(\frac{2\omega}{c}(L-x)\right)\cdot 1\left(\frac{x}{c}+t-2T_d\right)\right] \tag{A.30}$$

$$\delta_{t-\frac{x}{c}} = \delta\left(t - \frac{x}{c}\right)\left[-1\right] \tag{A.31}$$

$$\delta_{t+\frac{x}{c}-2T_d} = \delta(t + \frac{x}{c} - 2T_d)\begin{bmatrix} cos\left(\frac{2\omega(L-x)}{c}\right) \\ 1 \end{bmatrix} \tag{A.32}$$

Where

$$T_d = \frac{L}{c}, \quad \sigma_5 = \frac{P_{amp}^2}{c} \tag{A.33}$$

The force with reflections corresponding to n = 2 will be shown and simplified one exponent of β at a time:

$$F_{p,tr,n=2} = \sigma_1 \begin{bmatrix} \beta^2 \\ \beta^3 \\ \beta^4 \\ \beta^5 \\ \beta^6 \end{bmatrix} \cdot \begin{bmatrix} a_1 \\ a_2 \\ a_3 \\ a_4 \\ a_6 \end{bmatrix}^T \tag{A.34}$$

Where

$$\begin{aligned} a_1 = {} & \frac{\cos\left(\frac{2L\omega}{c}\right)\ \delta\left(\frac{2L+x-ct}{c}\right)\ \left(\mathbf{u}\left(\frac{x-ct}{c}\right)-1\right)}{2\omega} \\ & + \frac{\cos\left(\frac{2L\omega}{c}\right)\ \delta\left(\frac{x-ct}{c}\right)\ \left(\mathbf{u}\left(\frac{2L+x-ct}{c}\right)-1\right)}{2\omega} \end{aligned} \tag{A.35}$$

Looking at the arguments of the second term in Equation A.35, it can be shown using similiar analysis that was performed for the case where n = 1, that the dirac and heaviside functions cannot exist within the limits of interest. Therefore, this contribution will not be observed. The a term can therefore be simplifed to the following:

$$a_1 = -\frac{\omega}{2c^2} \cdot cos\left(\frac{2L\omega}{c}\right) \cdot \delta\left(t - \frac{x}{c} - \frac{2L}{c}\right) \tag{A.36}$$

The next contribution is the following :

$$\begin{aligned} a_2 = {} & \mathbf{u}\left(\frac{x-2L+ct}{c}\right)\ \sin\left(\frac{2\omega x}{c}\right)\ \left(\mathbf{u}\left(\frac{2L+x-ct}{c}\right)-1\right) \\ & - \mathbf{u}\left(\frac{x-4L+ct}{c}\right)\ \sin\left(\frac{2\omega(2L-x)}{c}\right)\ \left(\mathbf{u}\left(\frac{x-ct}{c}\right)-1\right) \\ & - \frac{0.5000\,\delta\left(\frac{2L+x-ct}{c}\right)\ \mathbf{u}\left(\frac{x-2L+ct}{c}\right)\ \cos\left(\frac{2\omega x}{c}\right)}{\omega} \\ & - \frac{0.5000\,\delta\left(\frac{x-4L+ct}{c}\right)\ \cos\left(\frac{2\omega(2L-x)}{c}\right)\ \left(\mathbf{u}\left(\frac{x-ct}{c}\right)-1\right)}{\omega} \\ & - \frac{0.5000\,\delta\left(\frac{x-2L+ct}{c}\right)\ \cos\left(\frac{2\omega x}{c}\right)\ \left(\mathbf{u}\left(\frac{2L+x-ct}{c}\right)-1\right)}{\omega} \\ & - \frac{0.5000\,\mathbf{u}\left(\frac{x-4L+ct}{c}\right)\ \delta\left(\frac{x-ct}{c}\right)\ \cos\left(\frac{2\omega(2L-x)}{c}\right)}{\omega} \end{aligned} \tag{A.37}$$

The step function in the first term of Equation A.37 is adequetely simplified. For the second term, the following relation must hold:

$$0 \leq \left(t + \frac{x}{c} - \frac{4L}{c}\right) \wedge \left(t - \frac{x}{c}\right) \tag{A.38}$$

This first occurs when the first step function is active. The second step function can therefore be neglected. The fifth and sixth terms can be shown to not exist in the limits where t>0 and L>=x >= 0. For the fourth and fifth term, it can be shown that the arguments for the heaviside functions are positive when the delta function equals zero. For this reason, the heaviside function does not need to be written. a_2 can therefore be rewritten to the following:

$$\begin{aligned} a_2 = {} & \mathbf{u}\left(t + \frac{x - 2\,L}{c}\right) \sin\left(\frac{2\omega}{c} \cdot (-x)\right) \\ & + \mathbf{u}\left(t + \frac{x - 4\,L}{c}\right) \sin\left(\frac{2\,\omega\,(2\,L - x)}{c}\right) \\ & - \frac{1}{2\omega} \cdot cos\left(\frac{2\omega}{c} \cdot (-x)\right) \cdot \delta\left(\frac{2 \cdot L + x}{c} - t\right) \\ & + \frac{1}{2\omega} \cdot cos\left(\frac{2\omega}{c} \cdot (2L - x)\right) \cdot \delta\left(t + \frac{x - 4L}{c}\right) \end{aligned} \tag{A.39}$$

The next contribution is given as the following:

$$\begin{aligned} a_3 = {} & -\frac{0.5000\,\delta\left(\frac{2\,L+z-c\,t}{c}\right)\ \text{heaviside}\left(-\frac{2\,L+z-c\,t}{c}\right)}{\omega} \\ & + \frac{0.5000\ \cos\left(\frac{2\,\omega}{c} \cdot (L)\right)\ \delta\left(\frac{z-2\,L+c\,t}{c}\right)\ \text{heaviside}\left(\frac{z-4\,L+c\,t}{c}\right)}{\omega} \\ & + \frac{0.5000\ \cos\left(\frac{2\,\omega}{c} \cdot (L)\right)\ \delta\left(\frac{z-4\,L+c\,t}{c}\right)\ \text{heaviside}\left(\frac{z-2\,L+c\,t}{c}\right)}{\omega} \end{aligned} \tag{A.40}$$

It can be shown that the heaviside and dirac functions do not exist within the limits of the system for the second term, reducing a_3 to the following:

$$a_3 = \frac{1}{2\omega}\left(-\delta\left(t - \frac{x}{c} - \frac{2L}{c}\right) + \cos\left(\frac{2\,\omega}{c} \cdot (L)\right) \cdot \delta\left(t + \frac{x}{c} - \frac{4L}{c}\right)\right) \tag{A.41}$$

The next contribution is given :

$$\begin{aligned} a_4 = {} & -\mathbf{u}\left(\frac{z - 4\,L + c\,t}{c}\right) \sin\left(\frac{2\,\omega\,(L - z)}{c}\right) \left(\mathbf{u}\left(\frac{2\,L + z - c\,t}{c}\right) - 1\right) \\ & - \frac{\delta\left(\frac{2\,L+z-c\,t}{c}\right)\ \mathbf{u}\left(\frac{z-4\,L+c\,t}{c}\right)\ \cos\left(\frac{2\,\omega\,(L-z)}{c}\right)}{2\omega} \\ & - \frac{\delta\left(\frac{z-4\,L+c\,t}{c}\right)\ \cos\left(\frac{2\,\omega\,(L-z)}{c}\right)\ \left(\mathbf{u}\left(\frac{2\,L+z-c\,t}{c}\right) - 1\right)}{2\omega} \end{aligned} \tag{A.42}$$

This simplifies to the following :

$$\begin{aligned} a_4 = {} & \mathbf{u}\left(t + \frac{x - 4L}{c}\right) \sin\left(\frac{2\,\omega\,(L - z)}{c}\right) \\ & + \frac{1}{2 \cdot \omega} \cdot \cos\left(\frac{2\,\omega\,(L - z)}{c}\right) \delta\left(\frac{x - 4L + ct}{c}\right) \end{aligned} \tag{A.43}$$

The final term is the a_5 term which is the following :

$$a_5 = \frac{1}{2\omega}\delta\left(\frac{x-4\,L+c\,t}{c}\right)\,\mathbf{u}\left(\frac{x-4\,L+c\,t}{c}\right) \tag{A.44}$$

Which can be rewritten as the following:

$$a_5 = \frac{1}{2\omega}\cdot\delta\left(t+\frac{x-4\,L}{c}\right) \tag{A.45}$$

The full simplified expression for the case with 2 sets of reflections can thus be given

$$F_{tr,M2} = F_{tr,M1} + \sigma_1\begin{bmatrix}\beta^3\\ \beta^5\end{bmatrix}\cdot\mathbf{F}_{tr,M2} + \sigma_5\begin{bmatrix}\beta^2\\ \beta^3\end{bmatrix}\delta_{\,t-\frac{x}{c}-2T_d} + \sigma_5\begin{bmatrix}\beta^3\\ \beta^4\\ \beta^5\\ \beta^6\end{bmatrix}\delta_{\,t+\frac{x}{c}-4T_d} \tag{A.46}$$

$$\mathbf{F}_{tr,M2} = \begin{bmatrix}\mathbf{u}\left(t-\frac{x}{c}-2T_d\right)\,\sin\left(\frac{2\,\omega\,(-x)}{c}\right)+\mathbf{u}\left(t+\frac{x}{c}-4T_d\right)\,\sin\left(\frac{2\,\omega\,(2\,L-x)}{c}\right)\\ \mathbf{u}\left(t+\frac{x}{c}-4T_d\right)\sin\left(\frac{2\,\omega\,(L-z)}{c}\right)\end{bmatrix} \tag{A.47}$$

$$\delta_{\,t-\frac{x}{c}-2T_d} = \delta(t-\frac{x}{c}-2T_d)\begin{bmatrix}-cos\left(\frac{2\omega}{c}\cdot(-x)\right)\\ -1\end{bmatrix} \tag{A.48}$$

$$\delta_{\,t+\frac{x}{c}-4T_d} = \delta(t+\frac{x}{c}-4T_d)\begin{bmatrix}cos\left(\frac{2\,\omega\,(2\,L-x)}{c}\right)\\ \cos\left(\frac{2\omega}{c}\cdot(L)\right)\\ \cos\left(\frac{2\omega}{c}\cdot(\,L-x)\right)\\ 1\end{bmatrix} \tag{A.49}$$

The third term can be expressed after simplification as the following :

$$F_{tr,M3} = F_{tr,M2} + \sigma_1\begin{bmatrix}\beta^5\\ \beta^7\\ \beta^9\end{bmatrix}\cdot\mathbf{F}_{tr,M2} + \sigma_5\begin{bmatrix}\beta^4\\ \beta^5\\ \beta^6\\ \beta^7\\ \beta^8\end{bmatrix}\delta_{\,t-\frac{x}{c}-4T_d} + \sigma_5\begin{bmatrix}\beta^5\\ \beta^6\\ \beta^7\\ \beta^8\\ \beta^9\\ \beta^{10}\end{bmatrix}\delta_{\,t+\frac{x}{c}-6T_d} \tag{A.50}$$

$$\mathbf{F}_{p,tr,n=3,M} = \begin{bmatrix}\mathbf{u}\left(t-\frac{x}{c}-4T_d\right)sin(\sigma_2\cdot(3\cdot L-x))+\mathbf{u}\left(t+\frac{x}{c}-6T_d\right)\cdot sin(\sigma_2\cdot(L-x)-4\sigma_3)\\ \mathbf{u}\left(t-\frac{x}{c}-4T_d\right)\cdot sin(\sigma_2(3L-x)-2\sigma_3)+\mathbf{u}\left(t+\frac{x}{c}-6T_d\right)\cdot sin(\sigma_2(2L-x)-4\sigma_3)\\ \mathbf{u}\left(t+\frac{x}{c}-6T_d\right)\cdot sin(\sigma_2\cdot(3\cdot L-x)-4\cdot\sigma_3)\end{bmatrix} \tag{A.51}$$

$$\delta_{\,t-\frac{x}{c}-4T_d} = \delta(t-\frac{x}{c}-4T_d)\begin{bmatrix}-cos\left(\frac{4\omega L}{c}\right)\\ -\cos\left(\frac{2\omega}{c}\cdot(L+x)\right)\\ -\cos\left(\frac{2\,L\,\omega}{c}\right)\\ -\cos\left(\frac{2\omega}{c}\cdot(x)\right)\\ -1\end{bmatrix} \tag{A.52}$$

$$\delta_{t+\frac{x}{c}-6T_d} = \delta(t+\frac{x}{c}-6T_d)\begin{bmatrix} cos\left(\frac{2\,\omega\,(3\,L-x)}{c}\right) \\ \cos\left(\frac{4\omega}{c}\cdot(L)\right) \\ cos\left(\frac{2\,\omega\,(2\,L-x)}{c}\right) \\ \cos\left(\frac{2\omega}{c}\cdot(L)\right) \\ cos\left(\frac{2\,\omega\,(\,L-x)}{c}\right) \\ 1 \end{bmatrix} \tag{A.53}$$

A number of patterns can be recognized to create a general expression for the generated force as a function of number of reflections. It can be seen that the persistant sinusoidal term is, as expected, the same expression that was found for the steady state analysis of the force equation multiplied by a step function corresponding to the number of reflections at a given time. The impulse component occours due to the gradient between the wave that already exists and the propogation of the new wave. A general expression of the generated force as a function of sets of reflections can be expressed as the following:

$$\begin{aligned} F_{tr} = \sigma_1 \cdot \sum_{q=1}^{\infty} \mathbf{u}\left(t-\frac{x}{c}-2\cdot q\cdot T_d\right)\cdot\sum_{i=1}^{q-1}\beta^{2q-1+2\cdot(i-1)}\cdot(sin(\frac{2L\omega}{c}(n-i-1)\cdot L-x)) \\ +\sum_{q=1}^{\infty}\mathbf{u}\left(t+\frac{x}{c}-2\cdot(q)T_d\right)\left[\sum_{i}^{q-1}\beta^{2q-1+2\cdot(i-1)}\left(sin(\frac{2L\omega}{c}\cdot((n-i+1)\cdot L-z))\right)\right. \\ \left.+F_{p,last}(q)\right]+\delta_R+\delta_L \end{aligned} \tag{A.54}$$

Delta terms are the following

$$\begin{aligned} \delta_L = -\frac{pAmp^2}{c}\cdot\sum_{q=1}^{\infty}\delta(t-\frac{x}{c}-(q-1)\cdot T_d)\cdot(\sum_{m=1}^{q}\beta^{2(q+m-2)}cos\left(\frac{2\omega L}{c}\cdot(q-m)\right) \\ +\sum_{p=1}^{q-1}\beta^{2\cdot(q+p)-3}cos\left(\frac{2\omega}{c}\cdot\left((q-p-1)\cdot L+z\right)\right) \end{aligned} \tag{A.55}$$

$$\begin{aligned} \delta_R = \frac{pAmp^2}{c}\cdot\sum_{q=1}^{\infty}\delta(t+\frac{x}{c}-2\cdot(q-1)\cdot T_d)(\sum_{m=1}^{q}\beta^{2(q+m-1)}cos\left(\frac{2\omega}{c}\cdot((n-j+1)\cdot L-z)\right) \\ +\sum_{p=1}^{q}\beta^{2(i+p-2)+1}cos\left(\frac{2\omega}{c}(q-p)\cdot L\right) \end{aligned} \tag{A.56}$$

$$F_{p,last}(n) = \beta^{1+(n-1)\cdot 4}\cdot sin\left(\frac{2\omega}{c}(L-x)\right) \tag{A.57}$$

This expression has been implemented in MatLAB and has been shown to produce all of the terms within the limits of the system as the number of reflections increases.

Appendix B

Linear Kalman Filter

This appendix shows the derivation and results of designing a Linear Kalman Filter for an air bubble experiencing an acoustophoretic force

B.1 Linear Kalman Filter

The Linear Kalman Filter (LKF) is a linear system observer that can optimally observe the states of a system disturbed by a process noise and with measurement noise on the outputs, assuming that the distribution of the process and system noise are gaussian. Kalman Filters are designed using a state space formulation of the system process whereby the process and measurement noise covarriances have been estimated. In this manner, the filter is able to balance both the "estimated" states of the system by using the state space model and the experimental measured data points to give a processed filtered state estimation.

The fact the designer of a Kalman Filter can choose the structure that the filter attempts to observe is taken advantage of in this thesis by introducing acoustic streaming force as a state in the state space formulation. This state cannot be directly measured and will therefore be observed by the filter. The state is also assumed not to change due to the other states and will therefore change due to its own state autocorrelation.

This section contains of the following subsections:

- Section B.2 : Linear Kalman Filter Bounding Equations
- Section 8.3 : Linear Air Bubble Model Structure
- Esimating Process and Measuremnet Noise
- Testing and Validating LKF on experimental data

B.2 Linear Kalman Filter Bounding Equations

The linear Kalman Filter can be used to estimate system state values given a discrete system in the form :

$$x(k+1) = \mathbf{A} \cdot x(k) + \mathbf{B} \cdot u(k) + \mathbf{V} \cdot v(k) \tag{B.1}$$

$$y(k) = \mathbf{C} \cdot x(k) + n(k) \tag{B.2}$$

Where $n(k)$ refers to a zero mean gaussian noise with covariance, N and $v(k)$ refers to the process noise of covariance M. The covariances are defined as the following, where $E\{x\}$ refers to the expected value of x:

$$E\{v(k) \cdot v^t(k)\} = ME\{n(k) \cdot n^t(k)\} = M \tag{B.3}$$

The LKF will generate an estimate for x, denoted $\hat{x}$, which minimizes the square error of x, where k is a given time step and j are the previous data values.:

$$\tilde{x}(k|j) = x(k) - \hat{x}(k|j), \quad min||\tilde{x}(k|j)||^2 \tag{B.4}$$

The optimal state esimate is given by the following expression:

$$\hat{x}(k+1|k+1) = \hat{x}(k+1|k) + \mathbf{K}(k+1) \cdot y(k+1) - \mathbf{C} \cdot \hat{x}(k+1|k) \tag{B.5}$$

Here, **K** refers to the Kalman gain which is updated depending on the state of the Kalman Filter. The physical intuition behind this matrix is that a high relative gain value indicates more faith in the system model and a lower relative gain value indicates more faith in the measurements. The Kalman Filter estimation algorithm consists of the prediction step and the update step. The prediction step is given as the following two equations:

$$\hat{x}(k+1|k) = \mathbf{A} \cdot \hat{x}(k|k) + \mathbf{B} \cdot u(k) \tag{B.6}$$

$$P^{-1}(k+1) = \mathbf{A} \cdot P(k) \cdot \mathbf{A}^T + V \cdot \mathbf{M} \cdot V^T \tag{B.7}$$

Equation B.6 simply generates an estimate for the value of the x state based on the system model for the given timestep. Equation B.7 is used to calculate an estimate state error covariance, $\mathbf{P}^-$, using the the previous timestep's predicted state error. This covariance matrix is calculated using the system matrix and measurement covariances.

The update consists of three steps : updating the Kalman Gain in the form of Equation B.8, updating the state estimate using Equation B.9 , and updating the error state covariance using Equation B.10.

$$\mathbf{K}(k+1) = P^-(k+1) \cdot \mathbf{C}^T[\mathbf{C} \cdot P^-(k+1) \cdot \mathbf{C}^T + N]^{-1} \tag{B.8}$$

$$\hat{x}(k+1k+1) = \hat{x}(k+1) + \mathbf{K}(k+1) \cdot [y(k+1) - \mathbf{C} \cdot \hat{x}(k+1|k)] \tag{B.9}$$

$$P(k+1) = [I - \mathbf{K}(k+1) \cdot C \ \cdot P^-(k+1) \tag{B.10}$$

In Equation B.10, **I** refers to an identity matrix with dimensions equal to the number of states in x.

B.3 Selection of Covariance Parameters

One of the difficulties in designing trustworthy Kalman Filters as disturbance observers is the selection of appropriate covariance values. This is because, if the values are selected incorrectly, the output of the LKF will not produce a good representation of the forces present in the system.

The initial state covariance, P^- is selected to be zero. The measurement noise matrix, **N**, state process noise matrix, **M**, and P^- matrix are now selected to be the following:

$$\mathbf{N} = \begin{bmatrix} \sigma_x & 0 \\ 0 & \sigma_v \end{bmatrix}, \qquad \mathbf{P}^- = \begin{bmatrix} 0 & 0 \\ 0 & 0 \end{bmatrix} \qquad \mathbf{M} = \begin{bmatrix} m_x & 0 & 0 \\ 0 & m_v & 0 \\ 0 & 0 & m_d \end{bmatrix} \tag{B.11}$$

Measurement Noise Estimation

It can be noted that no cross state noise and process covariances are assumed. This is because the position and velocity are both physically independent states.

The noise covariance function can, fortunately, be estimated directly from the variance of measured position values when the input to the system is at rest. This can be approximated using the sample covariance as given by the following equation:

$$cov(A, B) = \frac{1}{N-1} \sum_{i=1}^{N} (A_i - \mu_A) \cdot (B_i - \mu_B) \tag{B.12}$$

Where μ refers to the sample means of dataset A and B. Due to the variance of the measured states being the covariance of the measured states themselves, the equation for the sample variance can be used instead:

$$\hat{\sigma}_A = \frac{1}{N-1} \sum_{i=1}^{N} (A_i - \mu_A)^2 \tag{B.13}$$

A section of the identification data has been selected that has been detrended and the sample covariances of the position, σ_{xp} and velocities, σ_v are 1.5e-11 and 1.15e-6 respectively.

To get a baseline of how the Kalman Filter performs, it has initially been implemented in the nonlinear model. In this model, the only disturbances present are in the form of the differences between the linearized and nonlinear model. A simulated white noise is also added to the signals read by the LKF. This simulated noise is set to have the same variance as the experimentally found values. There is no disturbing acoustic streaming force present in the model. The LKF has been implemented using measurement data input and can be seen plotted with different measurement covariance values in Figure B.1. This Figure shows the response at times where the linear model underestimates the acoustphoretic (left) force and is much more similar to the linearization point (right).

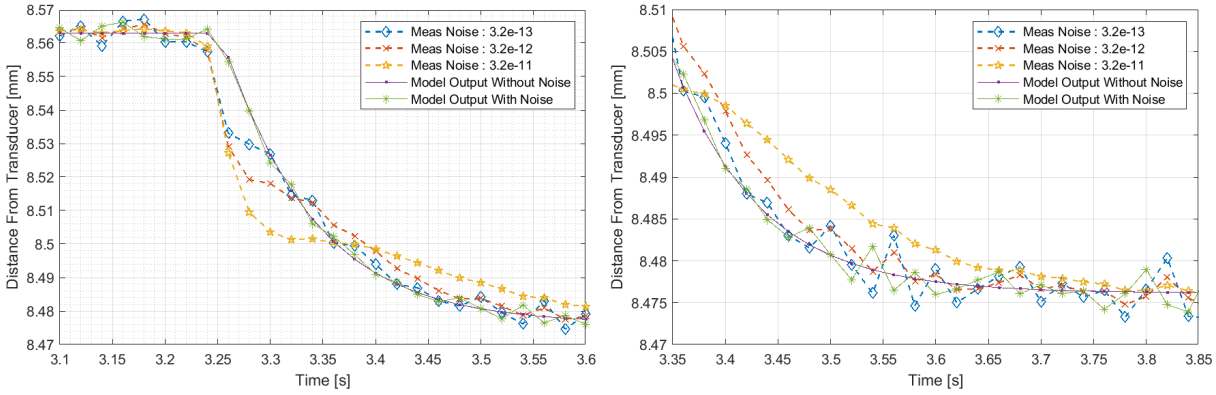

Figure B.1: This figure shows the air bubble position output of the LKF with different values for the system noise covariance matrix, **N**. The modelled noise has a value of 3.2e-12 and the process noise value for the disturbance state, m_d is 2e-17.

From the plot to the right in Figure B.1, it can be seen that underestimating the noise covariance, by comparing the blue, purple,and green lines, causes the LKF position state to be overly reactive to measurement noise. When looking at these lines in the plot to the left, the lower covariance value causes the LKF to respond more quickly to the uncertainty between the system model and the true process. The attribution of noise to the system dynamics is undesireable and choosing covariance values too low can be understood to provide a poor LKF state estimate.

It can be seen that overestimating the noise, as can be seen when comparing the the yellow lines to the purple and green lines, in both the left and right plot, causes the LKF to output an incorrect position state estimate. Here, the dynamics of the measured data is not fully captured as the measurments are interpretted as being mostly noise and the underlying dynamics are perscribe mostly by the system model.

Overall, the system response when the noise in the system is the same as that which is simulated, as seen as the red line in Figure B.1, as expected, has the best trade off between reaction to modelling noise and response to the system dynamics. These values are thefore accepted as the covariance values for the measurment noise matrix.

Process Noise Estimation

The purpose of the system identification methods used in this chapter are to determine the forces present in the system. Therefore, the selection of the process noise plays a key role in the results of this aim. The advantage of using a nonlinear model of the system when designing the LKF is that the "true" particle position and forces are available for measurement. The error between the output of the LKF and the simulated positions can be found without noise, reducing a dimension of complexity when interpreting the output of the LKF.

In order to find an appropriate disturbance state variance, the nonlinear model with the LKF has been run with different disturbance state covariances. The RMS of the position error has been used as a metric for the LKF performance. The model has been run with and without noise on the position and velocity signals read by the LKF. The results of this can be seen in Figure B.2 .

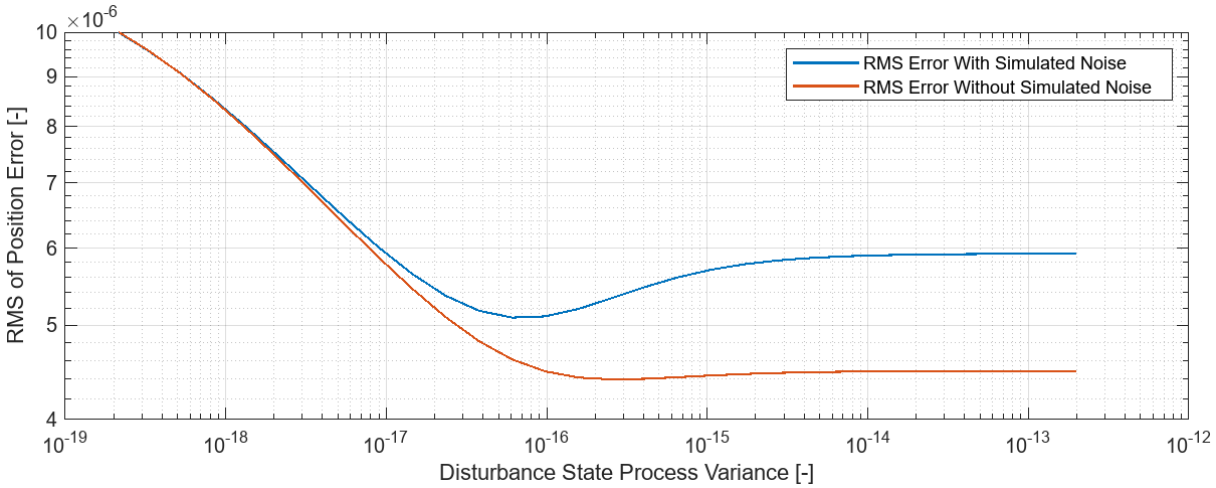

Figure B.2: This figure shows the RMS of the positions error when there is and is not noise on the position values as a function of the LKF disturbance state process noise.

It can be seen from the orange line in Figure B.2 that, if no noise is present, there appears to be a minmum of position state error with a minimum disturbance covariance value at approximately 2e-16. This error value at this minimum appears to be very similiar to the RMS that ocurs when the covariance is increased above this value. This would suggest that any disturbance variance value higher than than 2e-16 would be an acceptable value. This is however, not the case when noise is present on the signal as can be seen from the blue line in Figure B.2. When noise is present on the state measurments, there is, instead, a local minimum of position error with deteriorating estimation perforrmance above this value. This is because if the process noise variance is too high, the disturbance state will begin to interpret

the noise in the system as a part of the system dynamics. If it is too low, the LKF will not react to the measured dynamics of the particle and there will be high position error RMS as can be seen as the variance trends below 10^{-17}. A disturbance state variance value of 6e-17 has been selected as this lies at the minimum and should therefore provide the best state estimation.

The measurement noise and process noise matrices that have been selected have the following values:

$$\mathbf{N} = \begin{bmatrix} 4.2e-12 & 0 \\ 0 & 3.2e-9 \end{bmatrix}, \qquad \mathbf{M} = \begin{bmatrix} 0 & 0 & 0 \\ 0 & 0 & 0 \\ 0 & 0 & 6e-17 \end{bmatrix} \tag{B.14}$$

B.4 Implementation of the LKF

In this section, the LKF is shown to be applied to the nonlinear model and on experimental data. The results are shown and discussed.

LKF Observing the Nonlinear Model

The response of the tuned LKF on the nonlinear model can be seen shown in B.3. Noise was added to the measured signals to simulate measured data. Position, velocity, and the disturbance state values can be seen plotted alongside the test data in Figure B.3.

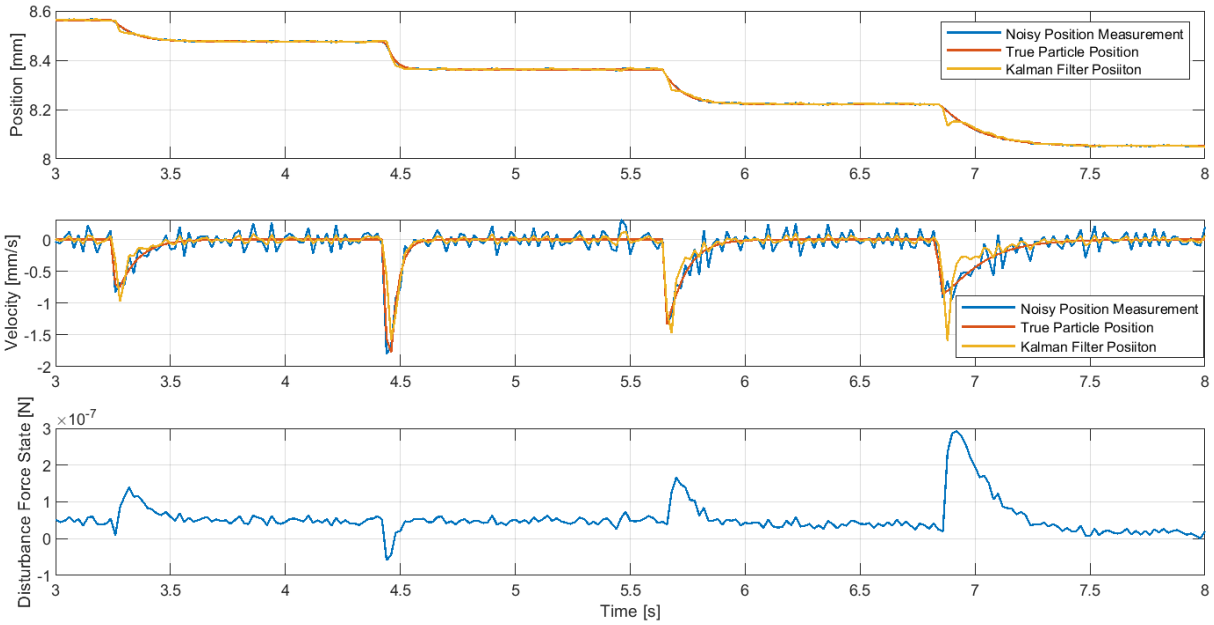

Figure B.3: Kalman Filter state output data compared with the nonlinear model.

On first inspection of Figure B.3, when comparing the yellow and red lines in the top two plots, the LKF is appears to be good at filtering both the position and velocity states. However, when comparing the yellow and red lines in the top plot, at certain times, such as 6.8 and 5.7 seconds, it appears to be the case that the LKF overestimates the change in velocity and position before realigning with the data. This is likely due to the incorrect estimation of the amplitude of the attractive domain force causing the linearization the LKF is based off to diverge from the nonlinear model. The LKF is, however good at realigning to the measured data and rejecting the noise in the system.

It can be seen in the bottom plot of Figure B.3 in the disturbance state that there appears to be a force offset. This offset occurs during the initialization of the LKF and is due to the fact that the system was not completely settled at a node when the filter was initialized. This corresponds to the prestressing of the spring-like acoustophoretic force being at a different position. It can be seen that, because the air bubble has a relatively low movement range, that this force level appears fairly constant in the data set.

The effect of the linearization of the amplitude of the acoustophoretic force can be seen in the bottom plot of Figure B.3 by the "peaky" nature of the disturbance force. These peaks occur when the pressure wave frequency is changed and occur because the amplitude of the node attractive domain forces are under or over estimated. This can be seen in the force at approximately 3.2 and 4.4 seconds where the force is first over estimated and the underestimated. For this reason, the disturbance force is adapted to be higher and lower than its steady state value at these points to compensate for this. This is especially noticeable at 6.7 seconds where the linearized model greatly understimates the attractive force. This is likely because the input frequency corresponds with the acoustic field being nearly as far from resonance as possible with the force being in the minimum in Figure 8.3 on page 69. This incorrect estimation of the acoustophoretic force amplitude is an inherit characteristic of the LKF being applied to the system at hand.

LKF Force Estimation

The trustworthiness of the LKF state outputs is determined by its ability to accurately characterise the dynamics of the process it is observing. This is analyzed by considering the force balance in the system process as simulated by the nonlinear model and comparing it to the force estimates in the LKF.

Every time a measurement is read by the the LKF, the system model in the LKF implicitly estimates the forces that affect the air bubble that cause the change of the air bubble states. To show this, the linearized system equation for the change of the second state have been written out in Equation B.15.

$$\dot{x}_2 = \frac{1}{m} \cdot \left(-B \cdot x_2 + [k_{xp} \cdot k_f \cdot \Delta f - k_{xp} \cdot x_1 + x_3] \right) \tag{B.15}$$

The square brackets in Equation B.15 refers to the expressions that represents the acoustophoretic force. This can be compared to the actual implemented nonlinear system model using the same state notation:

$$\dot{x}_2 = \frac{1}{m} \cdot \left(-B \cdot x_2 + F_{ap} \right) \tag{B.16}$$

If the LKF force balance can be shown to be able to replicate the total forces in the nonlinear model, it can be considered to be able to accurately characterize the system dynamics. In order to demonstrate the LKF's capability of doing this, the acoustophoretic force, as simulated in the nonlinear model, is measured. The x_1, and frequency dependent terms in Equation B.15 are added to each other and shown plotted alongside the simulated nonlinear acoustophoretic force and the disturbance force term, x_3, in Figure B.4. It can be noted that the contributions from the damping velocity terms are not shown as the B coefficients are the same in the nonlinear model and the LKF.

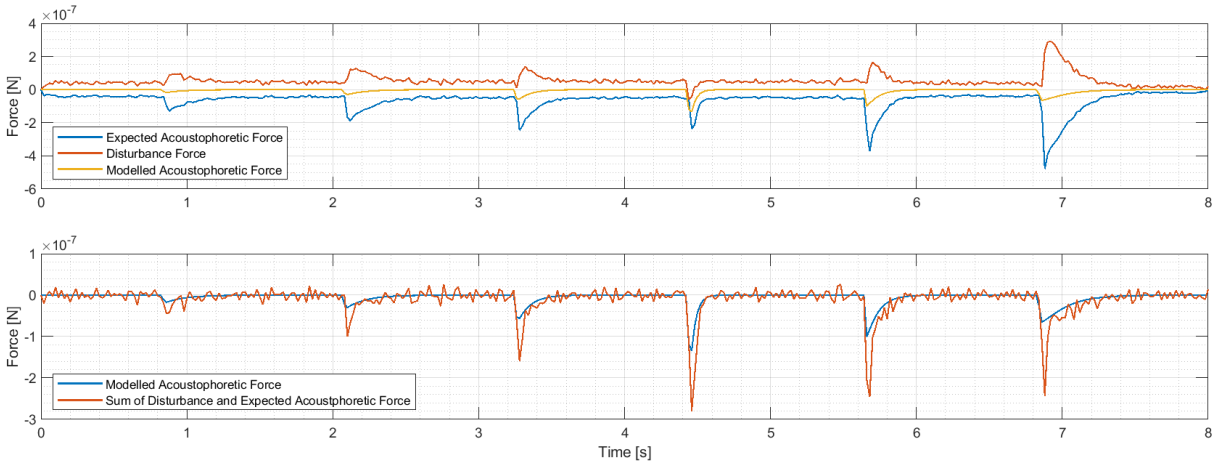

Figure B.4: This figure shows the acoustophoretic force simulated in the the nonlinear model alongside the acoustophoretic contributions as estimated by the LKF. In the top figure, the "Modelled Acoustophoretic Force" refers to the simulated acoustophoretic force affecting the air bubble in the nonlinear model. The "Expected Acoustophoretic Force" is what the estimate step of the LKF estimates the acoustophoretic force to be. The "Disturbance Force" is the amplitude of the disturbance state force, x_3 in the LKF. The bottom figure plots the summation of the "Expected Acoustophoretic Force" and the "Disturbance Force" alongside the "Modelled Acoustophoretic Force".

It can be seen from the top plot in Figure B.4 that the estimation step from the LKF does not appear to give a good estimate for the acoustophoretic force right when the input frequency is changed. However, the expected acoustophoretic force does show to settle at approximately the same time as the simulated acoustophoretic force, if not a little bit slower. This is because the disturbance state is able to to counteract the estimate of the acoustophoretic expected force in a similar time frame as it takes for the bubble to settle. The fact that the disturbance state becomes as large as it does suggests that it will be difficult to decouple the naturally occurring acoustic streaming effect from the disturbance associated with linearizing the acoustophoretic force when the input frequency is changing. However, because the disturbance state is able to settle as quickly as it does, the LKF may be able to characterize the properties of the acoustic streaming force effect when the input is held constant.

It can be noted from the bottom plot of Figure B.4 that the sum of the disturbance and expected acoustophoretic force do appear to align quite well the modelled force. However there does appear to be deviance on the first couple samples after the frequency has been changed. This could be due to the acoustophoretic force amplitude coefficient being a constant and causing the LKF's state estimation to over estimate the acoustophoretic force when the frequency is changed. This means that the disturbance force has to adaptively counteract this overestimated force, therefore causing there to be force estimation error when changes occur in the inputs.

Overall, the fact that the LKF is able to recreate the acoustophoretic present from the nonlinear model shows that it is capable of characterizing the system dynamics to a sufficient degree in the nonlinear model.

B.5 LKF Observing the Experimental Data

Now that the linear Kalman Filter has shown promising results in the nonlinear model, it has been tested on the experimental dataset. The position, velocity, and disturbance states have been shown plotted in Figure B.5.

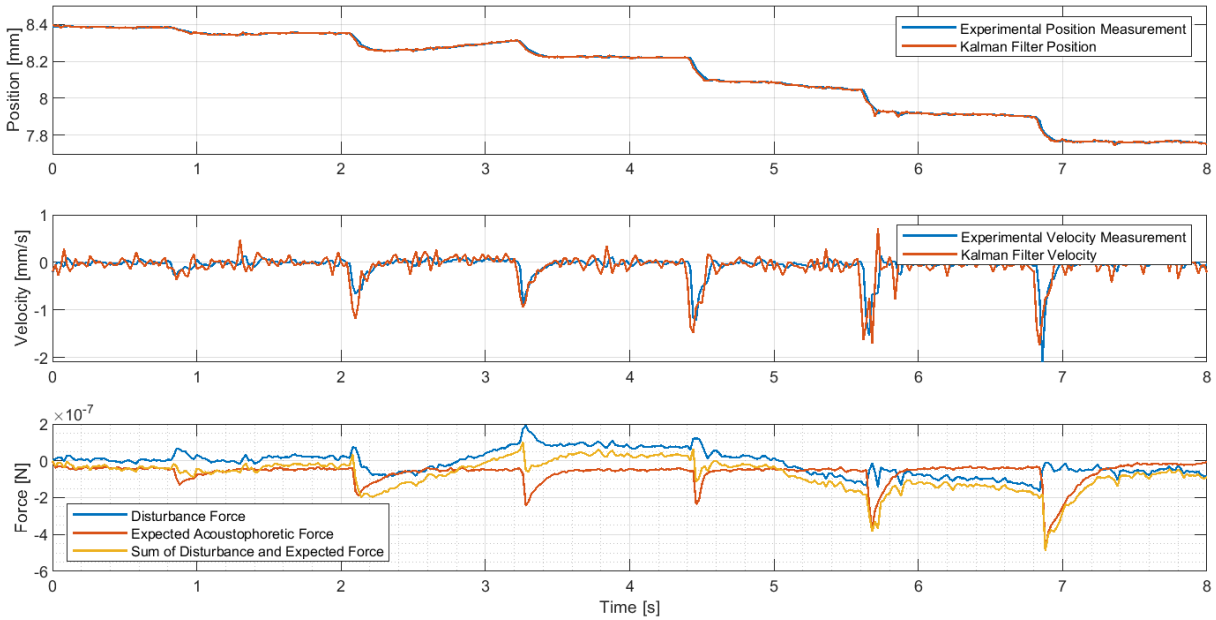

Figure B.5: This figure shows the outputs of the LKF on the system identification dataset. In the top two figures, the experimentally measured position and velocity are plotted alongside the position and velocity states of the LKF. In the bottom plot, the "Disturbance Force" is representative of the disturbance state, x_3. The "Expected Acoustophoretic Force" is the sum of the frequency and position force contributions from the estimation step of the LKF. and "Sum of Disturbance and Expected Force" is the summation of the "Disturbance Force " and the "Expected Acoustophoretic Force"

When looking at the top two plots of Figure B.5, it can be seen that the LKF appears to do a good job at filtering the position and velocity data. It can be seen that at certain times, such as 2.1 seconds and 4.5 seconds,the LKF underestimates the maximum velocity of the air bubble. Overall, the position and velocity filtering capability of the LKF appears similar to the results of implementing the LKF in the nonlinear model. It may even be argued that the LKF provides a better representation of the position data for the experimental data than the nonlinear model data as the discontinuities seen for the nonlinear model shown in Figure B.3 on page 101 when the input frequency is first changed do not appear to be present in the top plot of Figure B.5. This could suggest that the linear approximated model may be more representative of the experimental data than the nonlinear model, but this may just be due to the characteristics of the acoustic streaming force present in the specific data set.

Somewhat similar discontinuities as were seen in Figure B.3 on page 101 can, however be seen in the top plot of Figure B.5 at 5.6 seconds. However, it is likely that these are due to the visual position gathering algorithm used and not a true component of the system dynamics. This is assumed to be the case as the discontinuities quickly oscilate between positive and negative velocity values. This is reinforced by that fact that, when the velocity of the bubbles are high, the edges of the bubbles appear less clear to the video processing algorithm and this could cause this measurement "noise".

Looking at the disturbance force from the bottom plot of Figure B.5, it can be seen that there appears to be a drift in the disturbance force between 2 and 5.5 seconds that was not present in the nonlinear model. The acoustic streaming force was assumed to appear similar to a filtered gaussian noise and this would likely appear similar to the random walk-like characteristic of the shown LKF's disturbance state. However, in the bottom plot at 3.3 seconds, it can be seen that the amplitude of the disturbance is the same scale as the peak expected acoustophoretic force. This could be due to the amplitude of the disturbance varying greatly. It is not unlikely that this change of force amplitude is due to the linearization

of the acoustophoretic force amplitude and similiar to the what was shown in the nonlinear model. .

With the baseline characteristics of the disturbance force without any streaming effects present in the fluid established in the previous section, it is of interest to compare the disturbance force state from the the nonlinear model alongside the disturbance state to see what differences there may be. The two disturbance states have been plotted alongisde eachother and can be seen shown in Figure B.6.

data when the LKF is used, the nonlinear modelled force and the experimental disturbance force are plotted alongside eachother and can be seen in Figure

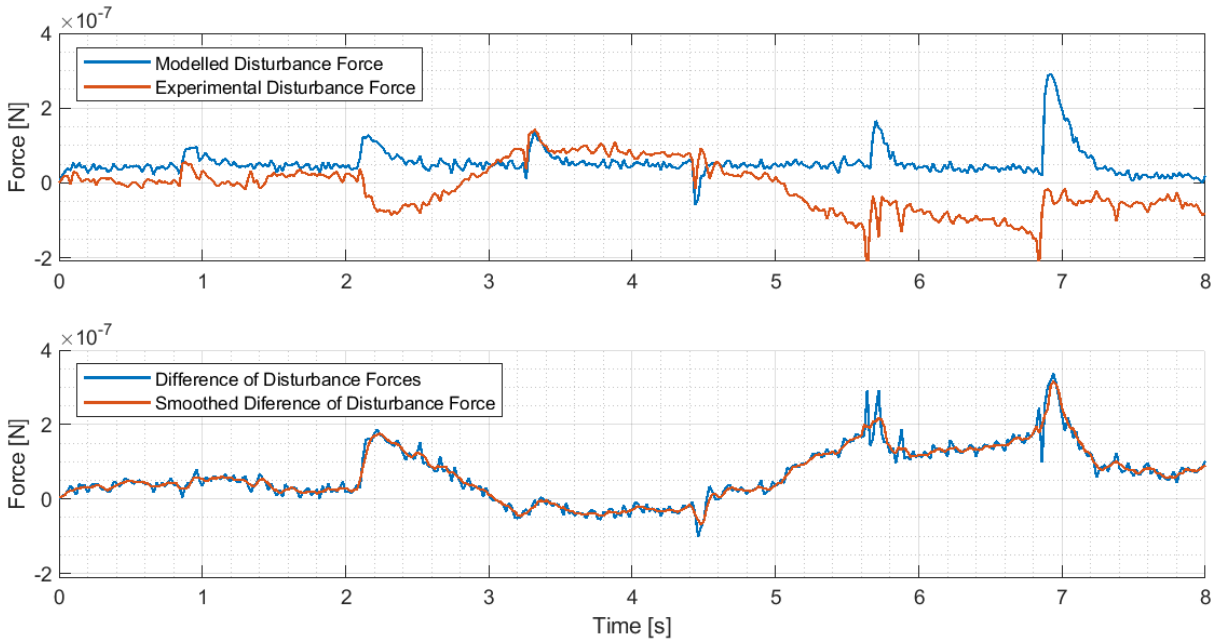

Figure B.6: This figure shows the disturbance force that the LKF generated for the nonlinear model (blue) plotted alongside the experimental data LKF output (orange).

It can be seen from the Figure B.6 that the relative change of the disturbance force in the experimental data corresponds well with the peaks from the nonlinear model. This can be observed also at times 0.9 seconds, 3.2 seconds, and 4.2 seconds. However, at times such as 2 seconds, 6.8 seconds, the results are not so promising, as the experimental data does not line particularely well up with the nonlinear data. The inconsistancy with the results of the disturbance force means that skepticism must be held when making conclusions about the force balance when using the LKF when the input is not held constant.